SIMULATION AND ANALYSIS OF UNCONVENTIONAL RESERVOIRS USING FAST MARCHING METHOD AND TRANSIENT DRAINAGE VOLUME

A Dissertation

by

CHANGDONG YANG

Submitted to the Office of Graduate and Professional Studies of
Texas A&M University
in partial fulfillment of the requirements for the degree of

DOCTOR OF PHILOSOPHY

Chair of Committee,	Akhil Datta-Gupta
Committee Members,	Michael J. King
	Eduardo Gildin
	Yalchin Efendiev
Head of Department,	A. Daniel Hill

August 2017

Major Subject: Petroleum Engineering

ABSTRACT

Unconventional tight/shale reservoirs have become an important component of the world’s energy map in the recent decade and have been attracting a lot of interests in both academia and industry. However, the industry today still faces significant challenges in understanding the fundamental mechanisms. Unconventional tight/shale reservoirs are characterized by low or ultra-low permeability, such that the transient pressure behavior might last throughout the production lifetime. Recent research has proposed a novel approach for unconventional reservoir analysis based on the high-frequency asymptotic approximation of diffusivity equation. By solving the Eikonal equation with the Fast Marching Method (FMM), one can rapidly obtain the diffusive time of flight (DToF) which depicts the pressure transient propagation process. A fast DToF-based forward simulation is further proposed to solve the fluid flow equation in a 1D equivalent coordinate system, with the DToF as the spatial coordinate.

In this study, we first adopt the DToF-based simulation as a rapid forward simulator to formulate an efficient hydraulic fracture design and optimization workflow. The DToF-based simulation can be orders of magnitude faster than the conventional finite difference/volume based simulation, and is ideal for optimization process where hundreds or thousands of simulations are necessary. Our workflow focuses on optimizing the number of hydraulic fracture stages, their spacing, and the allocation of proppant. The workflow also accounts for the geologic uncertainty, which given by different natural fracture distributions.

Next, we extend this DToF-based simulation from Cartesian and corner point grid system to unstructured grids to better characterize the complex fracture geometry induced by hydraulic fracturing job. Two different constructions of the local Eikonal equation solver, based on Fermat's principle and Eulerian discretization, are investigated and compared. Numerical examples are presented to illustrate the power and validity of this extended DToF-based simulation workflow.

Finally, we propose a model-free production data analysis method to analyze the performance of unconventional reservoirs when a full simulation model is not available. The transient drainage volume is derived directly based on bottom-hole pressure and production rate. We further define the drainage volume derivative and instantaneous recovery ratio, which can measure how effectively the hydraulic fractures have stimulated the reservoir. This technique is then applied to select candidate wells for refracturing.

DEDICATION

To my parents and wife for their endless love and support.

ACKNOWLEDGEMENTS

I would like to express my sincere gratitude to my advisor, Dr. Akhil Datta-Gupta for his academic guidance and financial support throughout my Master and Ph.D. study. His continuous encouragement helped me overcome all the difficulties and his support for industry opportunities through internship was extremely helpful for my future career. His immense knowledge, insightful view, and amiable personality are a model for me.

I would like to thank Dr. Michael J. King, the co-director of this MCERI group, for his innovative ideas and thoughtful guidance throughout my graduate school study. I would like to extend my sincere appreciation to my other committee members, Dr. Eduardo Gildin and Dr. Yalchin Efendiev for their insightful comments and suggestions that helped improve the contents of this research.

I also would like to thank Xian-Huan Wen, Paul A. Fjerstad, Han-Young Park, Jiang Xie, and Pallav Sarma for their supervision and mentorship during my summer internships with Chevron ETC.

Thanks also go to MCERI alumni and current students. I would like to appreciate the mentorship received from my seniors, the collaboration with my colleagues and the companionship of my friends in Texas A&M University.

Finally, special thanks to my parents and beloved wife, Xinyi.

CONTRIBUTORS AND FUNDING SOURCES

Contributors

This work was supervised by a dissertation committee consisting of Professor Akhil Datta-Gupta (advisor), Michael J. King, and Eduardo Gildin of the Department of Petroleum Engineering and Professor Yalchin Efendiev of the Department of Mathematics.

The hydraulic fracture design and optimization in Chapter 2 was collaborated with Aditya Vyas and was published in 2017. The student designed the optimization workflow and was the main contributor in this study. In Chapter 4, the synthetic Mangrove case was contributed by Xu Xue, the synthetic ABAQUS case was contributed by Jixiang Huang, and the field data processing was conducted in collaboration with Vishal Kumar Sharma. These work were published in 2015 and 2016.

All other work conducted for the dissertation was completed by the student independently.

Funding Sources

This work was made possible by the financial support of the member companies of the Model Calibration and Efficient Reservoir Imaging (MCERI) consortium.

TABLE OF CONTENTS

Page

LIST OF FIGURES

Page

LIST OF TABLES

CHAPTER I

INTRODUCTION

1.1 Introduction

Unconventional tight/shale reservoirs have become an important component of the world's energy map in the recent decade. The successful development of such reservoirs relies on horizontal wells completion and multistage hydraulic fracturing techniques (Holditch 2010). Even through the industry practice has become quite successful in the U.S., the engineers today still face significant challenges in understanding the fundamental mechanisms involved in the production of unconventional resources. Further research in simulation and analysis of unconventional reservoirs has been attracting a lot of interest in both academia and industry. Further technology advancement can help optimize the unconventional reservoir development by reducing costs and minimizing risks.

Currently, decline curve analysis (Fetkovich 1980; Valko and Lee 2010) and pressure/rate transient analysis (Clarkson et al. 2012; Ilk et al. 2010; Song and Ehlig-Economides 2011) are two types of widely used analytical methods for production forecast in tight/shale reservoir development. The methods in the decline curve analysis are mostly curve-fitting, used to predict production via extrapolation and obtain the estimated ultimate recovery. There is no physical model associated with the decline curve analysis and the reservoir and fracture properties are mainly ignored. In the pressure/rate transient analysis, reservoir and fracture properties are first estimated from identified flow regimes, and then well production is predicted with the estimated properties. Pressure/rate transient analysis can only incorporate simplified completion and reservoir geometry, such as a homogeneous reservoir, planner hydraulic fractures, and full completion. The predictive power of these analytical techniques highly relies on the quantity and quality of production data. The analytical models are very useful especially when only production data are available, and there is very limited subsurface information. However, they become inadequate when we have a better knowledge of the reservoir heterogeneity and complex hydraulic fracture geometry through the integration of geological, geophysical, and engineering data.

When adequate subsurface information is available, numerical simulations have also been used to perform unconventional reservoir analysis (Cipolla et al. 2010; 2012; 2011; Fan et al. 2010; Freeman et al. 2010). The advantage of numerical simulation is that it can rigorously account for reservoir heterogeneity, complex fracture geometry and complicated physical processes, such as rock compaction, gas diffusion, and adsorption. However, the biggest disadvantage of numerical simulation is that it can be very time-consuming, particularly when a high-resolution simulation model is used to accurately model complex fracture geometry and the flow in the vicinity of the hydraulic fractures. In order to obtain a reliable prediction, the parameters of numerical models usually need to be calibrated by matching available production/pressure history data. The calibration process, as well as uncertainty quantification and field development optimization, require hundreds or thousands of simulation runs and thus become extremely computational expensive for a high-resolution simulation model.

In our recent research, we have proposed a novel approach for unconventional reservoir analysis based on the diffusive time of flight (DToF) provided by the Fast

Marching Method (FMM) (Datta-Gupta et al. 2011; King et al. 2016; Xie et al. 2015a, 2015b; YangVyas et al. 2017; Zhang et al. 2016; Zhang et al. 2013). This DToF-based approach stands midway between the simplified analytical models and conventional numerical simulations. Compared with simplified analytical models, this proposed DToF-based approach can incorporate reservoir heterogeneity, complex fracture geometry, and complicated physical processes. Compared with conventional numerical simulations, it is computationally more efficient, making it ideal for uncertainty analysis, parameter calibration, model ranking/selection, and field development optimization.

Before we introduce our proposed DToF-based approach for unconventional reservoir analysis, let's first take a brief look at the Fast Marching Method.

1.2 Fast Marching Method

The Fast Marching Method is a numerical technique, first proposed by Sethian (1996) and Sethian (1999), to efficiently solve nonlinear Eikonal equations, which are typically seen in first-arrival ray tracing or wave fronts propagation. In the Eikonal equation (shown by Eq.1.1), $\alpha(\vec{x})$ and boundary condition of $\tau(\vec{x})$ are usually supplied as known input.

$$\sqrt{\alpha(\vec{x})}\left|\nabla\tau(\vec{x})\right|=1 \tag{1.1}$$

FMM is a single-pass method which utilizes the fact that the value of $\tau(\vec{x})$ for the first-order partial differential equation depends only on the value of τ along the characteristic(s) passing through the point $\vec{x}$ (Sethian 1996). Thus, the solution of τ can be constructed in an orderly one-pass fashion from smaller values of τ to larger values. This monotonic marching behavior of FMM directly considers the causality requirement, which as defined by Vidale (1988), that “the time for the part of the ray path leading to a point must be known before the time of the point can be found.” As an efficient approach to solving the nonlinear Eikonal equations, FMM has been widely applied to many disciplines, including computational geometry, medical imaging, computational fluid dynamics and seismic analysis. The basic framework of the Fast Marching Method comprises of the following steps (Sethian 1999):

(1) Label all grid nodes as *unknown*;

(2) Assign τ values (usually zero) to the nodes corresponding to the initial position of the propagating front and label them as *accepted*;

(3) For each node that is *accepted*, locate its immediate neighboring nodes that are *unknown* and label them as *considered*;

(4) For each node labeled as *considered*, update its τ value based on its accepted neighbors using the minimum local solutions;

(5) Once all nodes labeled as *considered* have been locally updated, we pick the node which has the minimum τ value among them, and label it as *accepted*;

(6) Go to step (3) until all nodes are *accepted*.

These steps can be illustrated with Dijkstra’s Algorithm in a 5-stencil Cartesian lattice grid (as depicted in Figure 1.1). We put one point as the initial position of the propagating front and label it as accepted (solid) as shown in (a). Then its immediate neighbors *A*, *B*, *C*, and *D* are marked as *considered* (circle) as shown in (b). After the τ values of *A*, *B, C* and *D* have been updated, we pick the smallest one (suppose it is *A*) and mark it as *accepted* as shown in (c). Then its neighbors *E, G*, and *F* are added into the *considered* as shown in (d). These steps will repeat for the next accepted point, suppose it is *D* as shown in (e), and then suppose it is *H* as shown (f) until all the points of the entire domain are accepted.

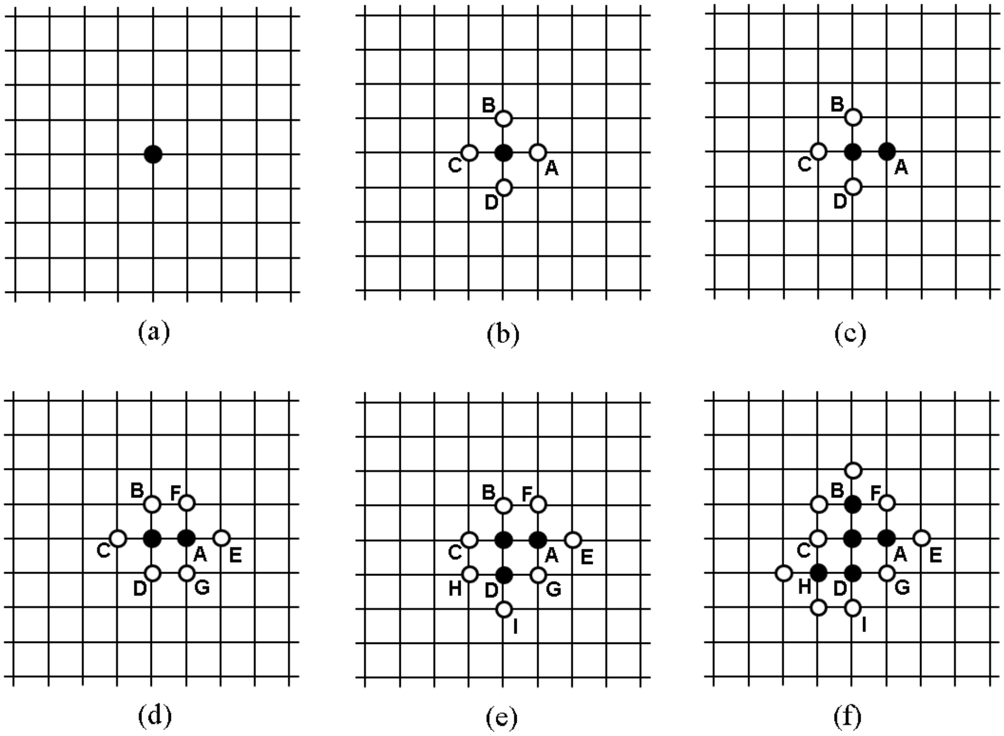
(a) (b) (c) (d) (e) (f)

Figure 1.1 Illustration of Dijkstra's Algorithm (modified from Xie et al. (2015b))

The local update of τ value for the 5-stencil Cartesian grid can be written with the standard finite difference notation as (Hassouna and Farag 2007; Sethian 1996):

$$\max\left(D_{ij}^{-x}\tau, -D_{ij}^{+x}\tau, 0\right)^2 + \max\left(D_{ij}^{-y}\tau, -D_{ij}^{+y}\tau, 0\right)^2 = \frac{1}{\alpha} \tag{1.2}$$

Here the upwind finite difference operator *D* for $\pm x$ directions can be written as $D_{ij}^{-x}\tau = (\tau_{i,j} - \tau_{i-1,j}) / \Delta x$ and $D_{ij}^{+x}\tau = (\tau_{i+1,j} - \tau_{i,j}) / \Delta x$. Similar equations hold for $\pm y$ directions. In Eq.1.2, τ values at unknown points are regarded as infinity, and the "max" function is used to guarantee the "upwind" criteria. Eq.1.2 leads to a quadratic equation, and its minimum positive root gives us the τ value at point (i, j). Alternatively, the τ values can be calculated from each of the four quadrants (bottom-left, bottom-right, top-left, and top-right) by conventional finite difference formulation and then take the minimum τ value obtained.

The computational efficiency of the FMM mainly comes from two facts, which are: 1) FMM only involves solving local quadratic equations and visiting every grid point once; 2) the implementation of the min-heap data structure to find the minimum value from the *considered* list. As a result, the FMM calculation only has a computational complexity of $O(N \log N)$, where N is the total number of computing nodes in the domain (Sethian 1999). More details of the algorithm and some extensions can be found in previous works (Fomel and Sethian 2002; Lelièvre et al. 2011; Sethian 1996; Sethian 1999; Sethian and Vladimirsky 2000).

1.3 DToF-based Fluid Flow Simulation

The depth of investigation is an important concept in the traditional pressure transient analysis to link the pressure response and reservoir properties. Lee (1982) proposed the definition to be the propagation distance of the maximum pressure draw-down for an impulse source/sink. In 2D radial flow, the depth of investigation (also known as the radius of investigation) in field units is calculated by Eq.1.3, which is originally derived from the line-source analytical pressure transient solution in homogeneous reservoirs.

$$r = \sqrt{\frac{kt}{948\phi\mu c_t}} \tag{1.3}$$

Unconventional tight/shale reservoirs are characterized by low or ultra-low permeability, which might result in a pressure transient behavior throughout the production lifetime. Therefore, the concept of depth of investigation is not limited to traditional well test analysis, and it becomes an important parameter to characterize the production of unconventional wells (Datta-Gupta et al. 2011). In the presence of reservoir heterogeneity, Vasco et al. (2000) and Kulkarni et al. (2000) derived the Eikonal equation for pressure front propagation and introduced the concept of the diffusive time of flight using the asymptotic ray theory from geometric optics and seismology. Their derivation provides the asymptotic solution of diffusivity equation (Eq.1.4) to capture the pressure front propagation, in analogy to the wave-front propagation.

$$\nabla \cdot \left(\frac{k}{\mu} \vec{\nabla} p \right) = \phi c_t \frac{\partial p}{\partial t} \tag{1.4}$$

By applying Fourier transform and asymptotic expansion of the diffusivity equation (Eq.1.4), it can be shown that in the high-frequency limit the pressure front propagation can be described by Eikonal equation (as given by Eq.1.1). In this case, the unknown τ is called diffusive time of flight (DToF), which is analogous to the radius of investigation in Eq.1.3 and is conceptually a measure of distance rather than time. The other term α is called diffusivity, defined by Eq.1.5. It is worthy to point out that all the reservoir heterogeneity information is lumped into this diffusivity term and later be embedded in variable τ after solving the Eikonal equation.

$$\alpha(\vec{x}) = \frac{k(\vec{x})}{\phi(\vec{x}) \mu c_t} \tag{1.5}$$

The derived Eikonal equation (Eq.1.1) describes the propagation of the pressure front and can be efficiently solved by the Fast Marching Method, developed by Sethian (1996) and Sethian (1999). The DToF obtained at each location characterizes the general connectivity to the sink/source point. By applying different DToF cut-offs or contours and adding up all the pore volume within the contours, the well drainage volumes can be approximated as a function of DToF. The drainage volume can provide intuitive visualization of the pressure propagation process and is obtained without solving any actual diffusivity equation. Thus, we generalize the drainage volume from pseudo-steady state flow in conventional reservoirs, where the drainage volume is usually fixed and is determined by well rates and spacing, to transient flow in unconventional reservoirs.

Our major contribution is to calculate the well performance based on the DToF and drainage volume. Xie et al. (2015b), Zhang et al. (2016) and Cui et al. (2016) have demonstrated the validity and the speed of DToF-based approach, and have shown how it can be utilized to provide the necessary understanding to describe unconventional reservoirs and optimize the development.

Xie et al. (2015a) proposed a pseudo-steady state (PSS) geometric approximation for pressure calculation under the constant flow rate boundary condition. The PSS geometric approximation assumes that the Darcy flux is negligible beyond the drainage volume and that the pressure is approximated by a pseudo-steady state solution within the drainage volume (Agarwal 2010; Nordbotten et al. 2004). For unconventional reservoir simulation, the constant wellbore pressure boundary condition is commonly implemented. The production rate under constant BHP condition is also presented by Xie et al. (2015b).

In geometric approximation, drainage pore volume as a function of time t is required. However, by solving the Eikonal equation using FMM, we obtain the drainage pore volume as a function of the DToF. In previous studies, Xie et al. (2015a) and Xie et al. (2015b) provided an approximate conversion from DToF to physical time. For homogeneous media with known flow regimes, this conversion can work accurately. Nevertheless, it brings inaccuracy for heterogeneous media because there is no global flow pattern.

Since the reservoir heterogeneity (or connectivity) information is embedded in the DToF τ, Zhang et al. (2016) derived a more direct approach to solving the fluid flow equation, using τ as a spatial variable. The details of this τ coordinate transformation can be found in the original work by Zhang et al. (2016), and it is also provided in Appendix A for completeness. By applying the DToF coordinate transformation, the diffusivity equation is then transformed into the following formula, given by Eq.1.6

$$\frac{1}{w(\tau)}\frac{\partial}{\partial \tau}\left(w(\tau)\frac{\partial p(\tau,t)}{\partial \tau} \right) = \frac{\partial p(\tau,t)}{\partial t} \tag{1.6}$$

where $w(\tau)$ is the derivative of drainage volume with respect to τ, given by Eq.1.7

$$w(\tau) = \frac{dV_p(\tau)}{d\tau} \tag{1.7}$$

Note that $w(\tau)$ is proportional to the surface area of the drainage pore volume and is directly related to the geometry of the drainage volume of the well. The heterogeneity and the physical properties appear to have “vanished” from the diffusivity equation in Eq.1.6, but actually, the heterogeneities have been lumped into the τ and $w(\tau)$ function.

The pressure which appears within the equivalent 1D diffusivity equation will then be the pressure averaged over the differential volume at the τ -contour, $p(\vec{x},t)=p(\tau(\vec{x}),t)$. This simplification in the representation of the pressure is especially useful for production analysis as it allows us to examine the relationships between pressure, rate and drainage volume without the need for high-resolution flow simulation or detailed reservoir modeling.

The direct analogy with the diffusivity equation for a single vertical well in homogeneous reservoirs is shown in Figure 1.2. For the homogeneous reservoir with a simple well geometry, the depth of investigation or pressure propagation surface of the well is circular. However, in the presence of reservoir heterogeneity or with complex fracture geometry, the shape of the pressure propagation surface becomes twisted area and is unknown before solving the pressure propagation equation on the simulation model.

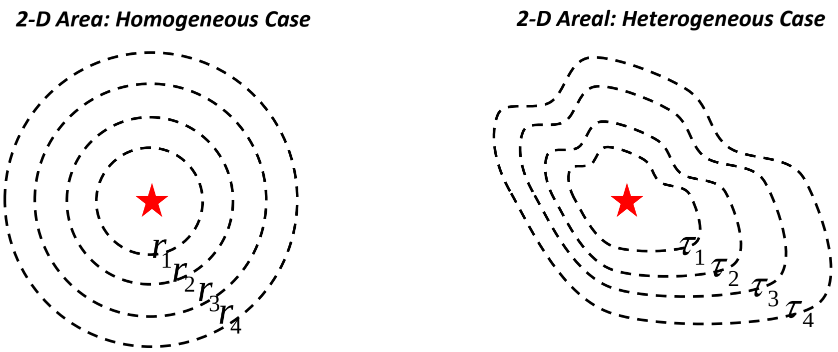

$$\frac{1}{r}\frac{\partial}{\partial r}\left(r\frac{\partial p}{\partial r}\right)=\frac{\phi\mu c_t}{k}\frac{\partial p}{\partial t}\xrightarrow{r\to\tau}\frac{1}{w(\tau)}\frac{\partial}{\partial\tau}\left(w(\tau)\frac{\partial p}{\partial\tau}\right)=\frac{\partial p}{\partial t}$$

Figure 1.2 Analogy between the $w(\tau)$ formulation in a heterogeneous reservoir and the circular drainage volume in a homogeneous reservoir

Similar to streamline simulation technique (Datta-Gupta and King 2007), the τ-coordinate transformed diffusivity equation (Eq.1.6) reduces the fluid flow from the 3D physical domain into a 1D τ-coordinate system, which can be efficiently solved with conventional numerical technique, such as finite difference method. Besides, this transformation allows more easily to incorporate complicated physical processes.

Fujita et al. (2016) extended this framework to a triple-continuum system for the modeling of shale gas reservoirs. In his approach, the DToF is calculated based on the equivalent diffusivity, and then the governing equations of different physics are transformed with the DToF coordinate. Fujita et al. (2016) comprehensively investigated the dominant physical mechanisms for shale gas reservoirs, including the Knudsen diffusion and slippage effects, gas adsorption/desorption, rock compaction, and gas diffusion from the kerogen.

King et al. (2016) also developed an analytical approach to solving the τ-coordinate transformed fluid flow equation (Eq.1.6), for the ease of use and simplicity of interpretation. They rewrote Eq.1.6 in terms of flux based on Darcy's law and solved the newly derived equation for flux by integrating its spatial gradient. They validated their analytical solution against conventional diagnostic plot for pressure draw-down and Fetkovich type curves (Fetkovich 1980), and obtained good agreement. Regarding composite reservoirs, King et al. (2016) introduced the reflection and transmission coefficients into the solution.

No matter whether being solved numerically or analytically, Eq.1.6 serves as the starting point in our DToF-based simulation for unconventional reservoirs.

1.4 Dissertation Outline

In this study, we first adopt the DToF-based simulation as a forward simulator and develop a systematic and efficient fracture design and optimization workflow. Then, we extend the DToF-based simulation to the unstructured grid system to better capture the complex fracture geometry. Finally, we propose a model-free production data analysis technique based on our cumulative understanding of the diffusive time of flight and transient drainage volume. The primary goals of the corresponding chapters are as follows:

Chapter I: General introduction and review of the DToF-based fluid flow simulation.

Chapter II: Development of a systematic and efficient fracture design and optimization workflow using the DToF-based simulation as a rapid forward simulation. The workflow also accounts for the geologic uncertainty, which is indicated by different natural fracture distributions.

Chapter III: Extension of the DToF-based simulation from Cartesian and corner point grid system to unstructured grids to better characterize the complex fracture geometry. The local Eikonal equation solvers based on Fermat's principle and Eulerian discretization for unstructured grids are investigated and compared.

Chapter IV: Development of a model-free production data analysis method to analyze the performance of unconventional reservoirs. This technique is then applied to select the candidate wells for refracturing.

Chapter V: Conclusion of this study and future work recommendations.

CHAPTER II

MULTISTAGE HYDRAULIC FRACTURE DESIGN AND OPTIMIZATION USING FAST MARCHING METHOD[*]

2.1 Introduction

This chapter extends the DToF-based simulation to dual porosity system and then it is used as the rapid forward simulator for the multistage hydraulic fracture design and optimization. We will present the Oda's method for calculating the permeability for fracture system from discrete fracture network, the proppant and fluid calculation with assumed hydraulic fracture geometry, and the derivative-free genetic algorithm based optimization workflow. The proposed multistage hydraulic fracture design and optimization workflow is demonstrated through a synthetic shale reservoir model. The optimization results are presented and discussed, especially the influence of reservoir heterogeneity induced by the distribution of nature fractures and the geologic uncertainty.

2.2 Background

Horizontal well completion and multistage hydraulic fracturing allow the wells in unconventional reservoirs to contact as much rock as possible by generating fracture networks with enough conductivity (Fisher et al. 2005; Maxwell et al. 2002). The resulting fracture networks could be quite complex due to the existence of natural fractures. Savitski

---

[*] Part of data reported in this Chapter is reprinted with permission from "Rapid Multistage Hydraulic Fracture Design and Optimization in Unconventional Reservoirs Using a Novel Fast Marching Method" by Yang, C., Vyas, A., Datta-Gupta, A., Ley, S. & Biswas, P. (2017), paper published in *Journal of Petroleum Science and Engineering* **156**: 91-101. Copyright [2017] Elsevier.

et al. (2013) showed that during hydraulic fracturing, the total area of pressurized discrete fracture networks (DFN) could be very significant. Riahi and Damjanac (2013) reported that natural fractures reopen when fracturing fluids are injected through numerical study. The reopening of pre-existing natural fractures and the induced fractures by hydraulic fracturing bring more challenges to better characterize the geological model and optimize hydraulic fracturing design. Saldungaray et al. (2013) summarized four broad categories of optimization parameters: a) wellbore placement and lateral length; b) completion hardware and isolation techniques; c) fracture spacing or the number of fractures; d) fracture geometry and conductivity.

Several researchers previously carried out the study on multistage fracture optimization. Sierra et al. (2013) investigated the correlations between various fracturing parameters, such as permeability, viscosity, and drawdown pressure, and the optimum fracture spacing through numerical simulation. Sehbi et al. (2011) presented an approach to optimize well completion design, and they found that an optimum number of hydraulic fracture stages exist for a given reservoir. Ma et al. (2013) applied a couple of stochastic optimization algorithms to address the hydraulic fracturing placement problem. They assigned uniform properties to the hydraulic fractures but didn’t account for geological heterogeneity of the model, which may lead to suboptimal hydraulic fracturing design.

2.3 Methodology

This subsection describes all the techniques used for the hydraulic fracture design and optimization, which includes Oda’s permeability upscaling, fracturing proppant and fluid calculation, DToF-based dual porosity model simulation, and genetic algorithm.

2.3.1 Oda's Permeability Upscaling

Approaches to calculating grid effective directional permeability include Oda's tensor approach (Oda 1984) and flow based permeability upscaling. Oda's tensor approach does not account for the connectivity of fractures and can, thus, underestimate the permeability when the fracture intensity is low. However, Oda's tensor approach is much faster with acceptable accuracy on a limited number of fracture planes.

Oda's crack tensor is expressed in the integral formula, but an empirical crack tensor can be calculated as shown by Eq.2.1, by adding the individual fracture weighted by its fracture area A_k and transmissivity T_k (Dershowitz et al. 2000).

$$F_{ij} = \frac{1}{V_{cell}} \sum_{k=1}^{N} A_k T_k n_{ik} n_{jk} \tag{2.1}$$

where, F_{ij} is the crack tensor, V_{cell} is the grid cell volume and n_{ik}, n_{jk} are the components of a unit normal to the fracture *k*.

Oda's permeability tensor is derived from crack tensor F_{ij} by assuming that crack tensor expresses fracture flow as a vector along the unit normal direction of the fractures. With the assumption that fractures are impermeable in the direction which is parallel to their unit normal, crack tensor needs to be rotated into the planes of fracture to obtain the permeability tensor (Eq.2.2).

$$k_{ij} = \frac{1}{12}\left(F_{kk}\delta_{ij} - F_{ij}\right) \tag{2.2}$$

where, δ_{ij} is Kronecker delta function and F_{kk} is the summation of three principal component of the crack tensor F_{ij} (i.e. $F_{kk} = F_{11} + F_{22} + F_{33}$).

2.3.2 Proppant and Fluids Calculation

In this study, we assume simple Khristianovic-Geertsma-de Klerk (KGD) fracture geometry. With desired fracture geometry, the total volume of hydraulic fractures per stage can be calculated using Eq.2.3,

$$V_p = 2x_f w_f h_f \tag{2.3}$$

where, x_f , w_f , and h_f are fracture half-length, fracture height and average width, respectively. The proppant mass M_p per stage then can be calculated with Eq.2.4, where ρ_p is proppant density, and ϕ_p is porosity of proppant.

$$M_p = V_p(1-\phi_p)\rho_p \tag{2.4}$$

With specified fluids pumping rate, the pumping time can be estimated by applying material balance equation to fluids leakage (Eq.2.5).

$$q_{inj}t_{inj} - \kappa(2h_f x_f)C_L\sqrt{t_{inj}} - (2h_f x_f)S_p - x_f w_f h_f = 0 \tag{2.5}$$

where, q_{inj} is injection rate per half fracture of a bi-winged fracture, t_{inj} is injection time, κ is the opening time distribution factor, C_L is the fluid leak-off coefficient for the formation, and S_p is spurt loss coefficient. Then, the total proppant slurry volume and total fracturing fluid volume per fracture stage can be determined by the following Eq.2.6 and Eq.2.7:

$$V_{slurry} = 2q_{inj}t_{inj} \tag{2.6}$$

$$V_{fluid} = 2q_{inj}t_{inj} - \frac{M_p}{\rho_p} \tag{2.7}$$

2.3.3 Extension of DToF-based Simulation to Dual Porosity System

In fractured reservoir, natural fractures will reopen and contribute to fluid flow during the hydraulic fracturing process. Generally speaking, dual porosity model (Warren and Root 1963), rather than single porosity model, is more suitable to characterize and model naturally fractured reservoir. Dual-porosity modeling is computationally inexpensive and structurally simplified compared direct modeling with the discrete fracture networks (DFN). In dual porosity model, the fracture system is highly conductive but can store little fluid due to its very low porosity; whereas the matrix system has low conductivity and large storage capacity compared to fracture system.

The fluid transport equation in the fracture system is given by Eq.2.8, with a mass transfer term connecting to the matrix:

$$\frac{\partial(\rho\phi_f)}{\partial t} - \nabla\cdot\left(\frac{\rho}{\mu}k_f\nabla p_f\right) = -\rho_{up}\sigma\frac{k_m}{\mu_{up}}(p_f - p_m) + \rho q_f \tag{2.8}$$

The fluid transport equation in the matrix is given by Eq.2.9:

$$\frac{\partial(\rho\phi_m)}{\partial t} = \rho_{up}\sigma\frac{k_m}{\mu_{up}}(p_f - p_m) \tag{2.9}$$

where, ρ is the fluid density, ϕ represents porosity, q_f is the sink/source term, μ stands for fluid viscosity and k denotes the permeability. Subscript f stands for the fracture and m represents the matrix. The right hand side of Eq.2.9 is the mass transfer term between fracture and matrix (Kazemi et al. 1976), among which σ is called shape factor that defines the connectivity between the matrix block and the surrounding fracture network.

As fluid flow only happens in the fracture system, the pressure propagation is solved with FMM in fracture system, where the drainage volume as a function of DToF is calculated. When solving the fluid flow equation to estimate the reservoir performance, we assume the matrix properties (i.e., porosity, permeability, and shape factor) are spatially uniform. Eq.2.8 and Eq.2.9 are transformed into τ coordinate for the DToF-based 1D flow simulation. After the τ coordinate transformation, the mass balance equation in fracture takes the following form as Eq.2.10 (Fujita et al. 2016), where $\phi_{f,ref}$ denotes the fracture porosity at the reference pressure. The matrix equation can be written as Eq.2.11. The dual porosity system on the DToF coordinate is illustrated in Figure 2.1, where the fracture network is the system through which the pressure front primary propagates and the matrix serves as a fluid source to the fracture system.

$$\frac{\partial}{\partial t}\left(\frac{\phi_f}{B}\right)-\frac{\phi_{f,ref}}{w(\tau)}\frac{\partial}{\partial \tau}\left(w(\tau)\frac{(\mu c_t)_{init}}{\mu B}\frac{\partial p_f}{\partial \tau}\right)=-\sigma\frac{k_m}{\mu B}(p_f-p_m)+\frac{q_f}{B} \tag{2.10}$$

$$\frac{\partial}{\partial t}\left(\frac{\phi_m}{B}\right)=\sigma\frac{k_m}{\mu B}(p_f-p_m) \tag{2.11}$$

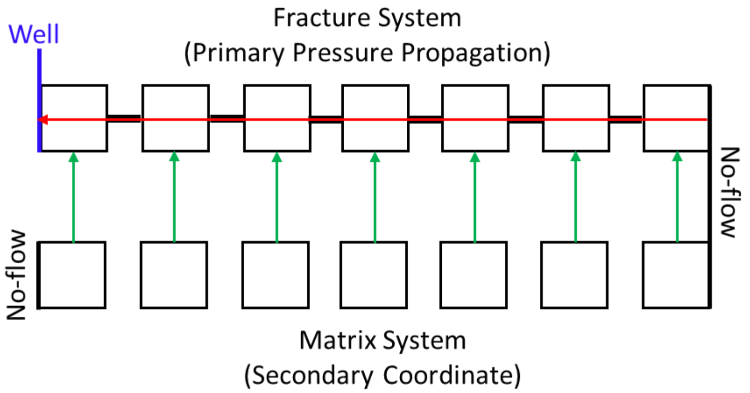

Figure 2.1 Dual-porosity system on the DToF coordinate (adapted from Fujita et al. (2016))

Here, we demonstrate the DToF-based dual porosity simulation model with a naturally fractured gas reservoir. The reservoir size 1990*ft*, 1990*ft*, and 50*ft* along *x*, *y*, and *z* directions respectively. A vertically completed well sits in the middle of the reservoir. The simulation model is comprised of total $199\times199\times10$ grids, where the first five layers are the matrix system, and the other five layers represent the fracture system. Figure 2.2 shows the permeability and porosity distribution in the fracture system. The fracture permeability ranges from 0.032 to 0.493 *md* in *x* direction, 0.032 to 0.498 *md* in *y* direction, and 0.0034 to 0.0634 *md* in *z* direction. Porosity ranges from 0.97% to 12%. The initial reservoir pressure is 5470 *psi* and the model is simulated at constant bottom-hole pressure (2000*psi*) constraint for five years. Other key parameters are listed in Table 2.1.

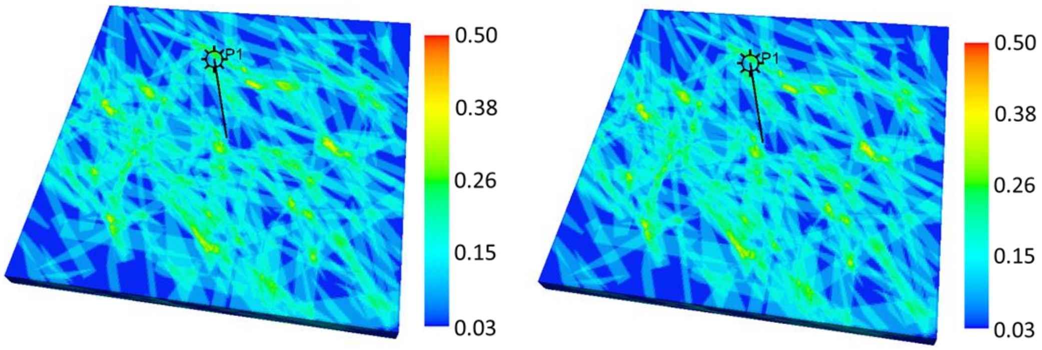

a) PERMX b) PERMY

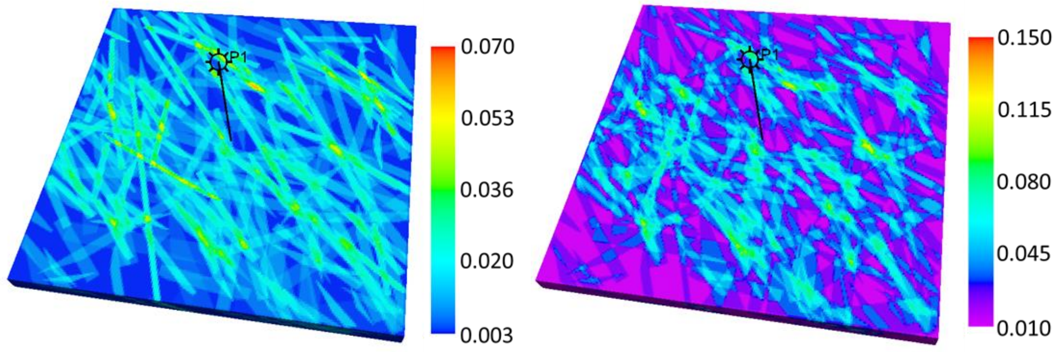

c) PERMZ d) PORO

Figure 2.2 Distribution of the fracture permeability and porosity for synthetic model

Table 2.1 Parameters used in synthetic dual porosity model

Reservoir size	1990×1990×50 ft^3
Matrix porosity	0.1
Matrix permeability	0.0001 *md*
Initial pressure	5470 *psi*
Rock compressibility(at p_{init})	1.0×10^{-6} psi^{-1}
Shape factor	0.15
Wellbore radius	0.5 *ft*
Bottom-hole pressure	2000 *psi*

After running FMM, the drainage volume as a function of DToF is shown in Figure 2.3 (red circle). It is observed that the drainage volume increases monotonically with increasing DToF; however, the rate of drainage volume growth (Eq.1.7), named drainage volume derivative, is not uniform and is controlled by the reservoir heterogeneity and the finite reservoir size. The drainage volume derivative falls to zero at late DToF because the pressure feels all boundary of the finite reservoir volume.

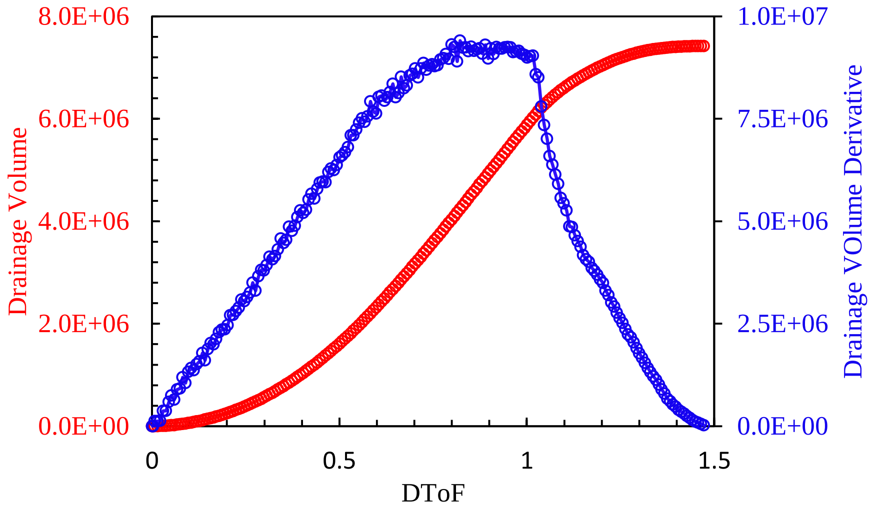

Figure 2.3 Drainage volume and drainage volume derivative as a function of DToF

Figure 2.4 shows the gas production rate comparison between the DToF-based simulation and finite difference simulator (ECLIPSE here). From the figure, we see a good agreement. Regarding computational efficiency, the DToF-based simulation only takes 13 seconds while ECLIPSE takes 124 seconds in this case, which is about ten times speedup. The computational complexity of DToF-based simulation is $O(N \log N)$, while that of the finite difference simulation is $O(N^2)$, thus the computational advantage of DToF-based simulation will continuously increase as the number of simulation cell N increases.

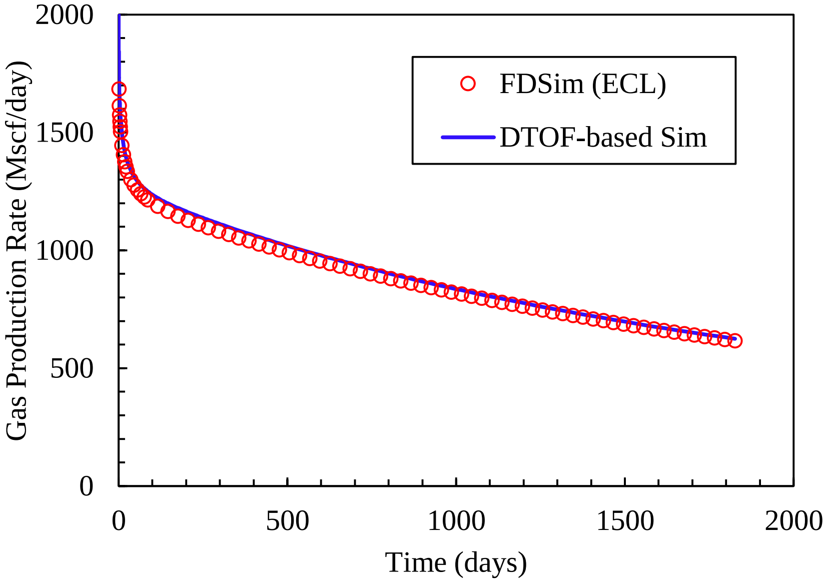

Figure 2.4 Gas production rate comparison for the synthetic dual porosity model

2.3.4 *Optimization Algorithm and Workflow*

To optimize the placement of multi-stage hydraulic fractures, a class of evolutionary algorithms known as Genetic Algorithms (Holland 1992; Mitchell 1999) is utilized here. The genetic algorithm is based on the biological theory of evolution. This kind of evolutionary algorithms has been found to be very effective in optimization process (Cheng et al. 2008; Yin et al. 2010; Yin et al. 2011). The main advantage of evolutionary algorithms is that they are derivative free. Yin et al. (2010) and Yin et al. (2011) had successfully applied the genetic algorithm to calibrate reservoir and hydraulic fracture parameters. We follow the same GA implementation as Yin et al. (2011) for our optimization process, and the workflow for GA is sketched in Figure 2.5.

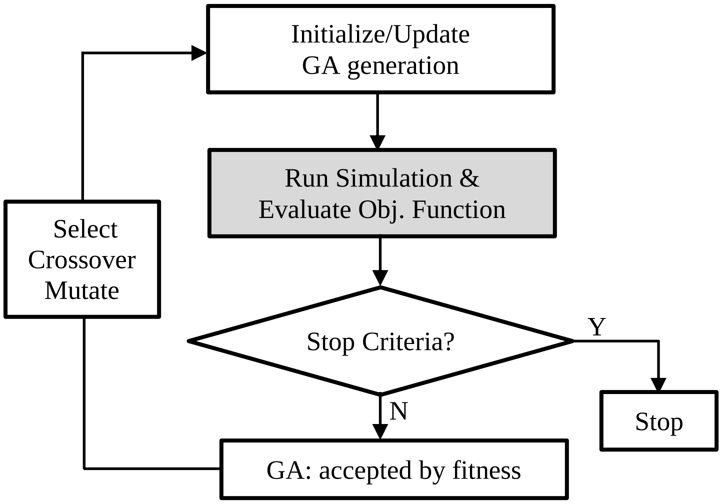

Figure 2.5 General workflow for Genetic Algorithm (GA)

The objective function evaluation process in Figure 2.5 is expanded in detail in Figure 2.6. We start with the parameters describing the number of hydraulic fractures, fracture spacing, half-lengths, and widths. The proppant and fracturing fluid are calculated with the method described above, and then the cost is estimated with assumed economic parameters. Based on reservoir model with DFN network, we upscale natural fractures to obtain properties of fracture systems using Oda’s method. Next, the gas production is predicted with DToF-based dual porosity simulation approach. With the gas production, revenue and net present value (NPV) are calculated and NPV is optimized.

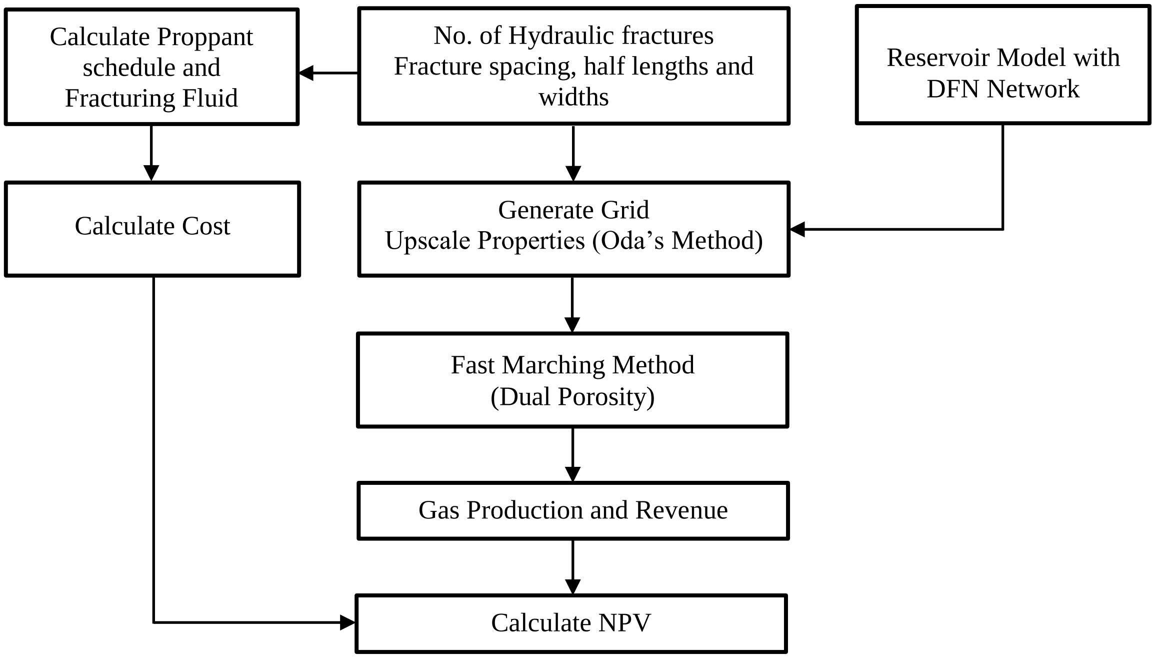

Figure 2.6 Workflow of objective function evaluation for each hydraulic fracture model

2.4 Application

To demonstrate our proposed workflow, we applied it to a synthetic multi-stage hydraulic fracture model. Discrete fracture network (DFN) is generated based on statistical properties and then upscaled to dual porosity model, with permeability upscaled by Oda's method. The DToF-based dual porosity simulation is utilized here as a rapid forward simulator. The net present value (NPV) of the model is optimized using the genetic algorithm. It is worth mentioning that our proposed workflow can easily be extended to account for the geological uncertainty, represented by different realizations of DFNs here. In that case, the objective function is calculated using the expected value on each realization with the same parameter set. The optimization results from single realization and multiple realizations are presented and compared.

2.4.1 Model Setting

The model used for this hydraulic fracture design and optimization study is a multi-stage hydraulic fractured horizontal well. It is a dual porosity model with “tartan” grid, where the grid in *y* direction is logarithmic near the fractures to provide better flow resolution. The well is BHP constrained at 3000 *psi* for first three years and then at 1000 *psi* for the rest of production time. Other parameters are given in Table 2.2.

Table 2.2 Model parameters for hydraulic fracture design and optimization

Reservoir properties	Reservoir size (*ft*)	1200×5000×60
	Simulation grid size	240×various×5
	Initial pressure (*psi*)	5000
	BHP for first 3 years (*psi*)	3000
	BHP for rest of production (*psi*)	1000
	Matrix porosity	0.076
	Matrix permeability (*md*)	0.0001
	Rock compressibility (psi^{-1})	4.0×10^{-6}
Well properties	Horizontal well length (*ft*)	4600
HF properties	HF Permeability (*md*)	1000
	HF Porosity	0.3
Fluid properties	Initial viscosity (*cp*)	0.0278
	Initial compressibility (psi^{-1})	1.2×10^{-4}

Discrete natural fractures are generated based on statistical properties of the fracture system (shown in Figure 2.7a). We assume normal distribution for the properties of the DFNs, such as natural fracture length, log-aperture, dip angle, and azimuth. Denser natural fractures are deliberately generated in two regions so as to investigate the influence of heterogeneous geologic properties (mainly fracture density) on hydraulic fracturing design. This natural fracture information is transformed into heterogeneous permeability field by applying the Oda's method, showing in Figure 2.7b (the hydraulic fractures are also shown in the figure with red line segments). For these cells without any discrete natural fractures passing through, a lower bound value of 100*nd* is assigned so as to account for the implicit natural fractures. It can be observed that the permeability field adequately captured the natural fracture information.

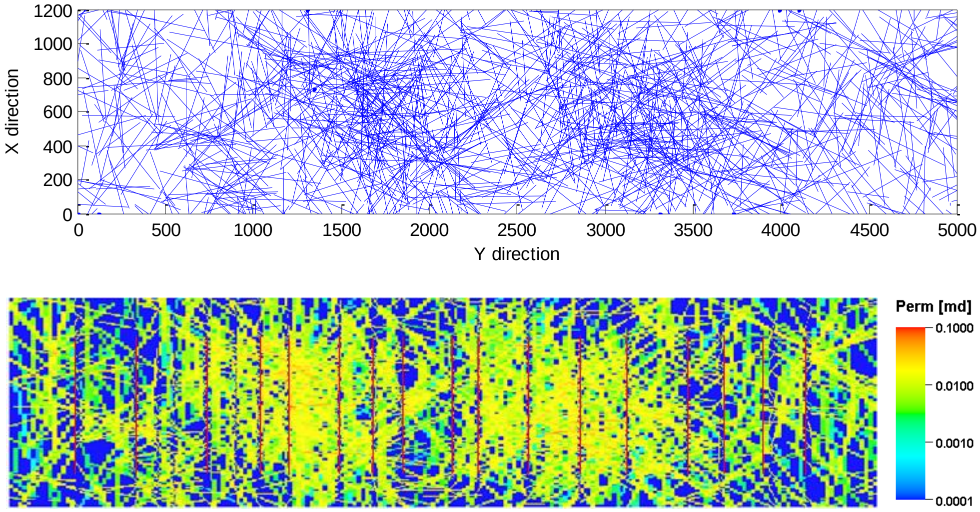

Figure 2.7 a) Discrete natural fracture networks (first layer); b) Upscaled permeability field for the fracture system (first layer)

The performance prediction of DToF-based simulation is first validated with finite difference based simulation (ECLIPSE here). In this validation, 20 hydraulic fracture stages have been used. The production rates and cumulative production comparisons are presented in Figure 2.8a and Figure 2.8b respectively. From the comparison, a reasonably good approximation is obtained and the DToF-based simulation is about 20 times faster than the ECLIPSE in this case. The computational advantage of DToF-based simulation comes from the fact that the pressure propagation process is calculated only once and then the fluid flow is computed in the transformed 1D domain.

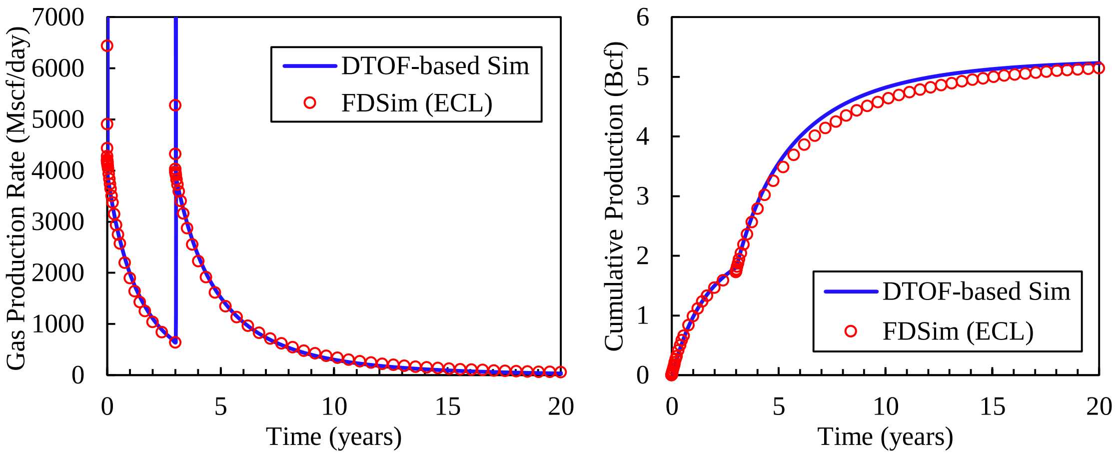

Figure 2.8 Simulation results comparison a) production rate; b) cumulative production

2.4.2 Sensitivity Analysis

After model validation, the DToF-based simulation is used to conduct the performance prediction for the rest of the study. Sensitivity analysis is first performed to analyze the relative influence of various parameters under investigation. A base value of each variable parameter is chosen, and its value is perturbed to the upper and lower limits to observe the effect on NPV once at a time. For sensitivity study, the base and perturbed values of various variables are given in Table 2.3. Hydraulic fractures are grouped into five groups here for the purpose of reducing the number of parameters during optimization. In this table, average fracture width, fracture half-lengths and fracture spacing for five groups of hydraulic fractures adjacent to each other are utilized. For all the cases, the lateral length is kept the same by rescaling the fracture spacing.

Table 2.3 Base and perturbed values for sensitivity analysis

Variable	Min Value	Base Value	Max Value
Stages Number (STAGE)	10	15	25
Avg Width (WF1 to WF5) (*ft*)	0.02	0.05	0.08
Fracture half-length (XF1 to XF5) (*ft*)	150	350	550
Fracture spacing (DIS1 to DIS5) (*ft*)	100	250	400

Table 2.4 Economic parameters used to calculate NPV

Cost of proppant (USD/ton)	400
Cost of Fracturing Fluid (USD/gal)	0.4
Price of Gas (USD/Mscf)	3.6
Horizontal Well Cost (USD/Well)	1.2×10^6
Equipment Rent (USD/min)	1250
Interest Rate (per year)	10%

The assumed economic parameters, such as the cost of well, gas sale price, the cost of fracturing fluid and proppant, are listed in Table 2.4. With these model parameters and economic parameters, the sensitivity results of NPV are shown in Figure 2.9, where the red bar corresponds to the lower bounds of the parameters, and blue bar corresponds to the upper limits of the parameters. The NPV is mainly controlled by the gas production and the completion cost. For instance, fewer hydraulic fracture stages restricts the gas production while too many stages increases the completion cost. From the sensitivity results, the number of stages, average fracture width, and the fracture half-length are the dominant parameters.

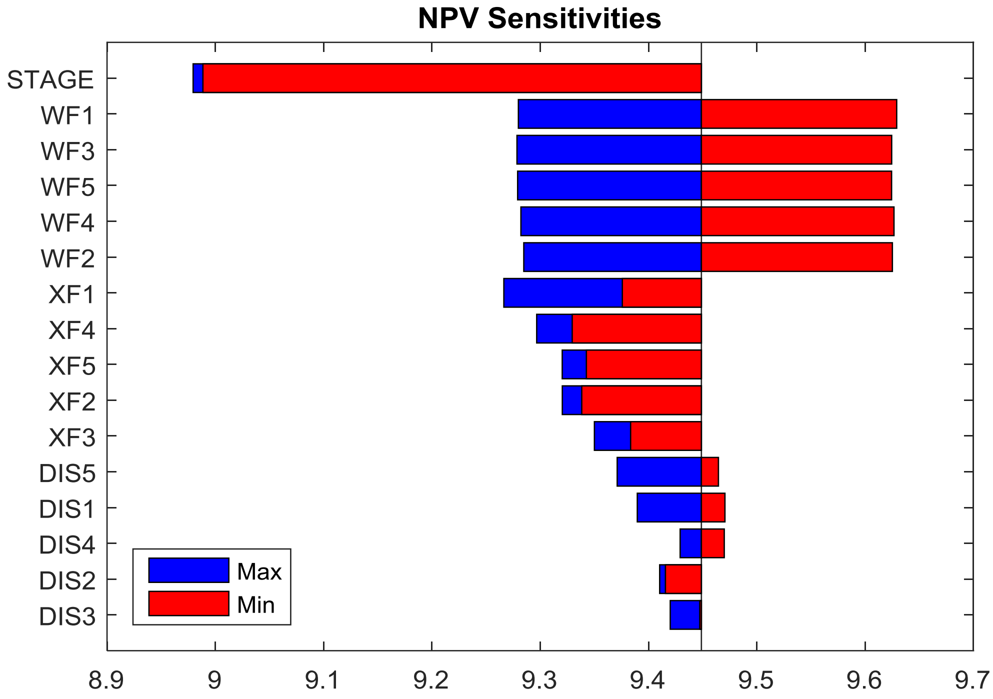

Figure 2.9 Sensitivity results of NPV on various variables under investigation

Before optimization process, we first investigate how the stage number affects the performance under uniformly distributed hydraulic fracture scenario (i.e. uniform spacing). Simulations are performed with 10, 15, 20 and 25 fracture stages. Figure 2.10 shows the gas rate production and cumulative gas production comparisons with a different number of fracture stages. As we can see from this figure, the case with a larger number of hydraulic fracture stages obtains higher gas production rate at the early time. But it will have a lower rate at the late time because the reservoir is depleted more quickly with a larger number of hydraulic fracture stages. This rate behavior gives more cumulative production at the early time for a larger number of hydraulic fracture stage case but eventually, they all reach a comparable level.

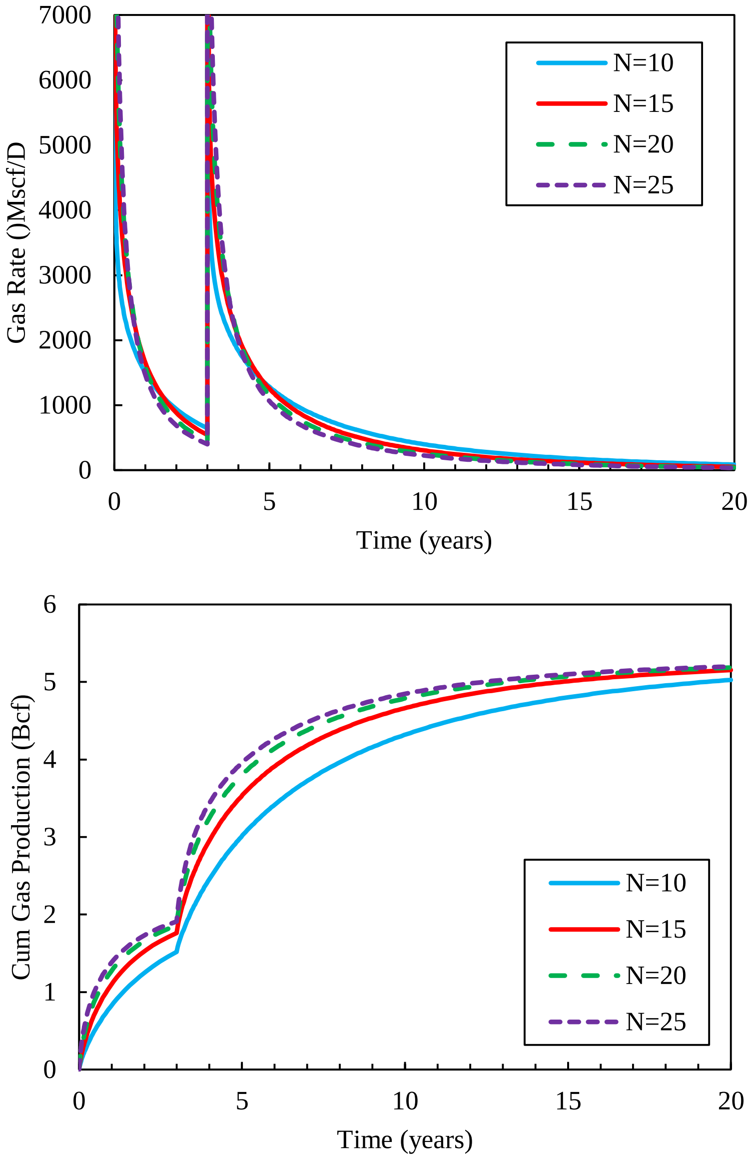

Figure 2.10 a) Gas rates comparison for various numbers of fracture stages; b) Cumulative gas production for different numbers of fracture stages

Higher production rate delievers more total revenue, accounting for the discounted interest rate. But it costs more as well to obtain higher production rate. Then, where is the balance point? Figure 2.11 shows the comparison between NPV and cost of different hydraulic fracturing stage numbers. It can be seen that the total revenue (NPV plus cost) increases with the number of fracture stages. But the cost of the fracturing job also increases significantly, thus the NPV decreases after a certain point. It can be observed that the optimum number of fracture stages is around 15 to 20 for this study case under the uniform spacing scenario.

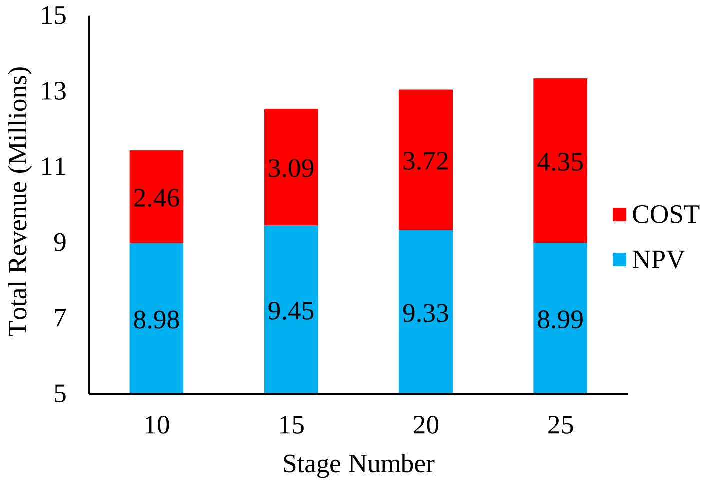

Figure 2.11 NPV vs Cost comparison for cases with various number of fracture stages

2.4.3 Optimization Results

Next, we perform hydraulic fracturing placement optimization study by simultaneously changing all the variables used in the sensitivity analysis. The genetic algorithm (GA) is deployed for optimization process as described above. A total of 15 generations with a population of 70 in each generation is used. The number of fracture stages could vary between 10 and 25. All other variables have same value ranges as given in Table 2.3. Since this study involves a large number of forward simulations, the DToF-based forward simulation is used for its computational advantage. Figure 2.12 shows that overall NPV increases with the number of generations in the GA. Also, with the progress of generations, more samples get closer to higher NPV values.

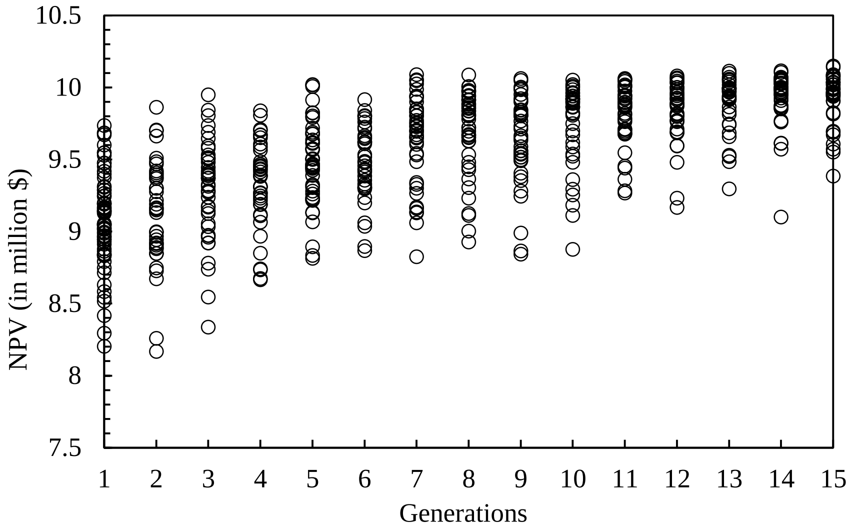

Figure 2.12 Genetic algorithm optimization results based on single realization

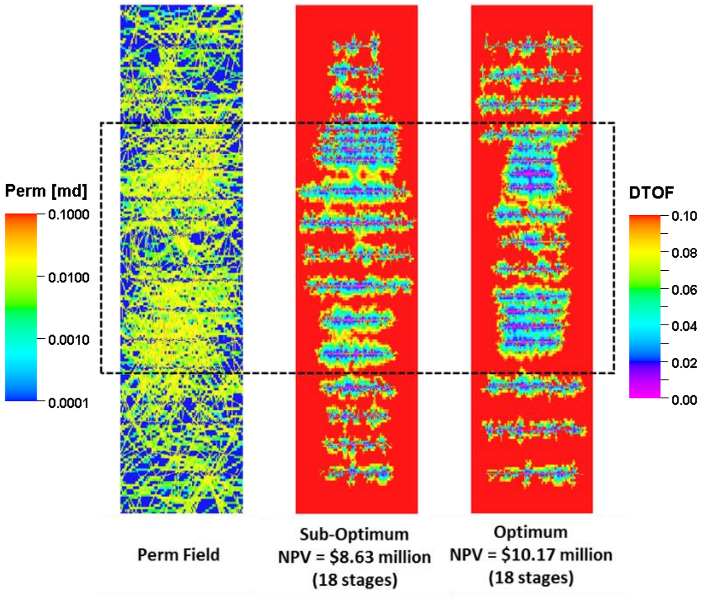

Figure 2.13 a) Permeability field; b) DToF map with sub-optimum hydraulic fracture design; c) DToF map with optimum hydraulic fracture design

From the simulations, the best model is picked based on the maximum NPV (18 stages with $10.17 million), and it is compared with one suboptimum case which has the same number of stages but just delivers an NPV of $8.63 million. The comparison confirms that the NPV can be increased by reallocating the hydraulic fractures, proppant, and fluids. The difference between the hydraulic fracture placements can be visualized using the diffusive time of flight map (Figure 2.13), which is a visual and intuitive display of the pressure propagation and drainage volume information. By comparing the permeability field (Figure 2.13a) and DToF map (Figure 2.13c), we observe the fractures in the high permeability region are wider but shorter and the fractures in the low permeability region are narrower but longer.

We also plot the parameter distributions from the first generation and selected 70 good matched models, as shown in Figure 2.14. Here, the parameters are normalized by its min and max value to fall between zero and unity. The blue boxes indicate the 25 percentile and 75 percentile of model parameters in the population and the red lines are the median. From Figure 2.14a, we see that the parameter distribution is quite uniform in the first generation; however, Figure 2.14b displays that the better-performed models show a preference for the parameters. Most of the models have 20 stages. It is also worth to notice that the fractures in the second group, which locate in high permeability region, have larger fracture width (larger *WF2*) with shorter half-length (smaller *XF2*); while, the fractures in the first and fifth group, which locate in low permeability region, have smaller fracture width (smaller *WF1*, *WF5*) with longer half-length (larger *XF1*, *XF5*). This can be illustrated from the diffusive time of flight map as well (Figure 2.13c). It suggests that in the high permeability region, the conductivity of the fracture is more important, and shorter length can help save the completion cost. While in the low permeability region, creating more fracture surface area (longer half-length but smaller fracture width) can help improve the reservoir performance.

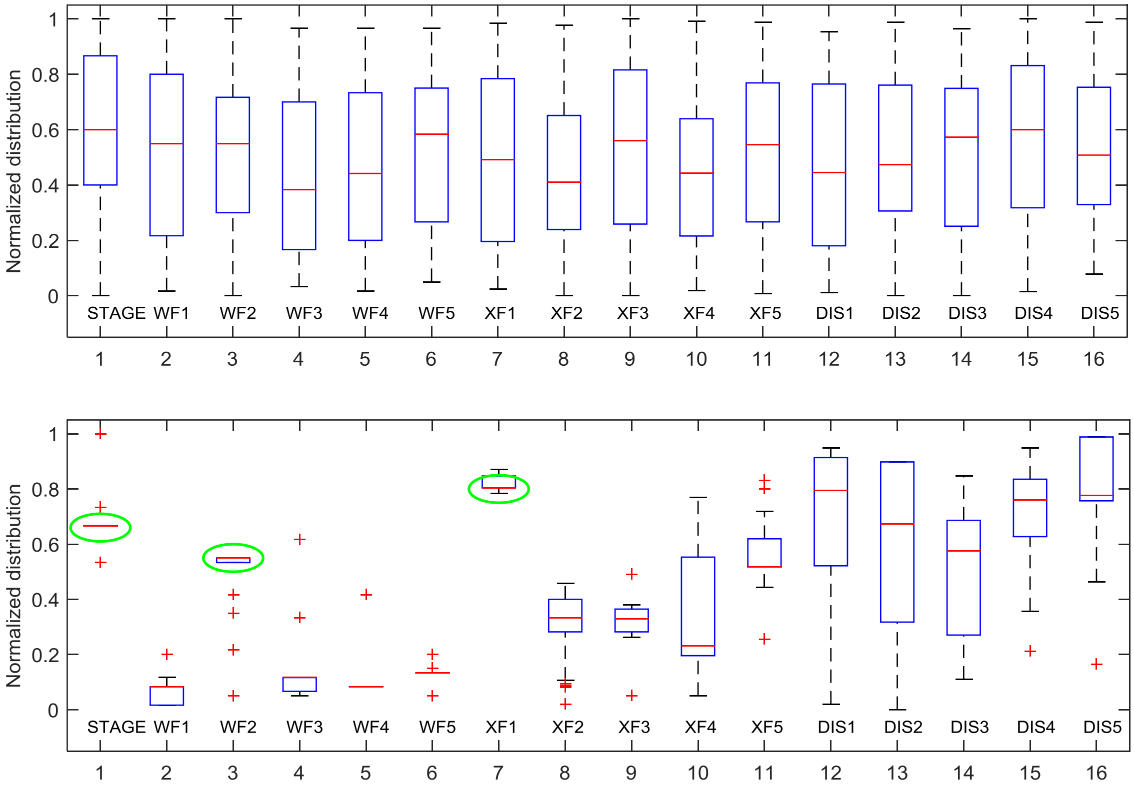

Figure 2.14 Normalized parameter distribution for a) first generation; b) selected 70 models

2.4.4 *Effects of Geologic Uncertainty*

The results discussed above assume that the locations of natural fractures are known as a priori with a reasonable degree of confidence. In practice, we can infer the natural fracture information near the wellbore, and natural fractures far away cannot be accurately characterized. If the locations of natural fractures are not known, it may lead to a suboptimal design with a much lower NPV. To take into account the effect of uncertainty in natural fracture locations, we performed the optimization simultaneously on different geologic realizations. In our study here, 12 different realizations (Figure 2.15) are generated, including the natural fracture realization in the previous subsection. The same optimization algorithm discussed earlier is applied except that the objective function used now is the expected value (shown by Eq.2.12) of the NPVs of the 12 realizations for the same given set of parameters. The results of the genetic algorithm are presented in Figure 2.16. The maximum NPV from the optimization is \$10.08 million, which is not as high as that in Figure 2.12 because of the compromised uncertainty in the natural fractures.

$$NPV = \frac{1}{N}\sum_{i=1}^{N} w_i \cdot NPV_i \tag{2.12}$$

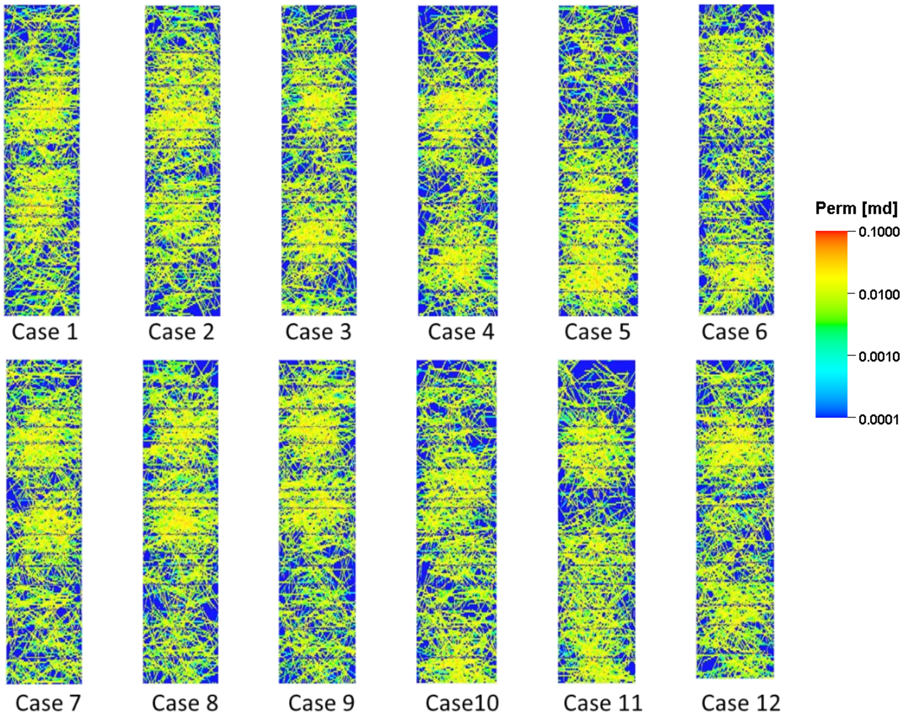

Figure 2.15 Permeability field (first layer) of twelve different realizations

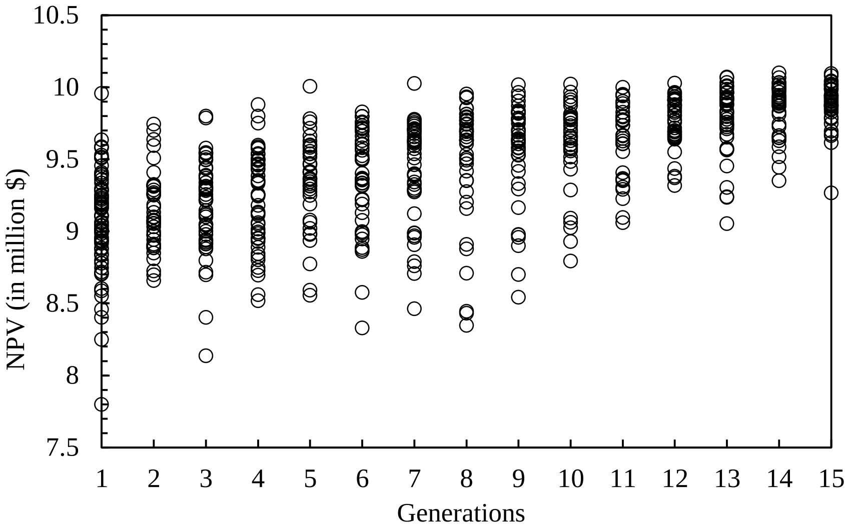

Figure 2.16 Genetic algorithm optimization results based on twelve realizations

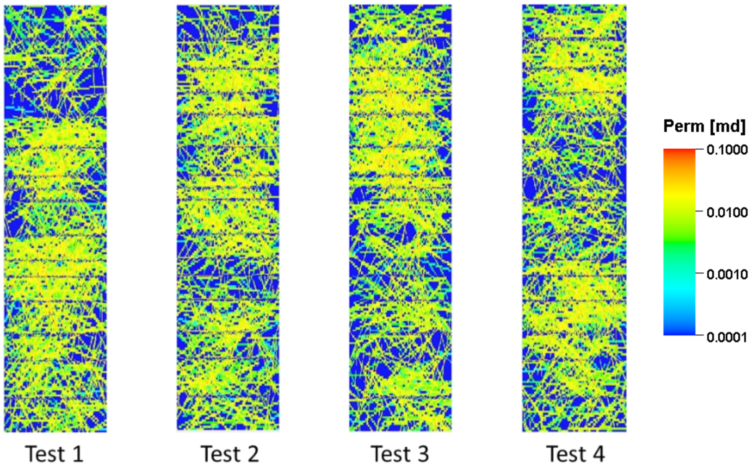

Figure 2.17 Four different blind test models for evaluating the robustness of the proposed optimization workflow

To validate the robustness of proposed optimization workflow with uncertainty, another four different realizations are created (Figure 2.17) as blind test models and four best designs from single realization and multiple realization optimizations are applied on each of them. Table 2.5 summarizes the NPVs of individual model after applying these designs and the average values across the four test models. It can be observed that the optimum designs also provide high NPV on the blind test models and the variability in NPV is relatively small. It is also worth noticing that when the optimization process considers the uncertainty of natural fracture locations using multiple realizations, the performance is superior to using single realization (relatively higher average NPV values).

Table 2.5 NPV (million) for different blind test models

Parameter Set	Test 1	Test 2	Test 3	Test 4	Average
Para 1 (single)	10.119	10.205	10.106	10.102	*10.13*
Para 2 (single)	10.067	10.150	10.079	10.141	*10.11*
Para 3 (single)	10.040	10.199	10.155	10.069	*10.12*
Para 4 (single)	10.052	10.218	10.173	10.030	*10.12*
Para 1 (multiple)	10.108	10.209	10.155	10.075	**10.14**
Para 2 (multiple)	10.212	10.209	10.159	10.172	**10.19**
Para 3 (multiple)	10.079	10.271	10.163	10.143	**10.16**
Para 4 (multiple)	10.160	10.205	10.142	10.121	**10.16**

2.5 Conclusions

In this chapter, we extend the DToF-based simulation to dual porosity system and apply it as the rapid forward simulator for the multistage hydraulic fracture design and optimization. The Oda’s method is used for calculating the permeability for fracture system from DFN, and the proppant and fluids required for hydraulic fracturing are calculated through material balance. The optimization process is carried out through a derivative-free evolutionary algorithm, genetic algorithm. We demonstrate the proposed workflow with a synthetic multistage hydraulic fracture model and show the capability to account for the geologic uncertainty (DFN distribution here).

The main conclusions from this study can be summarized as follows:

(1) DToF-based simulation is demonstrated to be an efficient approach to compute the well performance in unconventional reservoirs and shows good agreement with commercial finite difference simulators at a fraction of computation time. Two big advantages of this method are its computational efficiency and its capability of intuitively visualizing the well drainage volume.

(2) Given reservoir and horizontal well conditions, more stages of hydraulic fractures can lead to higher early production rate and higher revenue. However, the associated cost with more stages of hydraulic fractures increases as well. For a particular problem, optimum fracture stage number exists.

(3) With a reasonable knowledge of the natural fracture distribution, our proposed workflow can help obtain an optimum hydraulic fracture design. Based on our observations, the optimum design emphasizes the conductivity more for hydraulic fracture located in high permeability region, while it prefers more fracture surface area in low permeability region.

(4) When there is considerable uncertainty associated with the natural fracture distributions, multiple realizations can be included in our proposed workflow by applying the same parameter set simultaneously on each realization and evaluating the objective functions based on the expected value. From our study, the optimum design with consideration of the uncertainty provides superior results on blind test models.

CHAPTER III

EXTENSION OF THE DTOF-BASED SIMULATION WORKFLOW TO FRACTURED RESERVOIR WITH UNSTRUCTURED GRIDS[*]

3.1 Introduction

Our previous study demonstrated the DToF-based simulation to be an efficient approach for unconventional reservoir modeling; however, this workflow is currently limited to structured grids. This chapter extends the DToF-based simulation to unstructured grid system so as to better model the fractured reservoirs. On top of our previous experience with DToF-based simulation, the unstructured mesh generation and local Eikonal equation solver are the essential parts of this chapter. Force-equilibrium algorithm is utilized to provide unstructured grids with good mesh quality. The local Eikonal equation solver based on Fermat's principle and Eulerian discretization are investigated and compared. Through the numerical examples, the proposed method is demonstrated to be an efficient approach to simulate the naturally fractured reservoirs.

3.2 Background

In naturally fractured reservoirs, complex fracture networks are induced due to the interaction between hydraulic fractures and natural fractures. It is feasible to characterize the statistical properties of the natural fractures from outcrop, image-log, and core

---

[*] Part of data reported in this Chapter is reprinted with permission from "Rapid Simulation of Naturally Fractured Unconventional Reservoirs with Unstructured Grids Using the Fast Marching Method" by Yang, C., King, M. J., & Datta-Gupta, A. (2017), paper SPE-182612-MS presented at the SPE Reservoir Simulation Conference, 20-22 Feb., Montgomery, Texas, USA. Copyright [2017] SPE.

analysis. Based on these statistical properties, Kim and Schechter (2009) developed a fractal discrete fracture network model, which can generate multiple realizations of the natural fracture system. The evolving technology of micro-seismic event measurements has been used to capture complex fracture system (Cipolla et al. 2012; 2011).

Despite the capability to detect and characterize the complex fracture systems, the industry is still struggling to efficiently and accurately simulate the fractured reservoir with complex fracture network. Traditionally, a fractured reservoir is modeled with a dual-porosity model (Warren and Root 1963) or dual permeability model. However, as discussed by Kuchuk and Biryukov (2014), the dual-porosity model cannot capture the behavior of most fractured reservoirs, with one limitation being due to the assumption of uniformly distributed well-connected orthogonal fractures. Continuous representation methods, such as multiple interacting continua, will have similar issues.

Discrete fracture models (DFM) provide a better representation of the fracture geometry. In DFM, the discrete fractures are modeled either implicitly by modifying the transmissibility lists (Branets et al. 2009; Mallison et al. 2010) or explicitly with high permeability Voronoi cells (Cipolla et al. 2011; Sun and Schechter 2015), and the fluid flow equation is solved using finite volume simulation. One common drawback of the conventional simulation method with unstructured grids is the substantial computational cost. The embedded discrete fracture model (EDFM) can incorporate the effect of each fracture without an explicit simulation mesh (Lee et al. 2001; Li and Lee 2008), which is computationally efficient. However, the performance of EDFM highly depends on how accurately the modified transmissibility can capture the effects of the fractures.

Combining the advantages of unstructured grids and the DToF-based simulation, we propose the rapid simulation workflow for modeling naturally unconventional reservoirs. Unstructured grids allow better characterization of the transient drainage volume for complex fracture systems while the DToF-based simulation provides a rapid simulation of reservoir performance based on the transient drainage volume (YangKing et al. 2017). As mentioned earlier, two essential parts of this work include the generation of unstructured mesh and local Eikonal equation solver.

3.3 Generating Unstructured Grids

Since fracture systems are too complex to be accurately modeled with Cartesian and corner-point grids, unstructured grids, such as Voronoi grids, are considered as more appropriate discretization schemes. However, it is a crucial and challenging task to obtain unstructured grids with good mesh quality because highly skewed cells are inhibitive for either conventional finite volume simulation or our DToF-based simulation. Highly skewed cells will increase the inaccuracy of flux calculation in additional to the increased computational burden posed by the Courant-Friedrichs-Lewy (CFL) condition. For DToF-based simulation, the highly skewed cells will increase the possibility of violating the causality requirement while solving the Eikonal equation with FMM.

3.3.1 Mesh Generation Overview

Heinemann et al. (1991) first introduced the unstructured grid system to the petroleum industry. In their paper, they discussed the grid-construction method and finite volume flow discretization. Karimi-Fard et al. (2004) proposed a scheme to discretize fracture networks, and Branets et al. (2009) defined protection areas around fractures to handle the fracture intersections. Olorode et al. (2013) modeled nonplanar fractures and performed a high-resolution numerical study of the behaviors. Sun and Schechter (2015) presented a very comprehensive study with Voronoi grids which can characterize fractures with non-uniform aperture, which allows more accurate representation of unpropped fractures.

The local orthogonality of Voronoi grids is appealing to reservoir simulation since it reduces the grid orientation effects. As the Voronoi grid is the dual of the Delaunay triangulation, a well-shaped Delaunay triangulation is the first step to constructing Voronoi tessellation. According to Edelsbrunner (2001), any set of nodes in the *x*,*y*-plane can be triangulated by the Delaunay algorithm. Then the task of constructing well-shaped Voronoi grids is essential to obtain better-distributed nodes for Delaunay triangulation. Different approaches can be found in the literature to optimize the locations of triangle nodes (Field 1988; Freitag and Ollivier-Gooch 1997; Persson and Strang 2004), among which the force-equilibrium algorithm proposed by Persson and Strang (2004) tends to produce meshes with better quality and uniformity.

The workflow to generate unstructured grid is sketched in Figure 3.1, with the force-equilibrium algorithm as the key optimizer. This workflow starts with assigning the fixed nodes and flexible nodes, and then Delaunay triangulation is performed based on current nodes distribution. The locations of the flexible nodes are optimized with the force-equilibrium algorithm, which will be discussed in detail later. The optimization process will iterate until desired mesh is obtained or stop criteria is reached. Finally, the Voronoi cell is generated based on the optimized Delaunay nodes.

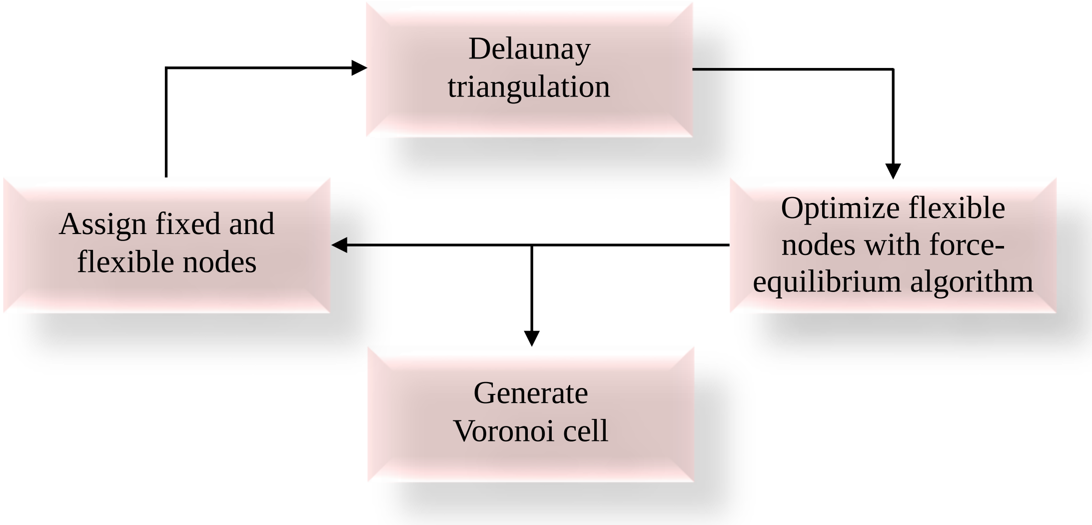

Figure 3.1 Workflow to generate Voronoi cell with force-equilibrium algorithm

3.3.2 Assignment of Fixed Delaunay Nodes

As mentioned above, one should design the fixed nodes to create protection areas so as to maintain the characteristics of the mesh objects, which here are complex fracture networks. The following procedure is implemented to design the fixed nodes for modeling complex fracture systems with intersections (note that hydraulic fracture and natural fractures are treated in the same manner):

(1) Each single fracture is first divided into fracture segments at intersections and fixed Delaunay nodes are placed at fracture tips and fracture intersections.

(2) Then, each fracture segment is further divided into fracture sub-segments based on user-defined interval size or minimum grid size.

(3) For each fracture sub-segment, three fixed Delaunay nodes are designed with the distance of fracture width (or aperture), with one node for the fracture grid block and the other two for the matrix grid blocks.

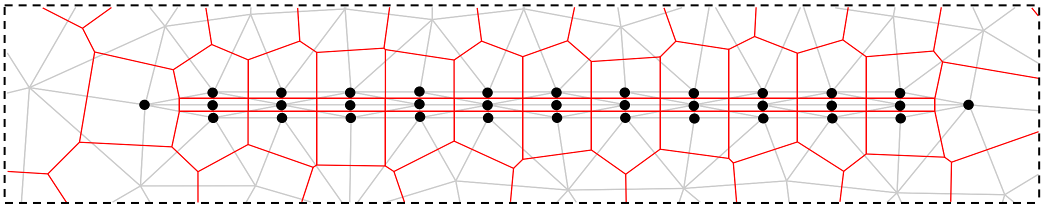

Figure 3.2 Illustration of assigning fixed points to represent fracture segment

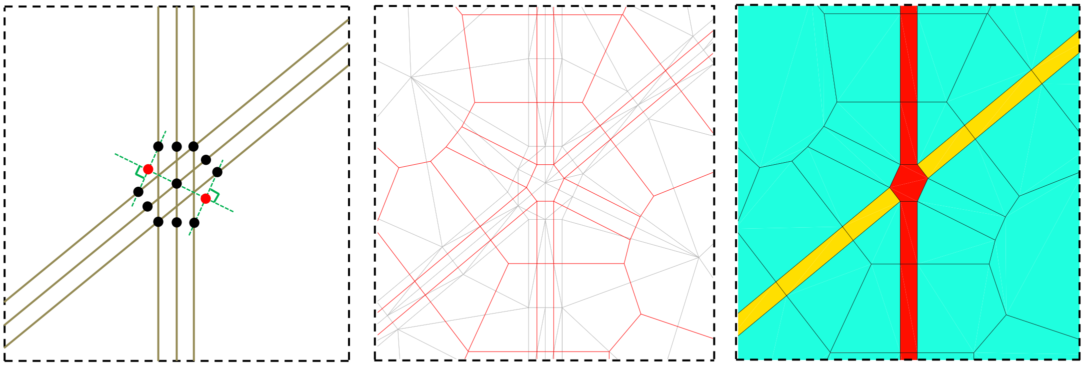

Figure 3.3 Illustration of fracture intersection: a) proposed fixed points; b) corresponding Voronoi cell; c) property (permeability) field

Figure 3.2 illustrates how a single fracture, without any intersections, is designed. The gray lines show the Delaunay triangulation and the red lines depict the corresponding Voronoi cells. It is worth mention that we have proposed a novel scheme to handle fracture intersections. As illustrated in Figure 3.3a, the fixed nodes of Delaunay triangulation are placed starting from the acute intersecting angle perpendicular to all other representing lines. Additional fixed nodes are placed at the intersection of central lines and the normal projection locations. Figure 3.3b displays the resulting Voronoi cells. Figure 3.3c shows how reservoir properties (e.g. permeability) are assigned to the intersection cells. Specifically, properties will take the higher value from the two fractures. We can observe that the intersecting Voronoi cell introduces minimum geometry alteration and maintains the same connecting surface area corresponding to each fracture. This assignment of fixed nodes can work well for small angle intersections.

3.3.3 Force-equilibrium Algorithm

After assigning all the fixed nodes, the force-equilibrium algorithm is applied to optimize the locations of the flexible nodes, following Persson and Strang (2004). This force-equilibrium algorithm is based on a mechanical analogy between a triangular mesh and a truss structure, where the edges of the triangles correspond to bars, and the vertices of the triangles are considered as joints of the truss (Persson and Strang 2004). The force displacement of each bar is calculated based on the difference between its current length and its unextended length (or desired edge length). The hope of the force-equilibrium algorithm is that the relative lengths of all the bars at equilibrium could be as close as possible to the desired relative size, which is a function of the position specified by the user and controls the eventual Voronoi cell size. The desired relative size (or Voronoi cell size) increases away from the mesh objects, which here are hydraulic fractures and natural fractures, following a predefined distance function.

The above force-equilibrium problem is a static equilibrium problem. However, to numerically solve this problem, an artificial time-dependent ordinary differential equation (Eq.3.1) is introduced:

$$\frac{d\vec{p}}{dt} = \vec{F}(\vec{p}),\ t \geq 0 \tag{3.1}$$

Here $\vec{p}$ denotes a $N \times 2$ vector array, consisting of the *x*-and *y*-coordinates of all N mesh-points. $\vec{F}(\vec{p})$ is the force vector at corresponding nodes and t is (artificial) time.

$$\vec{p}_{n+1} = \vec{p}_n + \Delta t \cdot \vec{F}(\vec{p}_n) \tag{3.2}$$

The forward Euler discretization can be applied to approximate the differential equation, as shown by Eq.3.2, where Δt is the discretized (artificial) time. Eq.3.2 is iteratively solved until the maximum change of positions is within a tolerance, or a maximum number of iteration is reached. When evaluating the force function at the n^{th} time step, the positions $\vec{p}_n$ are known, i.e. the truss topology or Delaunay triangulation of the current node set is known. The force vector of each internal point is the summation of the force induced by all the connecting edges, as shown in Figure 3.4a. For the nodes on the boundaries of the domain, an additional external force is added in the normal direction of the boundary, as illustrated in Figure 3.4b. The magnitude of the external force is just sufficient to prevent the nodes from moving outside the computational domain.

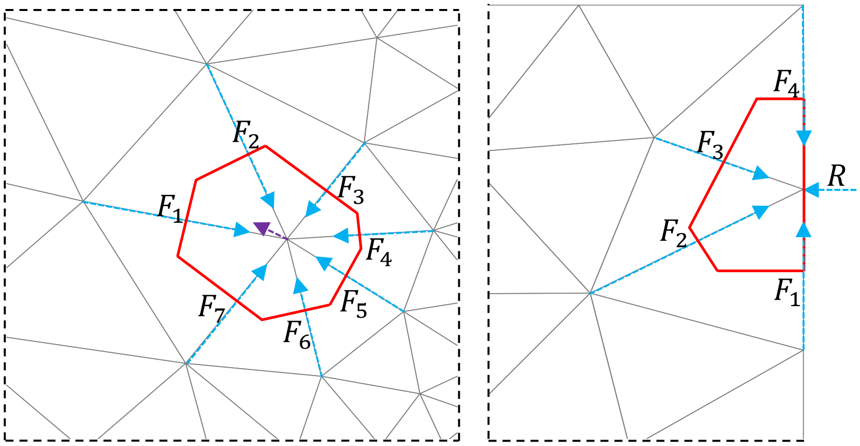

Figure 3.4 Force calculation for a) internal points b) points on the boundary

To calculate the scalar force function of each bar (triangle edge), a simple ordinary linear spring model, shown by Eq.3.3, is adopted:

$$f(l_0,l)=\begin{cases} k(l_0-l), & l<l_0 \\ 0, & l\geq l_0 \end{cases} \tag{3.3}$$

Here $f(l_0,l)$ is the internal force in each truss bar where l and l_0 represent the current edge length and the desired edge length respectively. Here k is a unit conversion factor. Note that Eq.3.3 only defines a repulsive force, which acts on the edges with a length smaller than desired edge length thereby ensuring that the nodes spread out from the mesh objects. Even though many alternatives exist and slightly nonlinear force-functions might generate better meshes, in general, the linear spring model has been demonstrated to work well (Persson and Strang 2004).

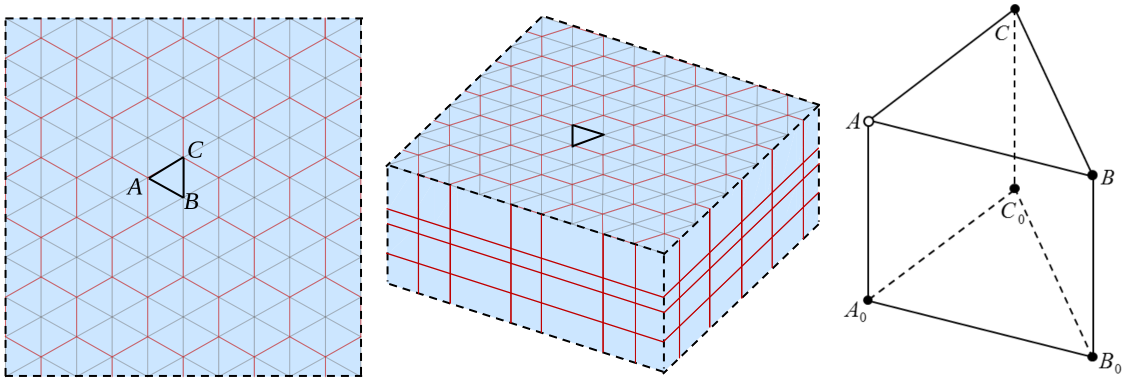

Figure 3.5 FMM computation domain: a) discretization of 2D Voronoi cells; b) 2.5D Voronoi cells; c) triangular prism

After obtaining 2D unstructured grid, 2.5D grid system can be easily constructed by assembling multiple layers and allowing vertical thickness variation. The Voronoi cells are then subdivided by connecting the centers of the Voronoi cells to the nodes of each corresponding edge (as shown in Figure 3.5a and Figure 3.5b). Any triangle in the 2D plane, for instance, *ABC* in Figure 3.5a, corresponds to a triangular prism in the 2.5D domain, shown in Figure 3.5c. The triangular prism is the basic unit of our computation domain for 2.5D unstructured grids. To update the DToF value at one particular node, we search for "virtual tetrahedrons", as the unstructured FMM local solver is constructed by the tetrahedron. For instance, to calculate the DToF value for node *A* in Figure 3.5c, the "virtual tetrahedrons" $ABCA_0$, $ABCB_0$, $ABCC_0$, and $AA_0B_0C_0$ are the candidates.

3.3.4 Illustration

Figure 3.6 shows the Delaunay triangulations of the Voronoi centers. Skewed cells can be obviously detected in Figure 3.6a for only ten iterations, and with more iterations, the triangles can be qualitatively observed well-shaped. Persson and Strang (2004) has quantitatively shown that the force-equilibrium algorithm improves both the quality and the uniformity of the mesh. The commonly used mesh quality measure is expressed by the ratio between the radius of the largest inscribed circle (times two) and the smallest circumscribed circle, as shown by Eq.3.4.

$$q = 2\frac{r_{in}}{r_{out}} = \frac{(b+c-a)(c+a-b)(a+b-c)}{abc} \tag{3.4}$$

where a, b, c are the side lengths. Higher q value corresponds to better mesh quality and $q=1$ represents an equilateral triangles. As a rule of thumb, if all triangles have $q>0.5$, the mesh quality is pretty good. Figure 3.7 shows the distribution of mesh quality for each cell after 10, 100 and 400 iterations. With more iterations, the cells obviously have better mesh quality. This observation can be reflected from the average mesh quality plot as well (Figure 3.8a).

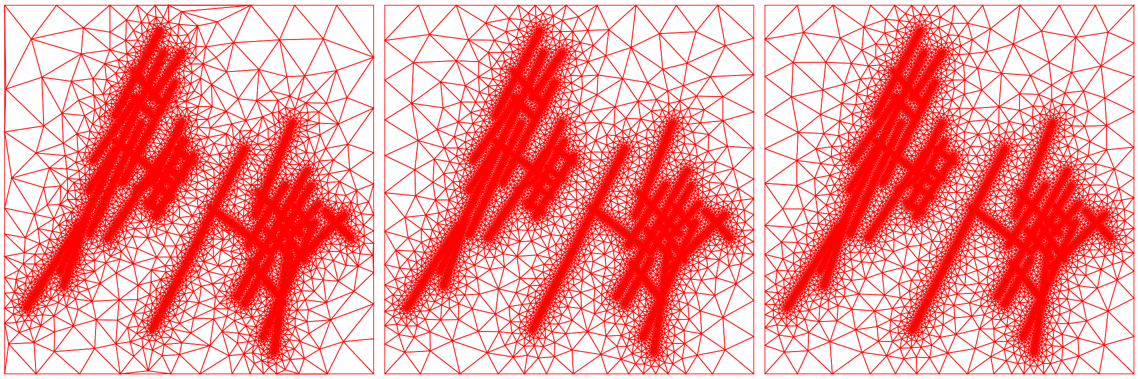

Figure 3.6 Delaunay triangulations of Voronoi centers after a) 10 iterations; b) 100 iterations; c) 400 iterations

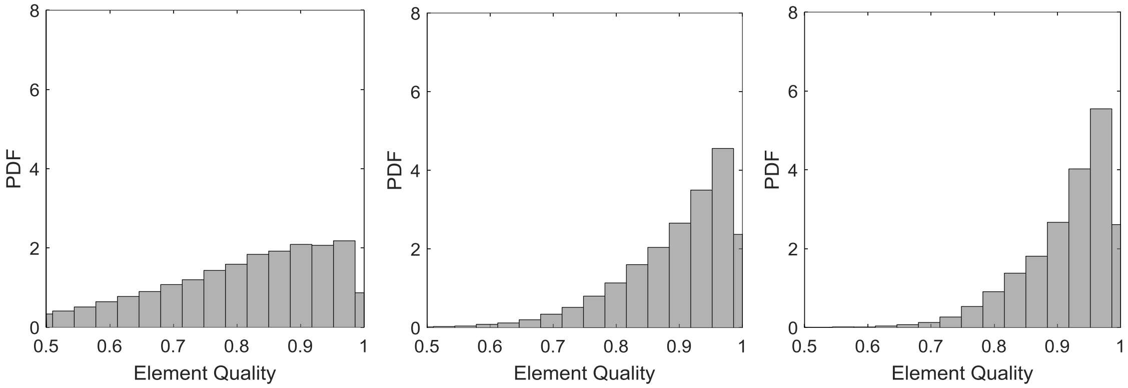

Figure 3.7 Element quality after a) 10 iterations; b) 100 iterations; c) 400 iterations

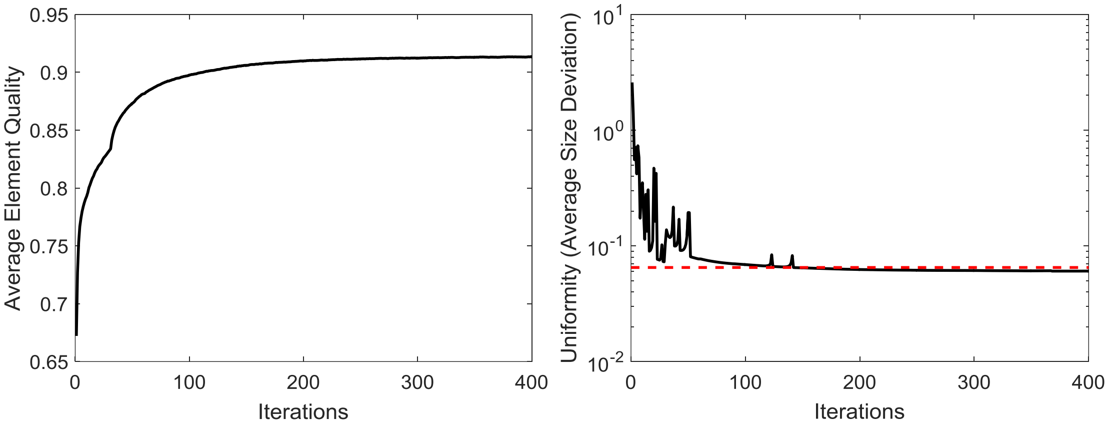

Figure 3.8 Convergence check of a) mesh quality; b) mesh uniformity

The mesh uniformity can be measured by the standard deviation of the ratio of actual sizes to desired sizes. That number is normalized by the mean value of the ratio since only the relative desired length is specified. From Figure 3.8b, we can see the average size deviations decline as a function of iterations and eventually the average size deviations are less than 6.5%.

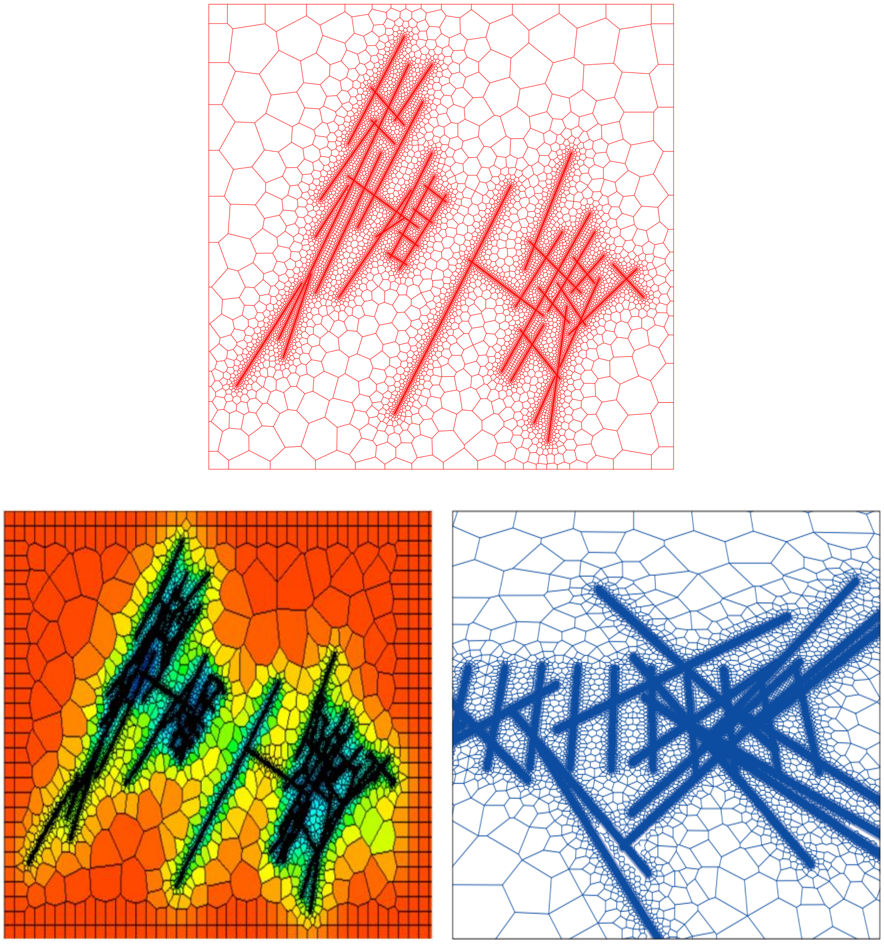

Figure 3.9 Comparison of mesh quality: a) with force-equilibrium optimization from this study; b) after Mirzaei and Cipolla (2012); c) after Kappa (2013)

After all the flexible points are determined based on the force-equilibrium algorithm, Voronoi cells can be generated based on the optimized Delaunay triangulation.

Figure 3.9 shows a comparison between the mesh from this study and other meshes from the literature for complex fracture networks, namely unstructured grids from Mangrove software and Kappa software. It is evident to notice that the Voronoi cells in Figure 3.9a are at uniform sizes at the same distance from the mesh objects. Not only are the Voronoi cells well oriented in a radial pattern around the fracture tips but also each Voronoi cell is well shaped (i.e. no highly skewed cells).

3.4 Local Eikonal Equation Solver

The main steps to implement the Fast Marching Methods in triangulated unstructured mesh remain the same as the those in the structured grid system, which has already been presented in Chapter I. The only difference is the procedure to update the value of one particular node based on the values of its neighbors.

In this subsection, we will present these two constructions in detail for both 2D triangles and 3D tetrahedron. One is based on the Fermat's principle; the other is based on Eulerian discretization. These two constructions are first presented for isotropic media, where the characteristic direction align with the DToF gradient. The local solver for anisotropic media is investigated separately. The construction based on Fermat's principle is more transparent to the physical meaning and shows the causality condition in a way much easier to be understood; however, the construction based on Eulerian discretization is found more straightforwardly be implemented and more easily be extended to anisotropic media. The causality requirement is more likely be violated in unstructured grid system or anisotropic media. Recursive Fast Marching Method is summarized for the completeness as it proves to be a good approach to deal with the causality issue.

3.4.1 Fermat's Principle

The Fermat's principle requires the ray from the source to the calculating point corresponds to the minimum arrival time. The construction based on Fermat's principle provides the first-order accuracy. Here we follow the derivation of Sun and Fomel (1998), Sethian (1999) in 2D and the derivation of Lelièvre et al. (2011) in 3D.

2D Local Solver

As shown in Figure 3.10, we assume the DToF values for nodes *A* and *B* are known and to solve for node *C*. Let $\xi (0 \le \xi \le 1)$ be the normalized distance from *A* to *S* along the segment *AB*. The DToF at point $S(\xi)$ can be approximated by the linear interpolation, shown by Eq.3.5:

$$\tau_S = (1-\xi)\tau_A + \xi\tau_B \tag{3.5}$$

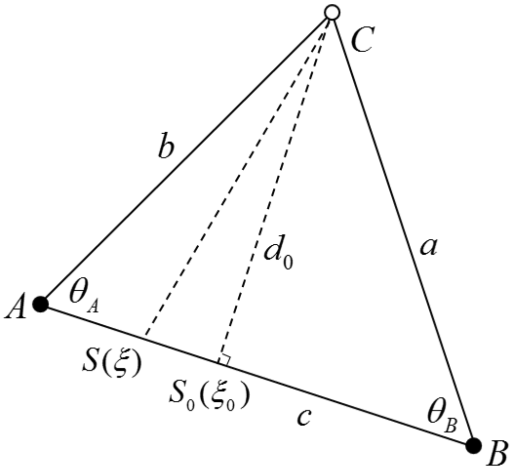

Figure 3.10 Travel-time updating procedure via Fermat's principle in 2D

According to Fermat's principle, the actual travel time to *C* corresponds to the minimum of the travel time with respect to path perturbations:

$$\tau_C = \min_{\xi \in [0,1]} \left\{ \tau_S + \sqrt{\frac{(\xi - \xi_0)^2 c^2 + d_0^2}{\alpha}} \right\} \tag{3.6}$$

where $S_0(\xi_0)$ and d_0 are the normal projection point and the distance of *C* to *AB*. α is the diffusivity. Eq.3.6 can be solved by setting the derivative to zero

$$\tau_B - \tau_A + \frac{(\xi - \xi_0)c^2}{\sqrt{\alpha(\xi - \xi_0)^2 c^2 + \alpha d_0^2}} = 0 \tag{3.7}$$

This is a quadratic equation for ξ and the solution is

$$\xi = \xi_0 \pm \frac{d_0(\tau_A - \tau_B)}{c\sqrt{c^2/\alpha - (\tau_A - \tau_B)^2}} \tag{3.8}$$

Substituting Eq.3.5 and Eq.3.8 into Eq.3.6 and selecting the appropriate branch of the square root, we obtain the solution

$$\tau_C = d_0 \sqrt{\frac{1}{\alpha} - \frac{(\tau_A - \tau_B)^2}{c^2}} + \frac{a}{c}\tau_A \cos\theta_B + \frac{b}{c}\tau_B \cos\theta_A \tag{3.9}$$

It is worth to mention that the minimization constraint $0 \le \xi \le 1$ makes sure the causality relationship is satisfied, i.e. the characteristic direction estimated lies inside the triangle and thus the acceptance of solution values always in acceding order (Eq.3.10).

$$\tau_C \ge \max\left\{\tau_A, \tau_B\right\} \tag{3.10}$$

3D Local Solver

For the 3D tetrahedron, as shown in Figure 3.11, we assume the DToF values for nodes *A*, *B* and *C* are known and to solve for node *D*. Let ξ, ζ, η be the normalized distance from *B* to *A*, *C* to *B*, and *A* to *C*, respectively. The DToF at any point $\tilde{D}(\xi, \zeta, \eta)$ can be approximated by the linear interpolation, shown by Eq.3.11:

$$\tau_{\tilde{D}} = \xi \tau_A + \zeta \tau_B + \eta \tau_C \tag{3.11}$$

where ξ, ζ, η satisfy the following requirements:

$$0 \le \xi, \zeta, \eta \le 1 \text{ and } \xi + \zeta + \eta = 1 \tag{3.12}$$

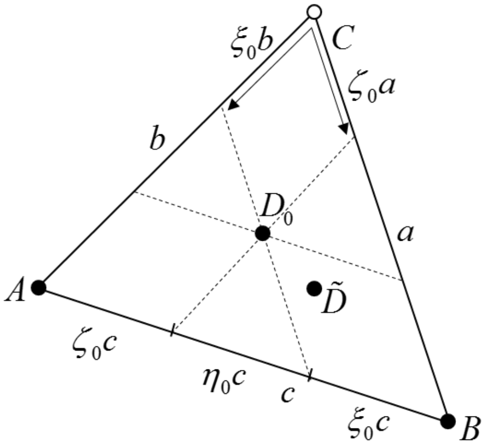

Figure 3.11 Travel-time updating procedure via Fermat's principle in 3D

According to Fermat's principle, the actual travel time to *D* corresponds to the minimum of the travel time with respect to path perturbations:

$$\tau_D = \min_{\xi,\zeta,\eta} \left\{ \tau_{\tilde{D}} + \sqrt{\frac{\left\| D_0\left(\xi_0, \zeta_0, \eta_0\right) \tilde{D}\left(\xi, \zeta, \eta\right) \right\|^2 + d_0^2}{\alpha}} \right\} \tag{3.13}$$

where $D_0(\xi_0, \zeta_0, \eta_0)$ is the normal projection of node *D* onto face *ABC*, d_0 is the length from node *D* to point D_0, and α is the diffusivity. We define $\mathbf{a}$, $\mathbf{b}$ as the vectors from *C* to *B* and *C* to *A* respectively, also define $\tilde{\xi} = \xi - \xi_0$ and $\tilde{\zeta} = \zeta - \zeta_0$ such that the distance between *D* and $\tilde{D}$ can be expressed as:

$$\begin{aligned} d^2 &= \left\| D_0\left(\xi_0,\zeta_0,\eta_0\right)\tilde{D}\left(\xi,\zeta,\eta\right)\right\|^2 + d_0^2 \\ &= \left\|\tilde{\xi}\mathbf{b}+\tilde{\zeta}\mathbf{a}\right\|^2 + d_0^2 = \tilde{\xi}^2 b^2 + \tilde{\zeta}^2 a^2 + 2\tilde{\xi}\tilde{\zeta}h^2 + d_0^2 \end{aligned} \tag{3.14}$$

where we have defined

$$h^2 = \mathbf{b}^T\mathbf{a} = ab\cos\theta_C \tag{3.15}$$

and θ_C is the angle at node *C* between the two vectors $\mathbf{a}$ and $\mathbf{b}$. Now the Eq.3.13 can be written as

$$\tau_D = \min_{\xi,\zeta,\eta}\left\{\left(\tilde{\xi}+\xi_0\right)\tau_A + \left(\tilde{\zeta}+\zeta_0\right)\tau_B + \left(\eta_0-\tilde{\xi}-\tilde{\zeta}\right)\tau_C + \sqrt{\frac{\tilde{\xi}^2b^2+\tilde{\zeta}^2a^2+2\tilde{\xi}\tilde{\zeta}h^2+d_0^2}{\alpha}}\right\} \tag{3.16}$$

By invoking Fermat's principle, Eq.3.16 can be solved by setting the derivative of τ_D with respect to both $\tilde{\xi}$ and $\tilde{\zeta}$ to zero

$$\begin{aligned} \frac{d\tau_D}{d\tilde{\xi}} &= \frac{d}{d\tilde{\xi}}\left(\left(\tilde{\xi}+\xi_0\right)\tau_A + \left(\tilde{\zeta}+\zeta_0\right)\tau_B + \left(\eta_0-\tilde{\xi}-\tilde{\zeta}\right)\tau_C + \sqrt{\frac{d^2}{\alpha}}\right) \\ &= \tau_A - \tau_C + \frac{b^2\tilde{\xi}+\tilde{\zeta}h^2}{\sqrt{\alpha d^2}} = 0 \end{aligned} \tag{3.17}$$

and similarly

$$\frac{d\tau_D}{d\tilde{\zeta}} = \tau_B - \tau_C + \frac{\tilde{\zeta}a^2+\tilde{\xi}h^2}{\sqrt{\alpha d^2}} = 0 \tag{3.18}$$

By solving Eq.3.17 and Eq.3.18 for the two unknowns, we obtain

$$\tilde{\xi} = -\frac{\sqrt{\alpha d^2}\left(ua^2-vh^2\right)}{(2S)^2} \tag{3.19a}$$

$$\tilde{\zeta} = -\frac{\sqrt{\alpha d^2}\left(vb^2-uh^2\right)}{(2S)^2} \tag{3.19b}$$

where $u = \tau_A - \tau_C$, $v = \tau_B - \tau_C$ and S is defined as:

$$S = \frac{1}{2} bc \sin\theta_A = \frac{1}{2} ac \sin\theta_B = \frac{1}{2} ab \sin\theta_C \tag{3.20}$$

Substituting Eq.3.19 and Eq.3.20 into Eq.3.16, we can obtain

$$d = \frac{d_0}{\sqrt{\alpha}} \cdot \frac{1}{\sqrt{\frac{1}{\alpha} - \frac{w^2}{(2S)^2}}} \tag{3.21}$$

where w is defined by Eq.3.22, which can be further expressed in the symmetric formula as Eq.3.23.

$$w^2 = u^2a^2 + v^2b^2 - 2uvh^2 \tag{3.22}$$

$$w^2 = (\tau_A - \tau_B)(\tau_A - \tau_C)a^2 + (\tau_B - \tau_A)(\tau_B - \tau_C)b^2 + (\tau_C - \tau_A)(\tau_C - \tau_B)c^2 \tag{3.23}$$

Substituting Eq.3.19 and Eq.3.21 into Eq.3.16, we arrive at

$$\tau_D = d_0 \sqrt{\frac{1}{\alpha} - \frac{w^2}{(2S)^2}} + \xi_0\tau_A + \zeta_0\tau_B + \eta_0\tau_C \tag{3.24}$$

Similarly, the minimization constraints $0 \le \xi, \zeta, \eta \le 1$ and $\xi + \zeta + \eta = 1$ make sure the characteristic direction estimated lies inside the tetrahedral and thus the acceptance of solution values always in acceding order (Eq.3.25).

$$\tau_D \ge \max\{\tau_A, \tau_B, \tau_C\} \tag{3.25}$$

3.4.2 Eulerian Discretization

The concept of the Eulerian construction is to approximate the gradient of the ray by finite difference discretization and then solve the characteristic vector as unknown. Here we follow Sethian and Vladimirsky (2000) and Qian et al. (2007).

2D Local Solver

Similarly, as shown in Figure 3.12, suppose we already know the DToF value for nodes *A* and *B* and now solve for the DToF for node *C*. Let *a* be the length of *BC* and *b* be the length of *AC*. Let $\vec{\sigma}_{AC}$ be the unit vector pointing from *A* to *C* and $\vec{\sigma}_{BC}$ be the unit vector pointing from *B* to *C* Then,

$$\begin{aligned} \vec{\sigma}_{AC} &= \frac{1}{b}(x_C - x_A, y_C - y_A) \\ \vec{\sigma}_{BC} &= \frac{1}{a}(x_C - x_B, y_C - y_B) \end{aligned} \tag{3.26}$$

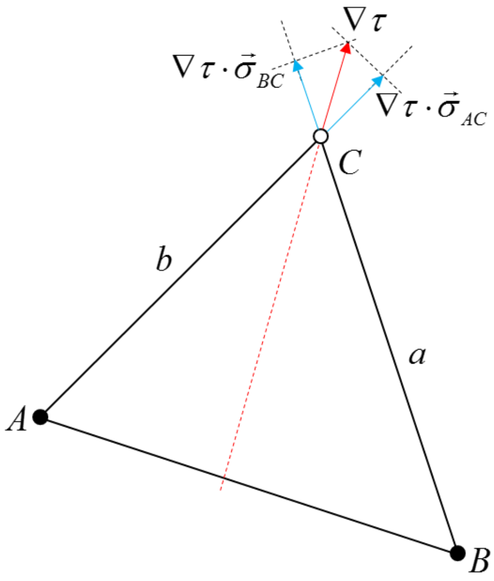

Figure 3.12 Travel-time updating procedure via Eulerian discretization in 2D

Assuming a linear approximation to τ locally, we have the following finite difference equation:

$$\begin{aligned} \frac{1}{b}(\tau_C - \tau_A) &= \nabla\tau\cdot\vec{\sigma}_{AC} \\ \frac{1}{a}(\tau_C - \tau_B) &= \nabla\tau\cdot\vec{\sigma}_{BC} \end{aligned} \tag{3.27}$$

If we define the matrix $\mathbf{P}$ with rows $\vec{\sigma}_{AC}$ and $\vec{\sigma}_{BC}$, then the characteristic direction $\nabla\tau$ can be calculated using Eq.3.28.

$$\nabla\tau = \mathbf{P}^{-1}\left(\begin{pmatrix}1/b\\1/a\end{pmatrix}\tau_C - \begin{pmatrix}\tau_A/b\\\tau_B/a\end{pmatrix}\right) \tag{3.28}$$

Substituting the above $\nabla\tau$ into the Eikonal equation, we obtain a quadratic equation with τ_C as the unknown parameter. The solution for τ_C should be verified against the causality condition, i.e., the computed characteristic direction must lie inside the triangle. In the implementation, the value obtained for point *C* will be updated only if the causality condition is satisfied. If the causality condition cannot be satisfied, the solution is updated from the triangle edges by solving a 1D Eikonal equation.

3D Local Solver

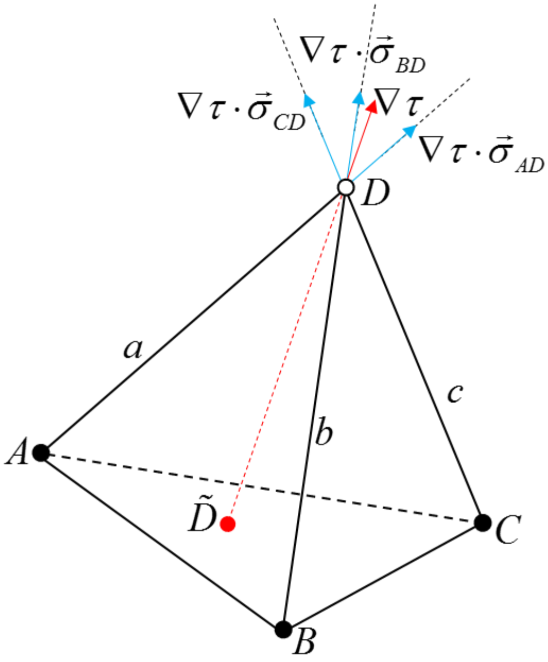

Figure 3.13 Travel-time updating procedure via Eulerian discretization in 3D

Similar to Eulerian discretization 2D, suppose we already know the DToF value for nodes *A*, *B* and *C* and now solve for the DToF for node *D* (shown in Figure 3.13). Let *a*, *b* and *c* be the length of *DA*, *DB*, and *DC*, respectively. Let $\vec{\sigma}_{AD}$, $\vec{\sigma}_{BD}$, and $\vec{\sigma}_{CD}$ be the unit vector pointing from *A* to *D*, *B* to *D* and *C* to *D*, respectively. Then,

$$\begin{aligned}
\vec{\sigma}_{AD} &= \frac{1}{a}(x_D - x_A, y_D - y_A, z_D - z_A) \\
\vec{\sigma}_{BD} &= \frac{1}{b}(x_D - x_B, y_D - y_B, z_D - z_B) \\
\vec{\sigma}_{CD} &= \frac{1}{c}(x_D - x_C, y_D - y_C, z_D - z_C)
\end{aligned} \tag{3.29}$$

Assuming a linear approximation to τ locally, we have the following finite difference equation:

$$\begin{aligned}
\frac{1}{a}(\tau_D - \tau_A) &= \nabla\tau \cdot \vec{\sigma}_{AD} \\
\frac{1}{b}(\tau_D - \tau_B) &= \nabla\tau \cdot \vec{\sigma}_{BD} \\
\frac{1}{c}(\tau_D - \tau_C) &= \nabla\tau \cdot \vec{\sigma}_{CD}
\end{aligned} \tag{3.30}$$

If we define the matrix $\mathbf{P}$ with rows $\vec{\sigma}_{AD}$, $\vec{\sigma}_{BD}$, and $\vec{\sigma}_{CD}$, then the gradient $\nabla\tau$ can be calculated using Eq.3.31.

$$\nabla\tau = \mathbf{P}^{-1}\left(\begin{pmatrix} 1/a \\ 1/b \\ 1/c \end{pmatrix}\tau_D - \begin{pmatrix} \tau_A/a \\ \tau_B/b \\ \tau_C/c \end{pmatrix}\right) \tag{3.31}$$

Substituting the above $\nabla\tau$ into the Eikonal equation, we obtain a quadratic equation with τ_D as the unknown parameter. The solution for τ_D should be verified against the causality condition. If the causality condition cannot be satisfied, the solution is updated from the tetrahedron faces by solving 2D Eikonal equation in 3D space. Suppose we are solving the DToF value within tetrahedron face *ABD*, with the value at node *A* and *B* as known. Eq.3.30 cannot be directly applied since gradient approximation from $\vec{\sigma}_{CD}$ are not available. But the causality relationship requires the characteristics lays within the *ABD* plane, which can be mathematically expressed as $(\vec{\sigma}_{AD}\times\vec{\sigma}_{BD})\cdot\nabla\tau=0$ for isotropic media. Then Eq.3.30 can be replaced by Eq.3.32:

$$\begin{aligned}
&\frac{1}{a}(\tau_D-\tau_A)=\nabla\tau\cdot\vec{\sigma}_{AD}\\
&\frac{1}{b}(\tau_D-\tau_B)=\nabla\tau\cdot\vec{\sigma}_{BD}\\
&0=(\vec{\sigma}_{AD}\times\vec{\sigma}_{BD})\cdot\nabla\tau
\end{aligned}\tag{3.32}$$

The matrix $\mathbf{P}$ are now with rows $\vec{\sigma}_{AD}$, $\vec{\sigma}_{BD}$, and $\vec{\sigma}_{AD}\times\vec{\sigma}_{BD}$. The gradient $\nabla\tau$ then can be calculated using Eq.3.33 and be substituted into Eikonal equation.

$$\nabla\tau=\mathbf{P}^{-1}\left(\begin{pmatrix}1/a\\1/b\\0\end{pmatrix}\tau_D-\begin{pmatrix}\tau_A/a\\\tau_B/b\\0\end{pmatrix}\right)\tag{3.33}$$

3.4.3 Comments on Implementation and Performance Comparison

Since the local Eikonal equation solver based on Fermat's principle provides the analytical solution, Eq.3.9 and Eq.3.24 can be directly implemented. To ensure the causality requirement, i.e. the characteristic line comes within the triangle or tetrahedron, the requirements of $0\le\xi\le1$ (in 2D) and $0\le\xi,\zeta,\eta\le1$ (in 3D) need be satisfied, which can be calculated from Eq.3.8 and Eq.3.19, respectively. Based on the perpendicular property, the parameters for the normal projection point ξ_0 (in 2D) and ξ_0, ζ_0 (in 3D) can be calculated as Eq.3.34a (in 2D) and Eq.3.34b (in 3D),

$$\overrightarrow{CS_0} \cdot \overrightarrow{AB} = (\xi_0 \overrightarrow{AB} - \overrightarrow{AC}) \cdot \overrightarrow{AB} = 0 \tag{3.34a}$$

$$\begin{cases} \overrightarrow{DD_0} \cdot \overrightarrow{CA} = (\xi_0 \overrightarrow{CA} + \zeta_0 \overrightarrow{CB} - \overrightarrow{CD}) \cdot \overrightarrow{CA} = 0 \\ \overrightarrow{DD_0} \cdot \overrightarrow{CB} = (\xi_0 \overrightarrow{CA} + \zeta_0 \overrightarrow{CB} - \overrightarrow{CD}) \cdot \overrightarrow{CB} = 0 \end{cases} \tag{3.34b}$$

For Eikonal equation based on Eulerian discretization, the characteristic direction is approximated using Eq.3.28 (in 2D) or Eq.3.31 (in 3D) with the calculated DToF value. The vector, connecting the target node and intersection point on *AB* edge or *ABC* plane, should be parallel to the characteristic direction. This parallel relationship can be represented by forcing the outer product equals zero (Eq.3.35a in 2D and Eq.3.35b in 3D). After solving the Eq.3.35, the condition $0 \le \xi \le 1$ (in 2D) or $0 \le \xi, \zeta, 1 - \xi - \zeta \le 1$ (in 3D) will ensure the causality requirement.

$$\overrightarrow{CS} \times \nabla \tau = (\xi \overrightarrow{AB} - \overrightarrow{AC}) \times \nabla \tau = 0 \tag{3.35a}$$

$$\overrightarrow{D\tilde{D}} \times \nabla \tau = (\xi \overrightarrow{CA} + \zeta \overrightarrow{CB} - \overrightarrow{CD}) \times \nabla \tau = 0 \tag{3.35b}$$

Another approach to check the causality condition is to decompose the $\nabla \tau$ to the unit vector direction (Eq.3.36a in 2D and Eq.3.36b in 3D). ξ, ζ and η are parameters to be determined through Eq.3.36. The causality condition is verified only if the condition $\xi, \zeta, \eta \ge 0$ is satisfied.

$$\nabla \tau = \xi \cdot \vec{\sigma}_{AC} + \zeta \cdot \vec{\sigma}_{BC} \tag{3.36a}$$

$$\nabla \tau = \xi \cdot \vec{\sigma}_{AD} + \zeta \cdot \vec{\sigma}_{BD} + \eta \cdot \vec{\sigma}_{CD} \tag{3.36b}$$

With the implementation of causality check, the above two constructions provide identical results. We demonstrate the comparison between these two constructions by application to a regular tetrahedron for which each face is an equilateral triangle (Lelièvre et al. 2011). The coordinates of this tetrahedron are given in Table 3.1, with the centroid at the origin. This tetrahedron is sketched in Figure 3.14. Here we investigate the error associated with the planar wave-front assumption during the local update based on Fermat's principle and Eulerian discretization.

A source is placed at some distance away from the tetrahedron on the negative side of the *z*-axis and set the homogeneous diffusivity to 1 $ft{\cdot}hr^{-1/2}$. The travel time for node *A*, *B*, *C* are assigned with the exact value. The travel time for node *D* is calculated and compared to the exact solution. The distance of source to origin varies between 1 *ft* and 10 *ft*, and the results are presented in Figure 3.15a, where the absolute error decreases as the source point moves far away. Then, we allow the location of the source to move away from the *z*-axis while maintaining the distance to the origin at 10 *ft*, and the results are shown by Figure 3.15b, with the largest errors occurring when the polar angle is close to 180°. The point here is that, from Figure 3.15, we observe the Eikonal equation solver based on Fermat's principle and Eulerian discretization provide the same solution.

Table 3.1 Coordinates that define a regular tetrahedron with centroid at the origin

Node	*x*	*y*	*z*
A	0.9428	0.0000	-0.3333
B	-0.4714	0.8165	-0.3333
C	-0.4714	-0.8165	-0.3333
D	0.0000	0.0000	1.0000

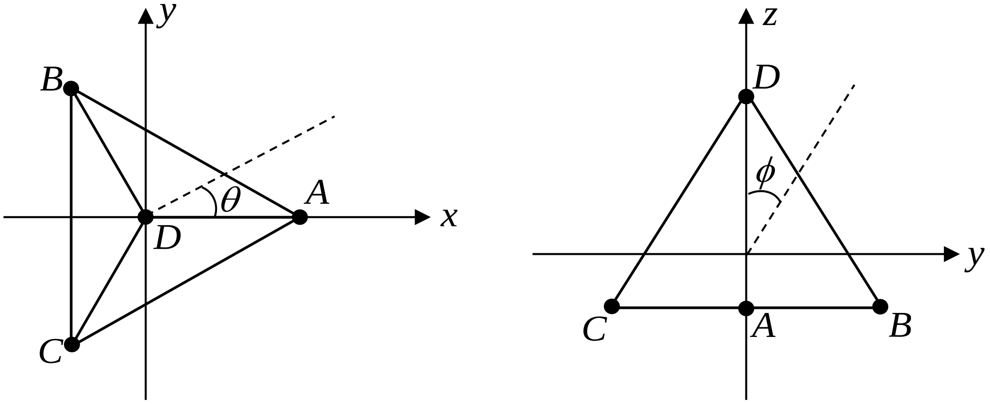

Figure 3.14 Tetrahedron defined in Table 3.1 as viewed from a) +*z* direction b) +*x* direction, with azimuthal angle θ and polar angle ϕ (after Lelièvre et al. (2011))

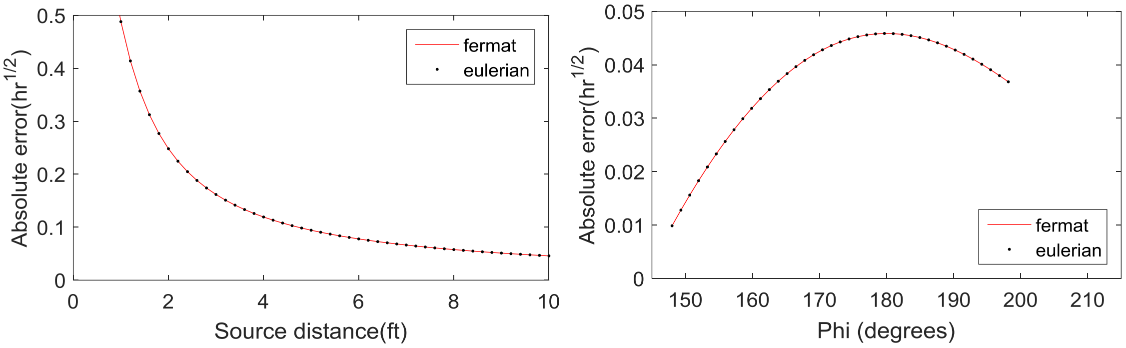

Figure 3.15 Absolute error versus source distance and polar angle for the FMM local update based on Fermat's principle and Eulerian discretization, showing two constructions provide identical results

The second error analysis model is a 50×50×50 *ft* homogeneous cubic. This cubic is discretized into tetrahedrons using the force-equilibrium based optimization, with 15469 nodes and 83712 cells. The homogeneous diffusivity is set to 1 $ft\cdot hr^{-1/2}$. The source is placed at one corner, and nodes within a distance of 1 *ft* to the source point are initialized with the analytical solution. The calculated DToF based on Eulerian discretization is shown in Figure 3.16a, which provides a nice 1/8 sphere. The average relative error of calculated to the analytical solution is 1.74%. Figure 3.16b shows the Q-Q plot of the calculated DToF value between FMM local solvers based on Fermat's principle and Eulerian discretization. All the results perfectly lay on the 45° line, which demonstrates that these two constructions provide identical results. The absolute errors between these two constructions for this case are all less than 5.0E-12 $hr^{1/2}$.

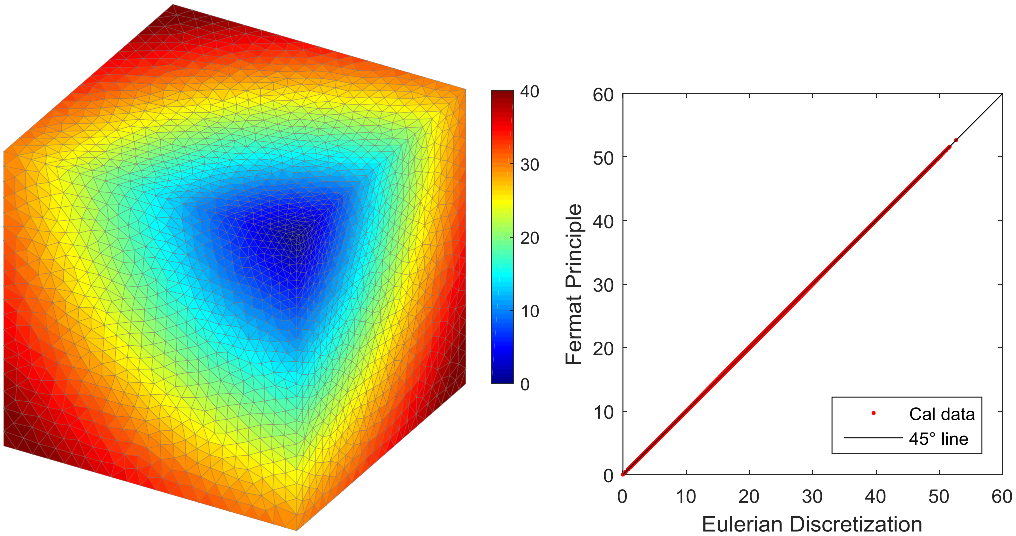

Figure 3.16 a) DToF for homogeneous cubic; b) Q-Q plot of results based on Fermat's principle and Eulerian Discretization

3.4.4 Extension to Anisotropic Permeability Field

The properties of the subsurface porous medium are seldom purely isotropic, at least in vertical and horizontal direction; therefore the development of Eikonal equation solver for anisotropic properties is crucial. From the previous comparison for isotropic media, we observe that the local Eikonal equation solver based on Fermat's principle and the one based on Eulerian discretization provide identical results. However, the local Eikonal equation solver based on Eulerian discretization is more straightforwardly and easily to be extended to 3D from 2D.

In Fermat's principle construction for anisotropic media, the diffusivity term α in Eq.3.6 and Eq.3.16 becomes a function of location and direction, instead of a constant value. We cannot obtain as concise derivative results as Eq.3.7, Eq.3.17 and Eq.3.18. On the other hand, the Eulerian discretization is more ready to be extended to anisotropic permeability, as it only approximates the DToF gradient $\nabla\tau$ and it doesn't touch the permeability tensor at all. The approximated DToF gradient can be directly substituted into the Eikonal equation for anisotropic permeability, expressed as Eq.3.37 (Datta-Gupta and King 2007), where the permeability tensor $\overline{\overline{\mathbf{k}}}$ is a positive-definite symmetric matrix.

$$\left(\nabla\tau(\vec{x})\right)^T \cdot \overline{\overline{\mathbf{k}}} \cdot \nabla\tau(\vec{x}) = \phi(\vec{x})\mu c_t \tag{3.37}$$

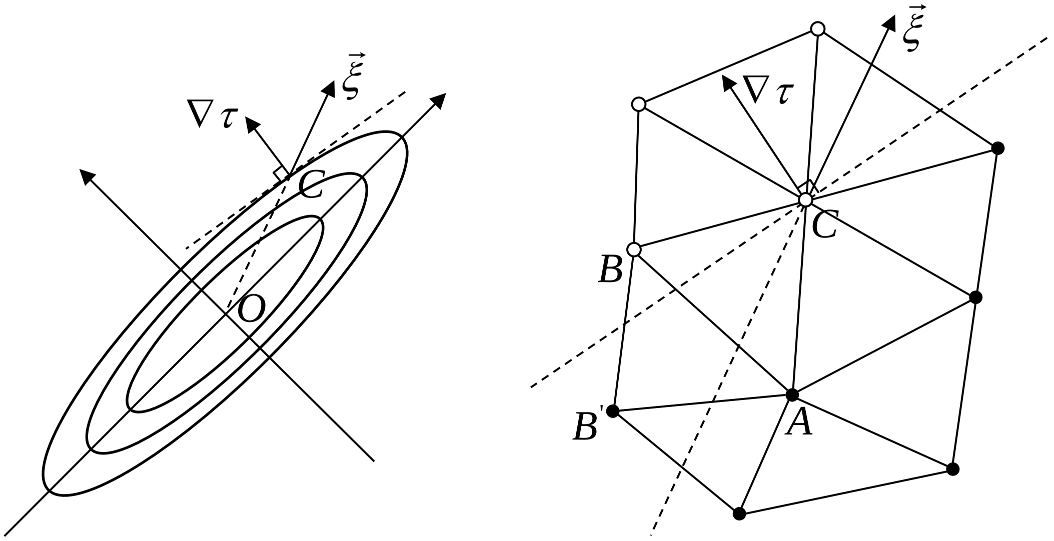

Figure 3.17 a) Contours of arrival time in homogenous anisotropic case showing the difference between characteristic direction and the gradient; b) Possible triangular mesh near point *C* showing the necessity of extending FMM for anisotropic case

Then we follow the same procedure as discussed in section 3.4.2 for the DToF calculation. The only difference is the causality requirement check. For the isotropic medium, the characteristic direction coincides with the gradient direction, which is critical to derive the causality relationship in ordinary fast marching methods. The extension of fast marching methods to solve anisotropic Eikonal equations is not trivial because the characteristic direction will be in general different from the gradient direction. For example, Figure 3.17a shows the travel time contours of the wave propagating from the source *O* in the homogeneous anisotropic medium. The characteristic direction and the gradient direction are shown in the figure at point *C*. Figure 3.17b shows one possible situation of local triangular mesh near the point *C*, where the upwind scheme does not guarantee causality relationship even for acute triangle *ABC*.

For anisotropic media, with the DToF gradient as $\nabla\tau = ((\nabla\tau)_1, (\nabla\tau)_2, (\nabla\tau)_3)^T$, the characteristic direction can be expressed as the derivative of Eikonal equation with respective to the DToF gradient, which results in the dot product of the permeability tensor and DToF gradient (expressed as Eq.3.38a). It can be expanded as Eq.3.38b.

$$\frac{\partial}{\partial(\nabla\tau)}\left((\nabla\tau)^T \cdot \overline{\overline{\mathbf{k}}} \cdot \nabla\tau\right) = \overline{\overline{\mathbf{k}}} \cdot \nabla\tau \tag{3.38a}$$

$$\begin{pmatrix} k_{11}(\nabla\tau)_1 + k_{12}(\nabla\tau)_2 + k_{13}(\nabla\tau)_3 \\ k_{21}(\nabla\tau)_1 + k_{22}(\nabla\tau)_2 + k_{23}(\nabla\tau)_3 \\ k_{31}(\nabla\tau)_1 + k_{32}(\nabla\tau)_2 + k_{33}(\nabla\tau)_3 \end{pmatrix} \tag{3.38b}$$

For specific scenarios, such as 2D general problem (Eq.3.39a) or 3D problem but the principle direction of the permeability tensor aligns with the coordinates (Eq.3.39b), the characteristics can be calculated using Eq.3.40a and Eq.3.40b.

$$\overline{\overline{\mathbf{k}}} = \begin{bmatrix} k_{11} & k_{12} \\ k_{21} & k_{22} \end{bmatrix},\ k_{11}, k_{22} > 0,\ k_{12} = k_{21} \tag{3.39a}$$

$$\overline{\overline{\mathbf{k}}} = \begin{bmatrix} k_{11} & 0 & 0 \\ 0 & k_{22} & 0 \\ 0 & 0 & k_{33} \end{bmatrix},\ k_{11}, k_{22}, k_{33} > 0 \tag{3.39b}$$

$$\begin{bmatrix} k_{11}(\nabla\tau)_1 + k_{12}(\nabla\tau)_2 \\ k_{22}(\nabla\tau)_2 + k_{21}(\nabla\tau)_1 \end{bmatrix} \tag{3.40a}$$

$$\begin{bmatrix} k_{11}(\nabla\tau)_1 \\ k_{22}(\nabla\tau)_2 \\ k_{33}(\nabla\tau)_3 \end{bmatrix} \tag{3.40b}$$

In the anisotropic scenario, the third equation of Eq.3.32 should be Eq.3.41, because it is essentially the characteristic direction that should be constrained to the plane and the characteristic direction is no longer align with the DToF gradient.

$$0 = (\vec{\sigma}_{AD} \times \vec{\sigma}_{BD}) \cdot \overline{\overline{\mathbf{k}}} \cdot \nabla\tau \tag{3.41}$$

For the same reason, the causality condition check, which is previously expressed as Eq.3.35 and Eq.3.36 for isotropic media should be as Eq.3.42 and Eq.3.43, respectively. When the causality requirement is further violated or only one data point is known for the tetrahedron, the problem reduces to a 1D Eikonal calculation. In which case, the maganitude of permeability along that edge should be calculated, which is given in Appendix B. The 1D Eikonal equation automatically satisfys causality requirement.

$$\overrightarrow{CS} \times (\overline{\overline{\mathbf{k}}} \cdot \nabla\tau) = (\xi \overrightarrow{AB} - \overrightarrow{AC}) \times (\overline{\overline{\mathbf{k}}} \cdot \nabla\tau) = 0 \tag{3.42a}$$

$$\overrightarrow{D\tilde{D}} \times (\overline{\overline{\mathbf{k}}} \cdot \nabla\tau) = (\xi \overrightarrow{CA} + \zeta \overrightarrow{CB} - \overrightarrow{CD}) \times (\overline{\overline{\mathbf{k}}} \cdot \nabla\tau) = 0 \tag{3.42b}$$

$$\overline{\overline{\mathbf{k}}} \cdot \nabla\tau = \xi \cdot \vec{\sigma}_{AC} + \zeta \cdot \vec{\sigma}_{BC} \tag{3.43a}$$

$$\overline{\overline{\mathbf{k}}} \cdot \nabla\tau = \xi \cdot \vec{\sigma}_{AD} + \zeta \cdot \vec{\sigma}_{BD} + \eta \cdot \vec{\sigma}_{CD} \tag{3.43b}$$

Zhang et al. (2013) showed that the causality relationship in structured grids could be easily satisfied if the principal direction of anisotropy is aligned with the grid. However, it is impossible to align all the unstructured grid in the same direction with the principal direction of anisotropy, which makes the causality requirement a more severe issue compared to the structured grid. Therefore, the causality requirement is more likely be violated in the unstructured grid system.

There are two approaches to deal with causality violation. One approach, known as the expanded neighborhood method, was proposed by Sethian and Vladimirsky (2000). The basic idea of the expanded neighborhood method is to find a “virtual triangle” that contains the characteristic direction and can “support” the calculation of DToF at the target point. In the example shown by Figure 3.17b, the “virtual triangle” $AB'C$ may be used to correctly update DToF at point C. It is critical to realize that not only the immediate neighboring nodes but also nodes farther away may need to be considered for local updates. This process can relatively easily be implemented for the structured grid system, but it is quite challenging for unstructured grid system since it becomes difficult to find the candidate nodes to form “virtual triangle”. Another way to deal with the anisotropic case is the Recursive Fast Marching Algorithm.

3.4.5 Recursive Fast Marching Method

The Recursive Fast Marching Algorithm (Konukoglu et al. 2007) uses the immediate neighboring nodes to compute arrival times, but it includes a recursive correction scheme taking into account the fact that due to anisotropy the immediate neighborhood used for computation may not always capture the characteristic direction.

The key element in the algorithm is that whenever a new node *n* is accepted, all its immediate neighboring nodes need to be re-computed using the newly accepted value at *n* including those that are already accepted. Thus it is possible that some of the already accepted nodes will get even smaller values because of the newly accepted value at *n*. If that happens, those accepted nodes will be updated and added to a list called *changed*. Then we try to work on the *changed* nodes and empty them in a recursive process before the front is marching forward again. The framework of recursive fast marching method comprises of the following steps:

(1) Label all grid nodes as *unknown*;

(2) Assign τ values (usually zero) to the nodes corresponding to the initial position of the propagating front and label them as *accepted*;

(3) For each node that is *accepted*, locate its immediate neighboring nodes that are *unknown* and label them as *considered*;

(4) For each node labeled *considered*, update its τ value based on its accepted neighbors using the minimum of local solutions;

(5) If the *changed* list is not empty, pick the node with minimum τ value and remove it from the *changed* list. Otherwise, we pick the node which has the minimum τ value among *considered* list, and label it as *accepted*;

(6) For all the *accepted* neighbors of current picked node, update its τ value. If a better solution is found, this *accepted* neighbor is added into the *changed* list.

(7) For all *unknown* neighbors of current picked node, label them as *considered*.

(8) For all *considered* neighbors of current picked node, update its update its τ value based on its accepted neighbors using the minimum of local solutions;

(9) Go to step (5) until the *changed* list is empty and all *considered* nodes are *accepted*.

As a test of the recursive fast marching algorithm, we compare the solutions of the same homogeneous anisotropic Eikonal equation in the same 5-stencil square grid (29 by 29) using both ordinary FMM and recursive FMM. The results in Figure 3.18 show that ordinary fast marching algorithm provides inaccurate results in the anisotropic case.

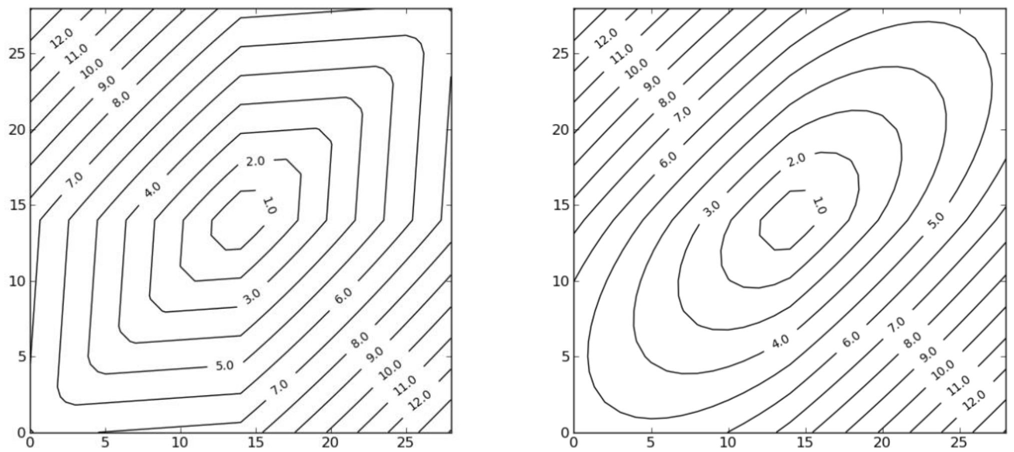

Figure 3.18 Solution of anisotropic Eikonal equation in 5-stencil square grid using a) isotropic fast marching algorithm; b) recursive fast marching algorithm

Figure 3.19 and Figure 3.20 show some numerical examples of calculated solution of the anisotropic Eikonal equation in 2D and 3D. The diffusivity anisotropy is 2:1 in the 2D case and Figure 3.19 shows accurate DToF calculation when the principle axis is rotated by an angle of 0^{o}, 30^{o}, -45^{o}. The diffusivity anisotropy with the 3D example is 3:2:1 and Figure 3.20 shows the DToF map precisely captures the anisotropy.

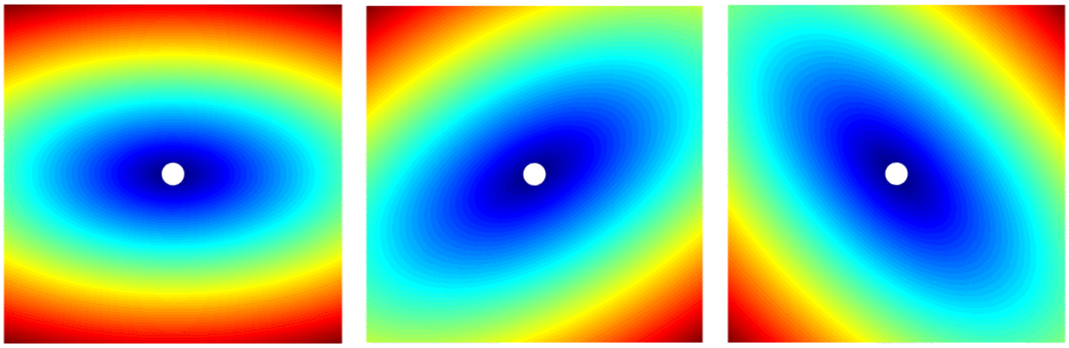

Figure 3.19 Solution of anisotropic Eikonal equation in 2D with diffusivity anisotropy 2:1 and rotation angle a) 0º; b) 30º; c) -45º

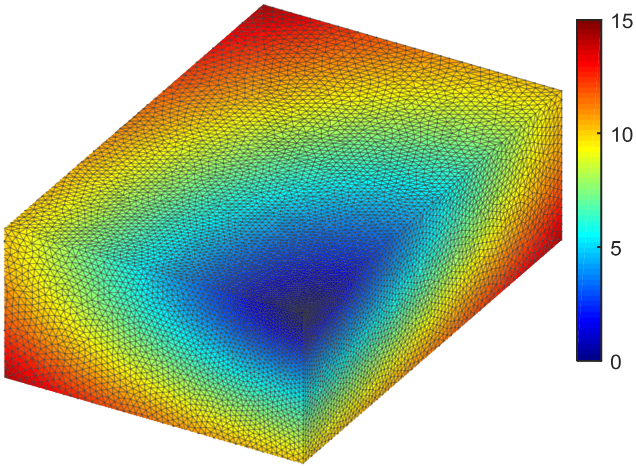

Figure 3.20 Solution of anisotropic Eikonal equation in 3D with diffusivity anisotropy 3:2:1

3.5 Solving Fluid Flow Equation

Without additional complexity and loss of generality, we just demonstrate the single phase fluid flow problem with the unstructured grid system. Starting with the mass conservation equation for single phase fluid flow, shown by Eq.3.44

$$\frac{\partial(\rho\phi)}{\partial t} = -\nabla\cdot(\rho\vec{u}) \tag{3.44}$$

$$\vec{u} = -\frac{k}{\mu}\nabla p \tag{3.45}$$

where ϕ is porosity, ρ is fluid density, and $\vec{u}$ is the Darcy velocity. k, μ and p are permeability, fluid viscosity and pressure, respectively.

Our proposed simulation approach relies on transforming the above equations into the 1D τ-coordinate. The mathematical details of the derivation are given in Appendix A. The transformed equation can be written as (with the sink/source term) Eq.3.46:

$$\frac{\partial(\phi\rho)}{\partial t} = \frac{\phi_{init}}{w(\tau)} \frac{\partial}{\partial\tau}\left(w(\tau)\rho \frac{(\mu c_t)_{init}}{\mu} \frac{\partial p}{\partial\tau} \right) + \rho q \tag{3.46}$$

$$w(\tau) = \frac{dV_p}{d\tau} \tag{3.47}$$

The $w(\tau)$ function is obtained from solving the Eikonal equation with the FMM, and then Eq.3.46 is solved numerically with a finite difference scheme. Since Eq.3.46 is solved only in a 1D spatial coordinate system, it is very computationally efficient. The heterogeneity and the physical properties appear to have "vanished" from the diffusivity equation in Eq.3.46, but actually, the heterogeneities have been lumped into the $w(\tau)$ function. Note that $w(\tau)$ is proportional to the surface area of the drainage volume and it is directly related to the geometry of the drainage volume of the well.

One approach to obtaining the $w(\tau)$ function is to calculate the drainage volume first, by adding up the pore volume within each τ-contour at different cut-off values, and then take the derivative with respect to τ. However, due to the grid effects and the reservoir heterogeneity, such a calculation for $w(\tau)$ is usually noisy and not smooth. In such a case, an appropriate smoothing technique should be carefully applied to extract accurate $w(\tau)$ response. Here, we propose a local discretization of $w(\tau)_i$ for each triangle, which works well without any additional requirements for smoothing. Eq.3.48 assumes a constant $w(\tau)_i$ value within each triangle between the corresponding min and max τ values and zero beyond this range. To compute $w(\tau)$ for the model at a particular τ value, we add local $w(\tau)_i$ from all triangles whose DToF range contains τ (shown by Eq.3.49).

$$w(\tau)_i = \frac{dV_p}{d\tau} = \frac{V_{p,i}}{\tau_{\max,i} - \tau_{\min,i}} \tag{3.48}$$

$$w(\tau) = \sum_{\tau_{\min,i} < \tau < \tau_{\max,i}} w(\tau)_i \tag{3.49}$$

3.6 Model Validation

3.6.1 Accuracy Comparison

To validate our proposed approach, we apply it to a shale oil reservoir model with a single infinite conductivity planar fracture, which can provide a simple cross-validation between our proposed approach and commercial finite difference based simulation. A finite volume based simulator has been implemented for the unstructured grid system and the performance is compared with commercial finite difference based simulation as well.

Figure 3.21a shows the tartan grid system for finite difference simulation and Figure 3.21b is the Voronoi grid (with 6343 cells) used for finite volume based simulation and our proposed approach. The key parameters are summarized in Table 3.2. This single fracture reservoir is produced at a constant BHP of 1000 *psi* for three years. Figure 3.22 compares the production rate from the three different techniques and from the comparison our proposed approach provides good agreement with the other two. Figure 3.22 also validates the correct implementation of the finite volume simulation.

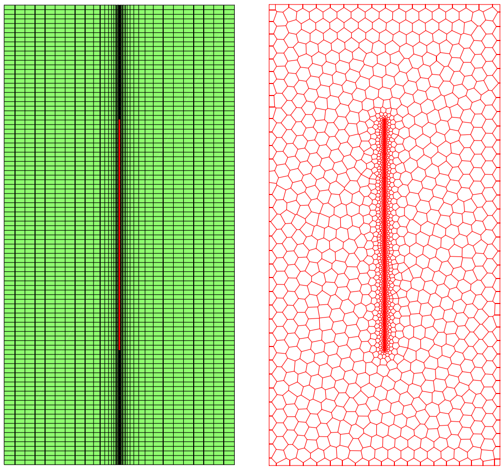

Figure 3.21 Single fracture: a) tartan grid b) Voronoi grid

Table 3.2 Parameters used in the 2D single fracture model

Reservoir size	500×1000×100 ft^3	Oil FVF (p_{init})	1.37 *bbl*/STB
Initial pressure	5470 *psi*	Wellbore radius	0.2 *ft*
Matrix porosity	0.046	Fracture porosity	0.25
Matrix permeability	0.0001 *md*	Fracture permeability	1000 *md*
Rock compressibility(p_{init})	1.0×10^{-6} psi^{-1}	Fracture width	0.2 *ft.*
Oil viscosity	0.2 *cp*	Fracture height	100 *ft*
Oil compressibility	2.0×10^{-5} psi^{-1}	Fracture half-length	250 *ft*

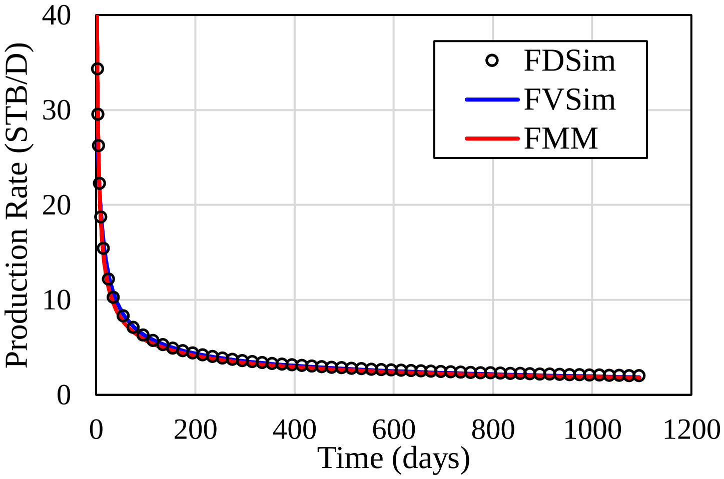

Figure 3.22 Production rate comparison for single fracture model

3.6.2 CPU Comparison

The goal of our proposed approach is to provide rapid reservoir simulation for complex fracture systems. As discussed in the previous section, the computational efficiency of our proposed approach with the FMM comes from the transformation of the 3D fluid flow equation into an equivalent 1D τ -based coordinate. Figure 3.23 shows the computational efficiency comparison between the finite volume based simulation and our proposed approach for different unstructured cases, including the above single fracture case (Figure 3.23b) and the application case in next section. Figure 3.23a shows the total CPU time for each scenario and Figure 3.23b presents the speedup ratio.

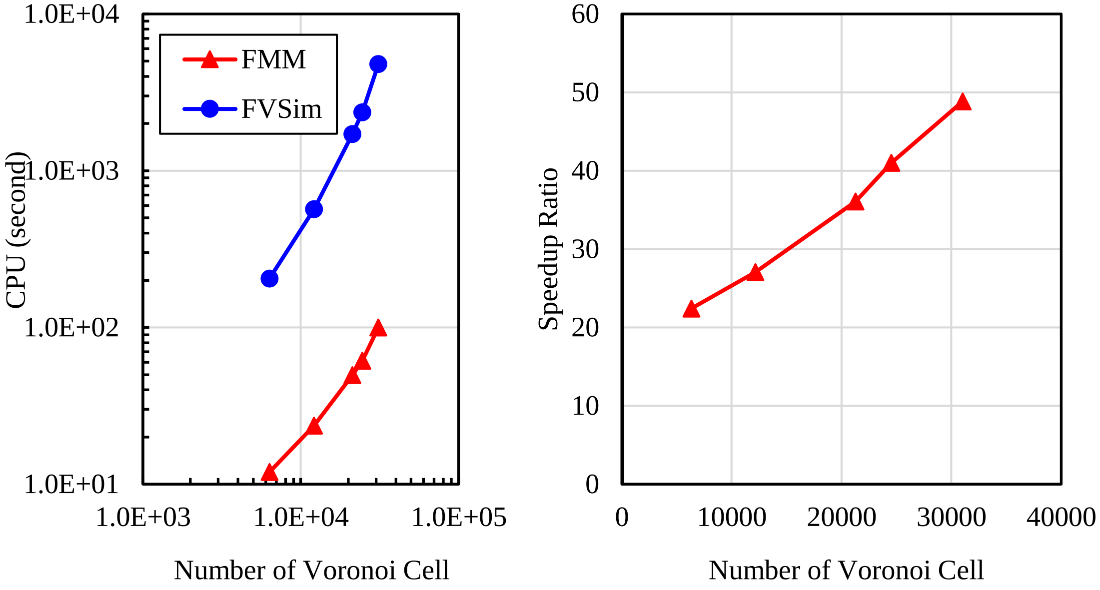

Figure 3.23 Computational efficiency comparison a) CPU time for FMM and finite volume method; b) Speedup ratio

According to the cases tested, our proposed approach provides orders of magnitude increase in computational speed with the computational advantage continuing to increase with the increase of the number of Voronoi cells. It is because that finite volume simulation (or finite difference simulation) has the computational complexity of $O(N^2)$ while the FMM calculation only has the computational complexity of $O(N \log N)$ and the fluid flow simulation in transformed 1D coordinate only takes a few seconds as it is independent of N, where N is the number of Voronoi cells.

3.7 Application

3.7.1 2D Synthetic Example

This section demonstrates the applicability of our proposed approach to a 2D synthetic naturally fractured reservoir with multiple hydraulic fractures. The natural fracture system (green and blue line segments in Figure 3.24) is generated according to statistical properties. Only the segments directly connected to the hydraulic fractures (blue line segments) are assumed to contribute to the flow. This model considers 10 hydraulic fractures with a spacing of 250 *ft*, and a half-length 250 *ft* or 300 *ft*. Other key parameters are listed in Table 3.3.

Table 3.3 Parameters used in the 2D multiple fracture model

Reservoir size	3500×1000×100 ft^3	HF permeability	1000 *md*
Initial pressure	5470 *psi*	HF porosity	0.25
Matrix porosity	0.046	HF width	0.2 *ft*
Matrix permeability	0.0001 *md*	HF height	100 *ft*
Rock compressibility(p_{init})	1.0×10^{-6} psi^{-1}	Number of HF	10
Oil viscosity	0.2 *cp*	HF half-length	250, 300 *ft*
Oil compressibility	2.0×10^{-5} psi^{-1}	Propped NF permeability	10 *md*
Oil FVF (p_{init})	1.37 *bbl*/STB	Propped NF width	0.2 *ft.*
Wellbore radius	0.2 *ft*	Propped NF porosity	0.1

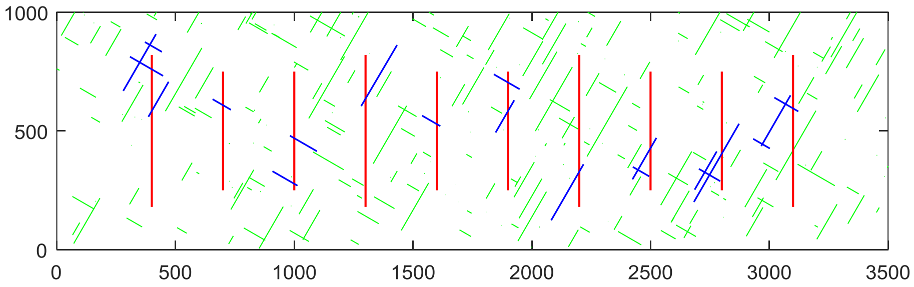

Figure 3.24 Multiple hydraulic fractures in a naturally fractured reservoir

Figure 3.25 shows the discretization for this complex fracture network, with 31038 Voronoi cells. We can see that all the fractures contributing to the flow are captured, and each Voronoi cell is well-shaped. Figure 3.26 is the diffusive time of flight map for this reservoir. The smaller value means it takes the shorter time for the pressure front to propagate to that location. The connected natural fractures help facilitate the pressure propagation into the matrix and therefore contribute to the flow.

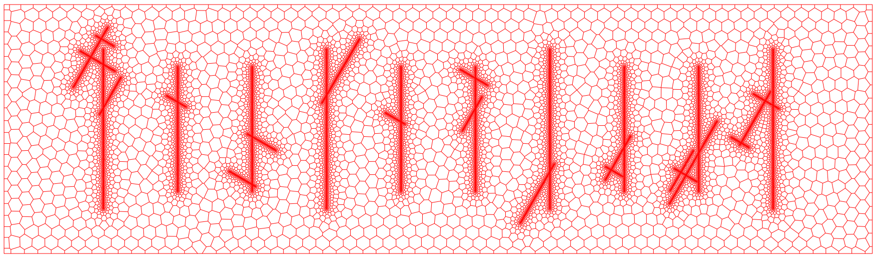

Figure 3.25 Voronoi grid for 2D multiple fracture model

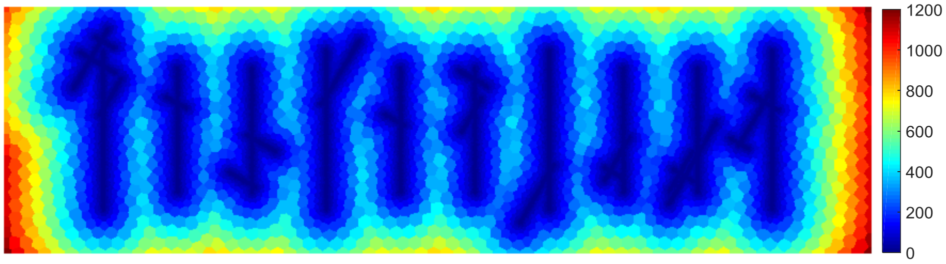

Figure 3.26 DToF map for 2D multiple fracture model calculated from the FMM

The synthetic multiple fracture model is simulated for three years under a constant bottom-hole pressure constraint of 1000 *psi*. After solving the 1D fluid flow equation in the τ-coordinate, the pressure value can be interpolated back to the physical cells based on their corresponding τ-value. Figure 3.27 shows the pressure distribution at different times. From pressure map at three years (Figure 3.27c), it can be detected that the fracture interference already occurs.

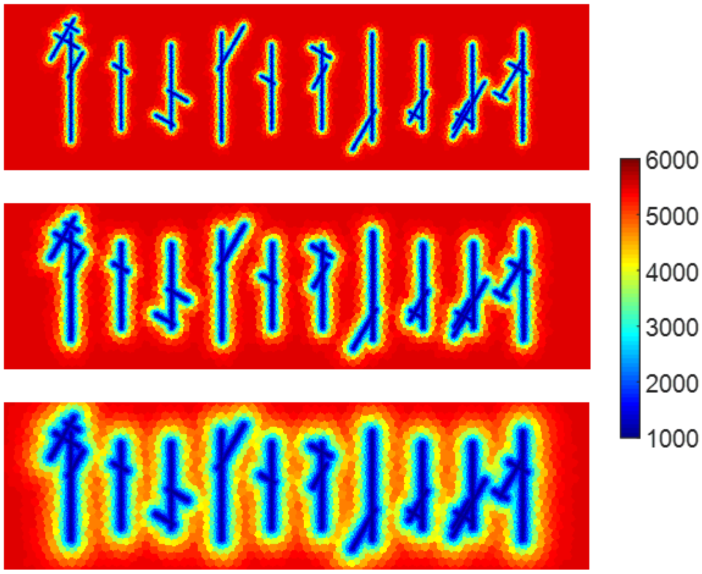

Figure 3.27 Pressure distribution for 2D multiple fracture model: a) 3 months; b) 1 year; c) 3 years

The oil production rate and cumulative production are presented in Figure 3.28 and Figure 3.29, respectively, where the results between cases with natural fractures and without natural fractures are compared. It can be observed that the production rate at very early times are quite similar due to the same hydraulic fracture areas for both cases, while the case with natural fractures maintains much higher production rate at the late time due to the contribution of the connected natural fractures. It takes only 70-100 seconds for solving the Eikonal equation using FMM and solving the 1D fluid flow simulation, as shown by the case with the largest number of Voronoi cell in Figure 3.23a. While the finite volume simulation takes 40 to 50 times longer (Figure 3.24b), which demonstrates the computational advantages of our proposed approach.

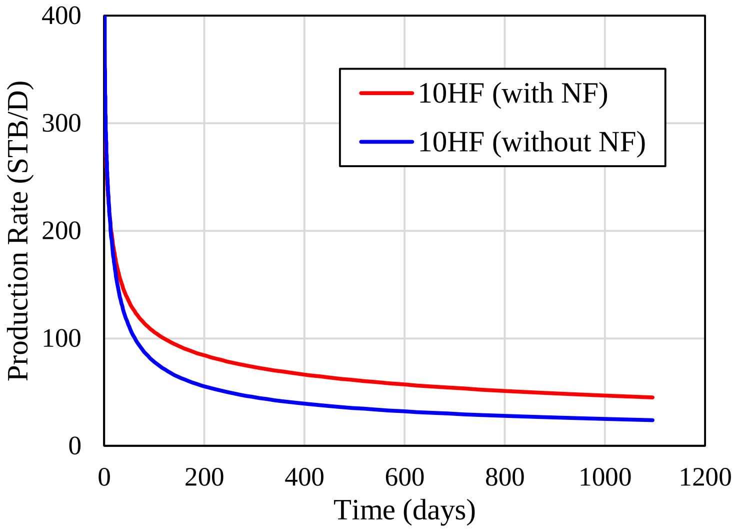

Figure 3.28 Production rate comparison for 2D multiple fracture model

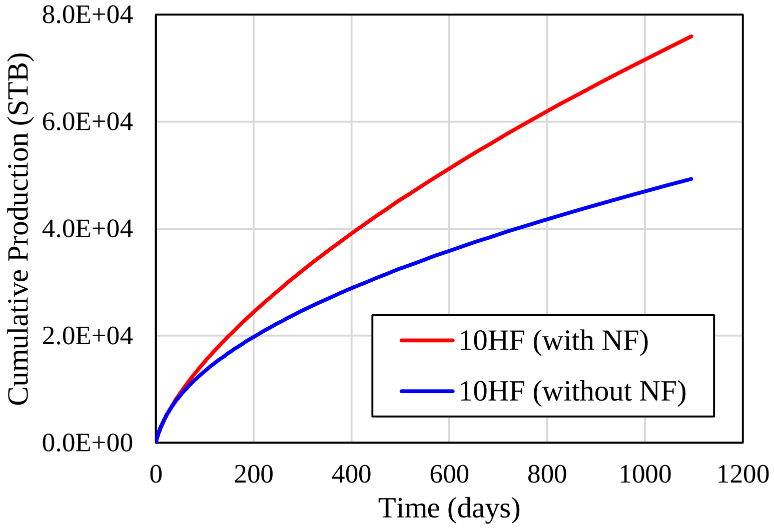

Figure 3.29 Cumulative production comparison for 2D multiple fracture model

3.7.2 3D Synthetic Example

The synthetic example is a gas reservoir, with reservoir size 1000×1000×100 ft^3. This synthetic reservoir is divided into five layers with non-uniform thickness. There are one dominating hydraulic fracture, with fracture permeability 1.0×10^5 *md,* and three intersecting fractures, with fracture permeability 1.0×10^3 *md*. All the fractures are fully penetrated, and they share the same fracture porosity and width. The synthetic example is simulated under bottom-hole pressure (1000 *psi*) constraint for 3 years. Other key parameters used in the synthetic example are listed in Table 3.4.

Table 3.4 Parameters used in the 3D synthetic model

Reservoir size	1000×1000×100 ft^3	Wellbore radius	0.16 *ft*
Grid thickness	20, 10, 30, 15, 25 *ft*	Fracture porosity	0.25
Initial pressure	5000 *psi*	Fracture width	0.2 *ft.*
Matrix porosity	0.046	Frac1 perm/length	1E5 *md*, 600*ft*
Matrix permeability	0.0001 *md*	Frac2 perm/length	1E3 *md*, 640 *ft*
Rock compressibility(p_{init})	4.0×10^{-6} psi^{-1}	Frac3 perm/length	1E3 *md*, 400 *ft*
Gas viscosity	0.0278 *cp*	Frac4 perm/length	1E3 *md*, 283 *ft*
Gas compressibility	1.45×10^{-4} psi^{-1}	BHP	1000 *psi*
Gas FVF (p_{init})	0.725 *bbl*/Mscf	Simulation time	3 years

Figure 3.30a shows the top-view of unstructured grids generated with the force-equilibrium algorithm. The unstructured grids are then further divided into the triangular prism and the DToF values at each node of the triangular prism are calculated with FMM. For each unstructured cell, the average value based on all nodes is assigned as the cell property, and Figure 3.30b represents the DToF map on the basis of each cell.

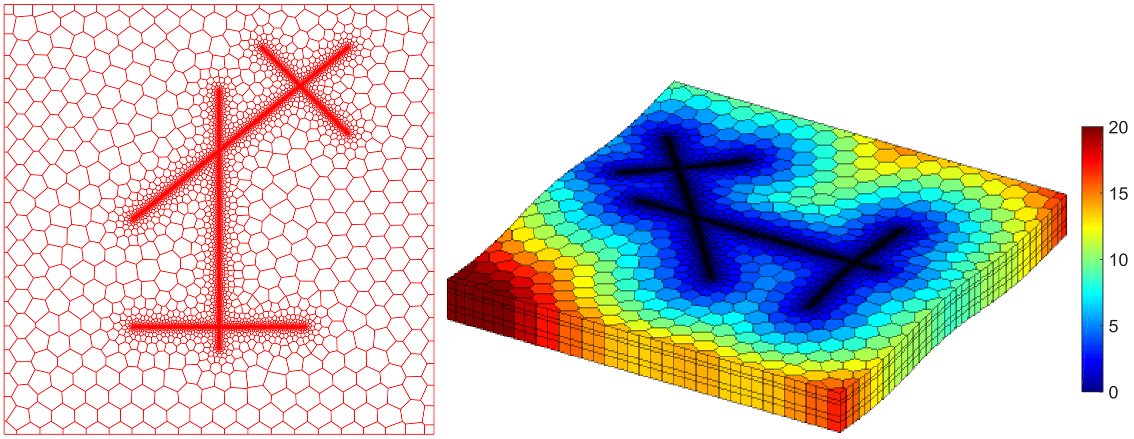

Figure 3.30 a) Top-view of unstructured Voronoi cells; b) DToF map in 2.5D unstructured grids

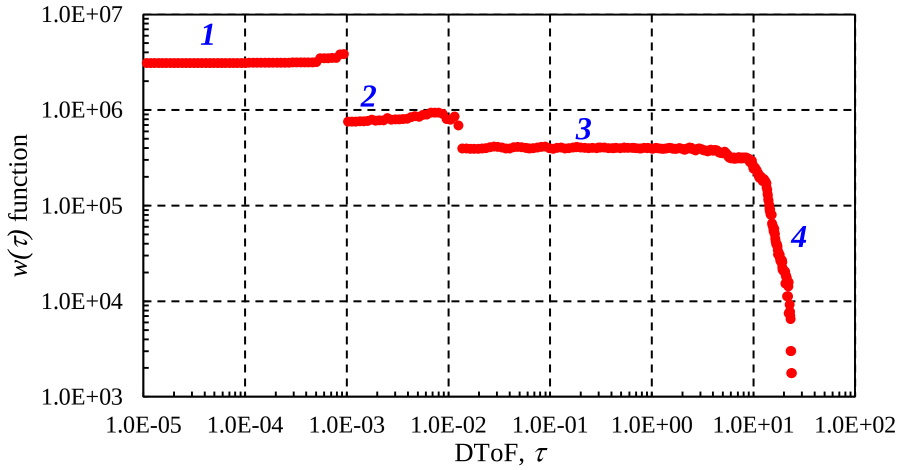

Figure 3.31 $w(\tau)$ **function indicating the flow geometry for 3D synthetic model**

With the proposed procedure to calculate the $w(\tau)$ function, we can skip the calculation of drainage volume. The $w(\tau)$ function for this synthetic example is presented in Figure 3.31. From Figure 3.31, four distinctive stages can be identified, where stage 1 corresponds to the pressure propagation in the dominating hydraulic fracture, stage 2 is the propagation into intersecting fractures (with smaller diffusivity), stage 3 represents the pressure propagation from fracture to formation and stage 4 is finite volume effect when pressure approaches the boundary. More analysis about the characteristic of $w(\tau)$ function can be found in Xue et al. (2016).

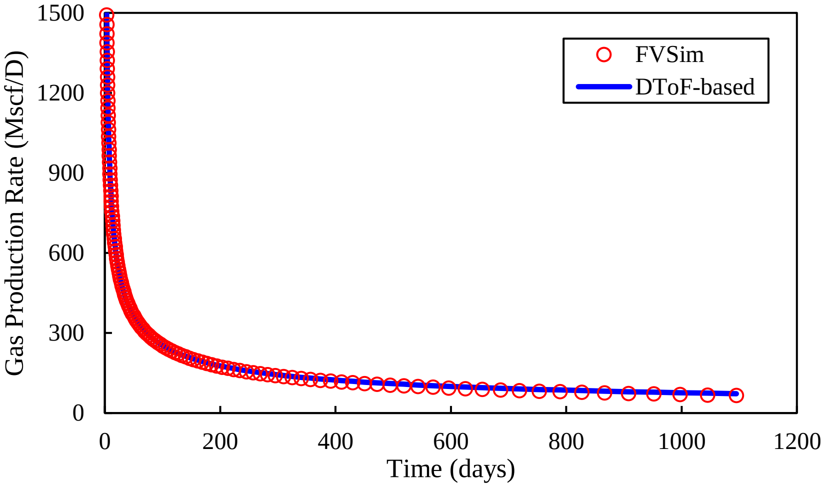

Figure 3.32 Gas production rate comparison (DToF-based vs. finite volume simulation)

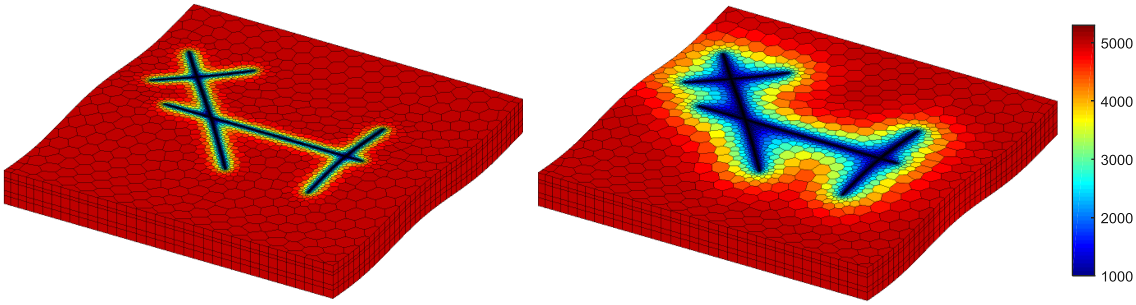

Figure 3.33 Pressure distribution for 3D synthetic model at a) 3 months and b) 3 years

The reservoir performance is then simulated based on the calculated DToF and $w(\tau)$ function. Figure 3.32 shows the comparison of gas production rate from the DToF-based approach and finite volume simulation, where a good agreement is obtained. For this synthetic case, the DToF-based simulation obtains a speedup of 18, which might be higher once the programming is further optimized. The pressure data on the DToF coordinates can be interpolated on the DToF map to obtain the pressure distribution in the 3D physical domain. Figure 3.33 shows the pressure distribution calculated in this manner at 3 months and 3 years, which honors the geometry of the fractures.

This DToF-based approach is also applied to a field-scale problem to demonstrate the applicability. The reservoir properties are based on an Eagle Ford shale well. In this model, four hydraulic stages are created with five fracture per stage and a fracture spacing 100 *ft*. Other key parameters are summarized in Table 3.5.

Table 3.5 Parameters for Eagle Ford shale reservoir

Reservoir size	$2000\times2800\times155\ ft^3$	Bottom-hole pressure	2500 *psi*
Reservoir permeability	150 *md*	Gas viscosity	0.25 *cp*
Reservoir porosity	0.061	Gas compressibility	$1.63\times10^{-4}\ psi^{-1}$
Reservoir pressure	4280 *psi*	Slickwater viscosity	1.5 *cp*
Young's Modulus	$6.11\times10^{6}\ psi$	7.5% HCL viscosity	1.37 *cp.*
Min horizontal stress grad	0.9 *psi/ft*	Linear Gel viscosity	31 *cp*
Pore pressure gradient	0.58 *psi/ft*	Crosslinked Gel vis.	600 *cp*
Overburden stress gradient	1.15 *psi/ft*	No. of perfs per stage	5
Stress anisotropy	1.03	No. of stage	4
Rock compressibility	$3.6\times10^{-6}\ psi^{-1}$	Cluster spacing	100 *ft*

Commercial software, Mangrove, is used to simulate the fracture propagation process using Unconventional Fracture Model (UFM) method (Wu et al. 2012), which takes into account the stress shadow effect and the interaction between hydraulic fractures and natural fractures. The fracturing pumping schedule for the fracture propagation simulation is listed in Table 3.6, and the resulting complex fracture system is shown by

Figure 3.34a. Based on the fracture geometry, the unstructured grids are generated using the force-equilibrium algorithm, and the top-view of the grids is shown by Figure 3.34b.

Table 3.6 Fracturing pumping schedule

	Fluid type	Fluid volume (gals)	Proppant type	Proppant concentration (PPA)
Step 1	Slickwater	10500	-	0.0
Step 2	7.5% HCL	1000	-	0.0
Step 3	Slickwater	30000	-	0.0.
Step 4	Slickwater	8333	100 mesh	0.5
Step 5	Linear Gel	15000	100 mesh	1.0
Step 6	Linear Gel	70000	100 mesh	1.5
Step 7	Crosslinked Gel	74000	100 mesh	2.25
Step 8	Crosslinked Gel	73143	40/70 White	3.0

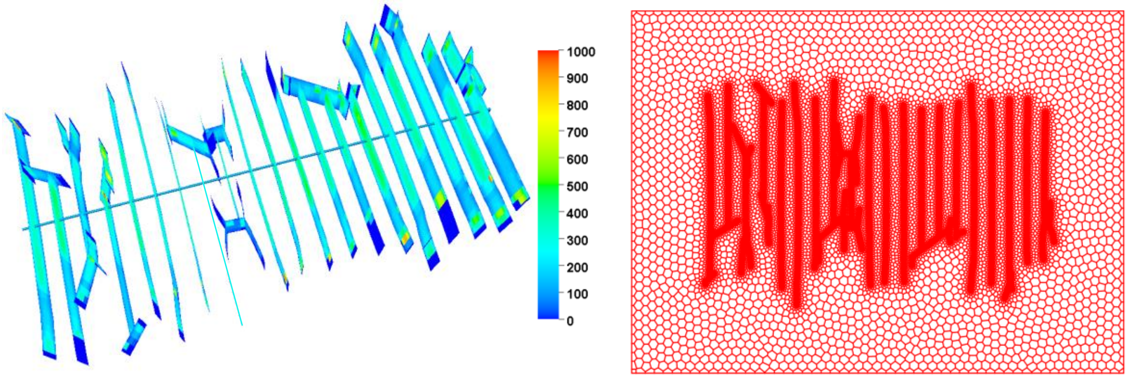

Figure 3.34 a) Complex fracture system generated by Mangrove; b) top-view of unstructured Voronoi cells

Figure 3.35a denotes the DToF map in log10 scale calculated using FMM, from which the fracture geometry is well captured. The $w(\tau)$ function is shown in Figure 3.35b, where we can observe the pressure propagation within the hydraulic fracture, from fracture to formation, fracture interference, and finite boundary effect.

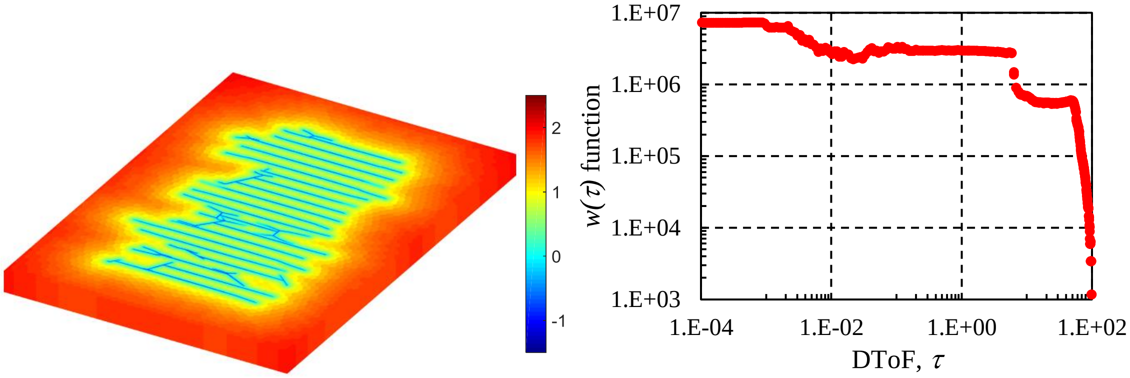

Figure 3.35 a) DToF map (in log10 scale) calculated using FMM; b) $w(\tau)$ function indicating the flow geometry

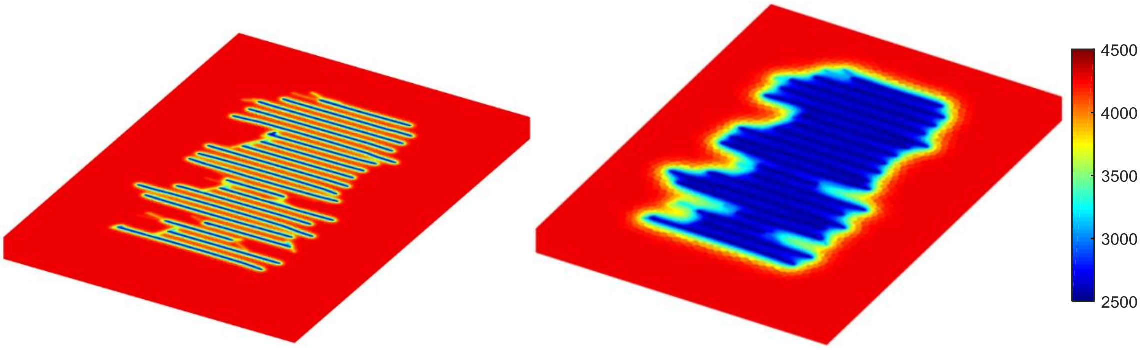

Figure 3.36 Pressure distribution for field-scale model at (a) 3 months (b) 3 years

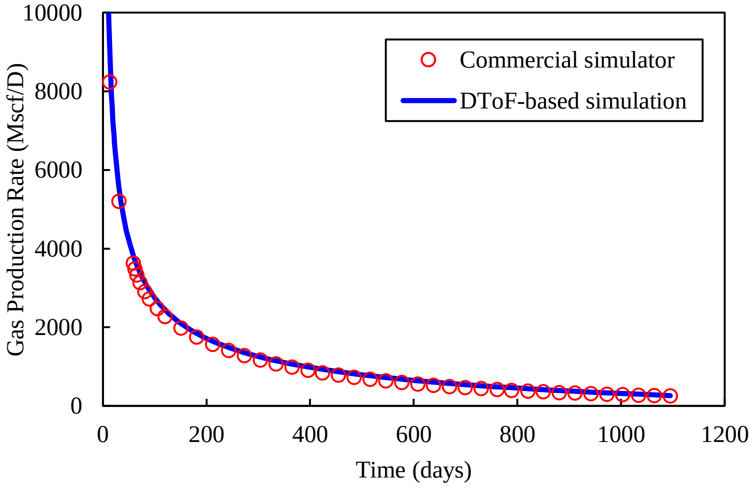

Figure 3.37 Gas production rate comparison (DToF-based vs. commercial simulator)

Figure 3.36 shows the pressure distribution for the multiple fracture field model calculated at 3 months and 3 years. It can be observed that the fractures interference already happens at 3 years based on the pressure distribution in Figure 3.36b. Figure 3.37 shows the comparison of gas production rate from the DToF-based approach and commercial simulator, where a good agreement is obtained as well.

3.8 Conclusions

In this chapter, we extended the DToF-based simulation approach to unstructured grid system so as to better model the fractured reservoirs. We presented the procedure of unstructured mesh generation, which includes a force-equilibrium optimization algorithm to provide the mesh with high quality. Next, we investigated the two constructions of local Eikonal equation solver for unstructured grids, which are based on Fermat’s principle and Eulerian discretization. The performance of these two constructions are compared and the Eulerian discretization approach is extended to anisotropic media. After calculating the DToF with FMM, a novel process of constructing the $w(\tau)$ function is presented and the fluid flow equation is solved numerically. Through the numerical examples, our proposed approach proves to be an efficient workflow to model the fractured reservoirs.

The main conclusions from this study can be summarized as follows:

(1) Unstructured grids allow better characterization of the transient drainage volume for complex fracture systems while the DToF-based simulation provides a rapid simulation of reservoir performance.

(2) A novel scheme is proposed to handle fracture intersections for Voronoi grid systems. The force-equilibrium optimization algorithm proves to be an

efficient approach to optimize the location of Delaunay nodes, which yields unstructured mesh with good mesh quality and uniformity.

(3) We derived a symmetric formula for the 3D Eikonal equation solver based on Fermat's principle. We provided the detailed implementation of Eulerian discretization, especially, the degradation from the tetrahedron to the plane in 3D and the causality requirement constraint.

(4) The construction based on Fermat's principle is more transparent to physical meaning; while the construction based on Eulerian discretization is more straightforwardly be implemented and more easily be extended to anisotropic media.

(5) Based on the numerical test cases in isotropic media, the Fermat's principle and Eulerian discretization yields equivalent results even though they follow different constructions.

(6) After computing the DToF with FMM, all the complex fracture geometry and reservoir heterogeneity information are lumped into the $w(\tau)$ function. And we adopt a new procedure to construct the $w(\tau)$ function without resorting to an explicit calculation of drainage volume.

(7) The accuracy of the DToF-based simulation approach is validated against conventional finite volume simulation, and the applicability is demonstrated through field-scale numerical examples. Compared with conventional finite volume simulation, our proposed approach shows orders of computational reduction.

CHAPTER IV

MODEL-FREE PRODUCTION DATA ANALYSIS BASED ON THE TRANSIENT DRAINAGE VOLUME[*]

4.1 Introduction

Based on our study in previous chapters, the DToF-based simulation approach proves to be an efficient method to model the unconventional reservoirs. However, a high-resolution simulation model is necessary to compute the accurate transient drainage volume. The reality is that a high-resolution simulation model is usually not available while the production and pressure data is abundant for unconventional wells. Based on our knowledge of the transient drainage volume through the development of DToF-based simulation, we propose the model-free production analysis technique (Yang et al. 2015).

In this chapter, we work directly with field production and pressure data to infer the drainage volume, the instantaneous recovery ratio, defined as the ratio of the produced volume to the drainage volume and the $w(\tau)$ function that is related to a combined fracture and reservoir surface area. Our work draws upon the commonly used pressure transient and Rate Normalized Pressure (RNP) concepts. However, it specifically generalizes the

---

[*] Part of data reported in this Chapter is reprinted with permission from “A Novel Approach for Production Transient Analysis of Shale Gas/Oil Reservoirs” by Yang, C., Sharma, V. K., Datta-Gupta, A., & King, M. J. (2015), paper URTEC-2176280-MS presented at the Unconventional Resources Technology Conference, 20-22 Jul., San Antonio, Texas, USA. Copyright [2015] URTeC.

[*] Part of data reported in this Chapter is reprinted with permission from “Rapid Refracturing Candidate Selection in Shale Reservoirs Using Drainage Volume and Instantaneous Recovery Ratio” by Yang, C., Xue, X., Huang, J., Datta-Gupta, A., & King, M. J. (2016), paper URTEC-2459368-MS presented at the Unconventional Resources Technology Conference, 1-3 Aug., San Antonio, Texas, USA. Copyright [2016] URTeC.

concept of the drainage volume from pseudo-steady state flow to transient flow, as is required for unconventional reservoirs, and then infers the underlying flow geometry to help differentiate and analyze different reservoir and fracture properties. The proposed formulation is applied to the analysis of the production data from shale oil reservoirs (Yang et al. 2016). The field data has been interpreted to describe the variations in performance characteristics seen in many wells.

4.2 Background

Unconventional shale gas/oil reservoirs are characterized by extremely low permeability. Due to this low permeability, the time scale for a transient response in unconventional reservoirs is orders of magnitude greater than in conventional reservoirs, which have led to the development of reservoir analyses more akin to conventional reservoir rate and pressure transient techniques. Various analytical techniques are routinely applied, such as decline curve analysis (Arps 1945; Fetkovich 1980; Valko and Lee 2010) and pressure/rate transient analysis (Al-Kobaisi et al. 2006; Ilk et al. 2011; Song and Ehlig-Economides 2011) in unconventional reservoir analysis. Analytical techniques are easy to implement; however, analytical techniques are limited to homogeneous media with simple geometry. Conventional numerical reservoir simulation (Cipolla et al. 2011; Freeman et al. 2009; Sun and Schechter 2015; Yan et al. 2013) can rigorously account for reservoir heterogeneity, complex fracture geometry, different geological components, geo-mechanics effects, and many other physical processes. However, the need to develop a detailed reservoir model instead of utilizing a simpler conceptual model is a significant disadvantage of numerical simulation.

Our earlier studies have emphasized the prediction of the reservoir response given an underlying model. In current study, we work directly with field production and pressure data to infer the drainage volume, and the instantaneous recovery ratio, defined as the ratio of the produced volume to the drainage volume. Our work is similar to late time reservoir analysis in conventional reservoirs where pseudo steady state concepts can be applied (Callard and Schenewerk 1995; Pratikno et al. 2003; Ye and Ayala 2013). It also draws upon the pressure transient concepts and Rate Normalized Pressure (RNP) of Song and Ehlig-Economides (2011). However, it specifically generalizes the concept of the drainage volume from PSS flow to transient flow, as is required for unconventional reservoirs, and then infers the underlying flow geometry to help differentiate and analyze different reservoir and fracture properties.

The unconventional shale reservoir wells experienced sharp production declines. One direct application of our model-free approach would be evaluating the hydraulic fracturing effectiveness and reservoir properties to select candidate wells for refracturing. Studies by Miller et al. (2011) showed that about one-third of the perforation clusters in unconventional reservoirs are not producing, which can be attributed to reasons such as inefficient completion, proppant degradation, near wellbore damage and pressure depletion (Malpani et al. 2015). Refracturing the older underperforming wells, which costs approximately one-third of the total initial completion of a new well (Dahl et al. 2016), becomes an economical practice to enhance the production and gain additional economic returns (Jacobs 2015), which is especially important during the low oil price environment.

Vincent (2011) summarized numerous mechanisms of improving production with refracturing treatments, such as to enlarge fracture geometry, restore or increase fracture conductivity, and contact “new” rock due to reorientation effects. Refracturing can also improve the performance of previous suboptimal design with relatively large cluster spacing and small proppant volumes (Malpani et al. 2015). The benefit of refracturing unconventional shale reservoir is studied theoretically with numerical simulation (Araque-Martinez et al. 2013; Dahl et al. 2016; Huang et al. 2016) and practically by analyzing the performance of field refractured wells, mostly with decline curves analysis (Craig et al. 2012; Diakhate et al. 2015; French et al. 2014; Oruganti et al. 2015). The success of refracturing practice relies on several key factors, such as correct candidate selection, effective diversion techniques and proper execution and diagnostics (Grieser et al. 2016; Lindsay et al. 2016; Vincent 2011). Among these key factors, selecting the correct candidates for refracturing is the first critical step (Grieser et al. 2016; Malpani et al. 2015).

Currently, most of the refracturing candidate selection experiences, mentioned by Vincent (2011) or proposed by Roussel and Sharma (2012, 2013), are limited to conventional reservoirs or tight reservoirs. From the industry practice, the candidate selections are mostly empirical and operator specific (French et al. 2014; Grieser et al. 2016), which causes difficulties for decision-makers when considering multiple factors simultaneously, such as production, completion, and reservoir factors. Zoveidavianpoor et al. (2012) and Wang et al. (2013) proposed refracturing candidate selection based on data mining techniques but the correlations are not so promising. Sinha and Ramakrishnan (2011) proposed a more standardized screening method, which looks at the relationship of the production and completion indicators, but it cannot account for the production history of the horizontal wells. Therefore, an efficient approach hinged on the physics is necessary for refracturing candidate selection.

4.3 Mathematic Models

We have developed a novel formulation of the diffusivity equation to model pressure, rate, and production, especially for trainset reservoir response in unconventional reservoirs. The formulation is derived from the asymptotic (high frequency) limit of the diffusivity equation for the impulse pressure solution. The formulation requires the solution of the Eikonal equation for the DToF and the corresponding pore volume geometry contained within a DToF contour. Once the pore volume geometry is constructed, it may be used as the basis for either numerical or analytic solution. Even through the numerical solutions are more general, the analytic approach is more readily applicable to production data analysis.

4.3.1 Asymptotic Solution to Diffusivity Equation

We may express the diffusivity equation for slightly compressible fluid in terms of the diffusive time of flight, τ, and the $w(\tau)$ function as shown in Zhang et al. (2016).

$$\frac{\partial p}{\partial t} - \frac{1}{w(\tau)} \frac{\partial}{\partial \tau}\left(w(\tau) \frac{\partial p}{\partial \tau} \right) = 0 \tag{4.1}$$

The diffusivity equation is in terms of the pressure, as a function of τ and t. The flux is defined as the total flux which crosses a τ contour. We may express the Darcy flux in terms of the diffusive time of flight, τ.

$$q = c_t w(\tau) \frac{\partial p}{\partial \tau} \tag{4.2}$$

The diffusivity equation may also be stated in terms of the flux instead of the pressure.

$$\frac{\partial q}{\partial t} - w(\tau)\frac{\partial}{\partial \tau}\left(\frac{1}{w(\tau)}\frac{\partial q}{\partial \tau}\right) = 0 \tag{4.3}$$

For a fixed flow rate drawdown in an infinite domain, the initial and boundary conditions are:

$$\begin{array}{lll} t = 0 & p = p_{init} & q = 0 \\ \tau = 0 & & q = q_w \\ \tau \to \infty & p \to p_{init} & q \to 0 \end{array} \tag{4.4}$$

The flux boundary condition at the well is specified at $\tau = 0$, which may be at a finite wellbore radius, r_w, or at a distance of $r = 0$. The later arises for a fault surface or for the line source approximation to a well.

Consider the problem where $w(\tau)$ scales as a power-law in τ. It captures all of the classical line source solutions to the diffusivity equation, as well as the more interesting formulation for the diffusion on a fractal as described by Barker (1988). As these equations are linear in pressure and flux, a dimensional analysis shows that the dimensionless flux function can only depend upon a dimensionless ratio of τ and t. We will specifically work in terms of the Boltzmann variable.

$$\xi = \frac{\tau^2}{4t} \tag{4.5}$$

In contrast, because of the scaling of the boundary conditions at $\tau = 0$, the pressure diffusivity equation will only have a self-similar solution in 2D. The self-similarity of the flux solution allows us to relate t and τ derivatives of the flux and to simplify Eq.4.3.

$$\frac{\partial q}{\partial \tau}=\frac{\tau}{2t}\frac{dq}{d\xi} \text{ and } \frac{\partial q}{\partial t}=-\frac{\tau^2}{4t^2}\frac{dq}{d\xi}=-\frac{\tau^2}{4t^2}\frac{2t}{\tau}\frac{\partial q}{\partial \tau}=-\frac{\tau}{2t}\frac{\partial q}{\partial \tau} \tag{4.6}$$

Hence:

$$\frac{\tau}{2t}\left(\frac{1}{w(\tau)}\frac{dq}{d\tau}\right)+\frac{\partial}{\partial \tau}\left(\frac{1}{w(\tau)}\frac{dq}{d\tau}\right)=0 \tag{4.7}$$

In this form, the diffusivity equation may be integrated explicitly.

$$\frac{1}{w(\tau)}\frac{dq}{d\tau}=-\frac{q_w}{V_d(t)}e^{-\frac{\tau^2}{4t}} \tag{4.8}$$

The spatial dependence of the solution is controlled by the diffusion kernel $e^{-\tau^2/4t}$, the form of which is independent of $w(\tau)$. In contrast, the flux, $q(\tau,t)$, and the drainage volume, $V_d(t)$, explicitly depend upon $w(\tau)$. The flux may be obtained by an additional integration.

$$q(\tau,t)=\frac{q_w}{V_d(t)}\int^{\infty} d\tau.w(\tau).e^{-\frac{\tau^2}{4t}}=\frac{q_w}{V_d(t)}\int^{\infty} dV_p(\tau).e^{-\frac{\tau^2}{4t}} \tag{4.9}$$

The unknown function $V_d(t)$, is determined from the boundary condition at $\tau=0$.

$$V_d(t)=\int_0^{\infty} dV_p(\tau).e^{-\frac{\tau^2}{4t}}=\int_0^{\infty} w(\tau)e^{-\frac{\tau^2}{4t}}d\tau \tag{4.10}$$

This completes the solution of the flux equation for power-law $w(\tau)$.

For more general $w(\tau)$, we can write the diffusivity equation as:

$$\frac{\partial q}{\partial t}+\left(\frac{d\ln w(\tau)}{d\ln\tau}\right)\frac{1}{\tau}\frac{\partial q}{\partial \tau}-\frac{\partial^2 q}{\partial \tau^2}=0 \tag{4.11}$$

If we replace the term in parentheses by either its upper or lower bound, then we again obtain power-law solutions of the form of Eq.4.8, but with differing functions for $V_d(t)$. These provide upper and lower bounds for the flux for general $w(\tau)$, and justify the use of Eq.4.8 as an asymptotic solution to the diffusivity equation in an unbounded reservoir.

4.3.2 Drainage Volume Calculation

For a fixed rate draw-down in an infinite domain, Eq.4.12 and Eq.4.13 provide the starting point for our current production analysis:

$$c_t \frac{\partial p}{\partial t} = \frac{1}{w(\tau)} \frac{\partial q}{\partial \tau} = -\frac{q_w}{V_d(t)} e^{-\tau^2/4t} \tag{4.12}$$

$$V_d(t) = \int_0^\infty w(\tau) e^{-\tau^2/4t} d\tau \tag{4.13}$$

For slowly varying flow rates, following Winestock and Colpitts (1965), we may replace the fixed flow rate by $q_w(t)$. For strong changes, superposition in time may be used instead, or more generally replaced by a convolution integral. Similarly, for multiple wells or no flow boundaries, superposition in space may be used to generalize the right-hand side of the equation. For homogeneous models, these asymptotic solutions are exact. King et al. (2016) provide a detailed comparison of the asymptotic solutions with traditional analytical solutions for different scenarios. For systems with complex flow geometry, these analytic approximations may still be fairly accurate.

The drainage volume of a well has been defined by Matthews et al. (1954) for PSS flow. In our work, we extend their definition to transient flow, based upon the qualitative aspects of the asymptotic solution, as summarized in Table 4.1 and shown in Figure 4.1.

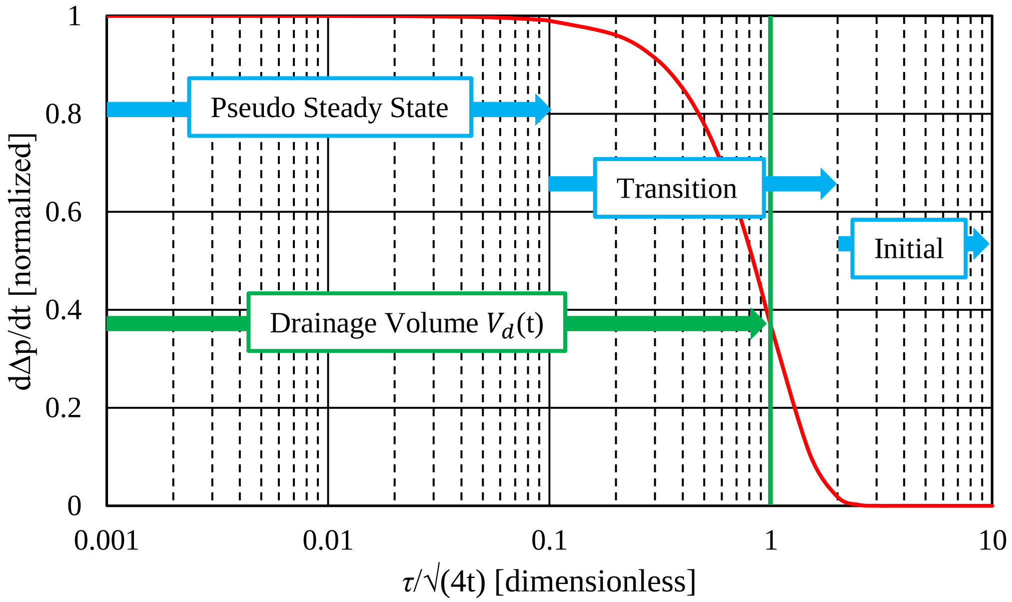

Figure 4.1 Spatial profile of the fixed rate draw-down solution to the asymptotic pressure approximation in terms of the time derivative to the pressure drop, normalized to its value at the well (modified from King et al. (2016))

Table 4.1 Characteristics of the asymptotic pressure solution

Boltzmann Variable	Diffusion Kernel	Characteristic
$\frac{\tau^2}{4t} < 0.01$	$\exp(-\frac{\tau^2}{4t}) > 0.99$	Pseudo-Steady State (PSS)
$0.01 < \frac{\tau^2}{4t} < 0.1$	$0.9 < \exp(-\frac{\tau^2}{4t}) < 0.99$	Near PSS (Transient)
$0.1 < \frac{\tau^2}{4t} < 4$	$0.018 < \exp(-\frac{\tau^2}{4t}) < 0.9$	Transient
$\frac{\tau^2}{4t} > 4$	$\exp(-\frac{\tau^2}{4t}) < 0.018$	Near Initial (Infinite Acting)

The spatial characteristics of these solutions are controlled by the Boltzmann variable, $\tau^2/4t$, which is a dimensionless combination of the diffusive time of flight and time. The exponential in Eq.4.12 is the “diffusion kernel” which controls the solution characteristics for both homogeneous and heterogeneous reservoir models and in arbitrary dimensions. The choice of characteristics is consistent with the general literature discussions of the validity of infinite acting radial flow, Lee (1982), and to field data interpretation of the radius of investigation, Kuchuk (2009), but here expressed in terms of the pressure transient and applied to our general solution.

Let’s describe the characteristics of the solution, starting from the bottom of Table 4.1. For sufficiently large values, $\tau^2/4t > 4$, the diffusion kernel is essentially equal to 0, and the pressure is still at its initial value. For values of $\tau^2/4t$ between 0.01 and 4, we have a moving transient solution where the solution depends upon both τ and t. Finally, for sufficiently small values, $\tau^2/4t < 0.01$, the diffusion kernel is essentially equal to 1, and $\partial p/\partial t$ is independent of τ, i.e., Pseudo-Steady State flow. Since we are in PSS near the well, we may define the drainage volume from production data, following the analysis of Matthews et al. (1954). It is important to recognize that this is the drainage volume within the region of the moving transient solution, and so will increase with time. For conventional reservoirs, the PSS limit will be reached in the entire reservoir and $V_d(t)$ will be the pore volume of the reservoir. However, we have no evidence of reaching the PSS limit in any of the unconventional reservoir examples we have examined, and instead, the drainage volume continues to increase during production. $V_d(t)$ is not the volume produced. Instead, it describes the footprint in the reservoir within which depletion has begun.

Given a model for $w(\tau)$ we may evaluate the drainage volume, $V_d(t)$, and then integrate the equation in time to determine the pressure drop calculated from the initial pressure. This solution is for a fixed rate draw-down.

$$\Delta p\left(\tau,t\right) = q_w \int\limits_{t=0} \frac{dt}{c_t V_d(t)} e^{-\tau^2/4t} \tag{4.14}$$

For instance, $V_d(t) \sim t$ for infinite acting radial flow and this solution is the Ei function. In the PSS limit, it reduces to the ln approximation of the Ei function. Similarly, we may predict the flow rate, given a fixed bottom-hole flowing pressure.

$$q_w\left(t\right) = \Delta p_{wf} \Big/ \int\limits_{t=0} \frac{dt}{c_t V_d(t)} e^{-\tau_w^2/4t} \tag{4.15}$$

In terms of pressure transient analysis, we can directly evaluate the well-test derivative from Eq.4.12 without any further integration.

$$\Delta p'_{wf} = \frac{d\Delta p_{wf}}{d\ln t} = \frac{q_w t}{c_t V_d(t)} e^{-\tau_w^2/4t} \approx \frac{q_w t}{c_t V_d(t)} \tag{4.16}$$

This provides an interpretation of the well-test derivative directly in terms of the drainage volume.

In the absence of a model, $w(\tau)$ is not known, but instead, we have field production data with variable pressure drop and flow rate.

$$\frac{d\Delta p_{wf}(t)}{dt} = \frac{q_w(t)}{c_t V_d(t)} e^{-\tau_w^2/4t} \approx \frac{q_w(t)}{c_t V_d(t)} \tag{4.17}$$

Following the earlier work of Winestock and Colpitts (1965), and of Song and Ehlig-Economides (2011) specifically for unconventional reservoirs, this relationship for the drainage volume may be extended to variable rate production through the use of rate normalized pressure and superposition time. As with previous authors, we approximate superposition time using the material balance time. The drainage volume is evaluated from variable production and pressure data based on the following equations:

$$\frac{1}{V_d\left(t_e\right)} \approx c_t \frac{d}{dt_e}\left(\frac{\Delta p_{wf}\left(t\right)}{q_w(t)}\right) \tag{4.18}$$

$$t_e = \frac{Q(t)}{q_w(t)} \tag{4.19}$$

We may also calculate the Instantaneous Recovery Ratio, defined as the ratio of the produced volume to the drainage volume. The IRR measures how quickly or how efficiently the accessed drainage volume has been produced. Both the operations of the well and the conductivity of the hydraulic fractures in unconventional reservoirs will govern the behavior of IRR curves.

$$IRR\left(t\right) = \frac{Q\left(t\right)}{V_d(t)} \tag{4.20}$$

4.3.3 Inversion Procedure for $w(\tau)$ Function

The $w(\tau)$ function is inverted in a way which truncates the infinite integral to be finite and divides the domain into small intervals with piecewise constant at each interval.

$$V_d(t_i) = \sum_{j=1}^{N} \int_{\tau_a}^{\tau_b} w(\tau) \exp\left(-\frac{\tau^2}{4t_i}\right) d\tau \tag{4.21}$$

Any type of $w(\tau)$ function can be assumed, here $w(\tau)$ is considered as piecewise constant. This is a fair assumption for two reasons: firstly, we are not trying to obtain a purely analytical solution of $w(\tau)$ and it is not possible to do so without an analytical formula for $V_d(t)$; and secondly, it is good approximation as long as a sufficient number of intervals are used. The integral in Eq.4.21 can be explicitly expressed in terms of error function as follows:

$$V_d(t_i) = \sqrt{\pi t_i} \sum_{j=1}^{N} w(\tau_j) \cdot \left(Erf\left(\frac{\tau_{jb}}{2\sqrt{t_i}} \right) - Erf\left(\frac{\tau_{ja}}{2\sqrt{t_i}} \right) \right) \qquad (4.22)$$

We end up solving a linear matrix $\mathbf{A}x = b$, where each term is expressed as Eq.4.23.

$$a_{ij} = \sqrt{\pi t_i} \left(Erf\left(\frac{\tau_{jb}}{2\sqrt{t_i}} \right) - Erf\left(\frac{\tau_{ja}}{2\sqrt{t_i}} \right) \right), \ x_i = w(\tau_i) \text{ and } b_i = V_d(t_i) \qquad (4.23)$$

The error function gets quite close to unity (0.9996), at arguments larger than 2.5, thus the coefficient is small. The coefficient matrix quickly becomes singular, and the entire system is not readily solvable. We can further reduce the upper limit of the integral for particular time t, here we choose $5\sqrt{t}$. For the first step, i.e. smallest time t_1, the $w(\tau_1)$ is considered constant in the entire interval and can be solved directly. And at the n^{th} interval, all previous $w(\tau)$ values have been solved, and the corresponding interval for solved value $w(\tau_i)$ is $\left[2\sqrt{t_{i-1}}, 2\sqrt{t_i}\right]$. We can then build a serious of equations in Eq.4.24, and solve them recursively.

$$V_d(t_1)=\sqrt{\pi t_1}w(\tau_1)\cdot\left(Erf\left(\frac{5\sqrt{t_1}}{2\sqrt{t_1}}\right)-Erf\left(\frac{0}{2\sqrt{t_1}}\right)\right)\approx\sqrt{\pi t_1}w(\tau_1)$$

$$V_d(t_2)=\sqrt{\pi t_2}w(\tau_1)\cdot\left(Erf\left(\frac{2\sqrt{t_1}}{2\sqrt{t_2}}\right)-Erf\left(\frac{0}{2\sqrt{t_2}}\right)\right)+\sqrt{\pi t_2}w(\tau_2)\cdot\left(Erf\left(\frac{5\sqrt{t_2}}{2\sqrt{t_2}}\right)-Erf\left(\frac{2\sqrt{t_1}}{2\sqrt{t_2}}\right)\right)$$

$$\ldots\ldots \tag{4.24}$$

$$V_d(t_n)=\sqrt{\pi t_n}\sum_{j=1}^{n-1}w(\tau_j)\cdot\left(Erf\left(\frac{2\sqrt{t_j}}{2\sqrt{t_n}}\right)-Erf\left(\frac{2\sqrt{t_{j-1}}}{2\sqrt{t_n}}\right)\right)+\sqrt{\pi t_n}w(\tau_n)\cdot\left(Erf\left(\frac{5\sqrt{t_n}}{2\sqrt{t_n}}\right)-Erf\left(\frac{2\sqrt{t_{n-1}}}{2\sqrt{t_n}}\right)\right)$$

Through this way, we can obtain a fairly good $w(\tau)$ function, which shows distinct characteristics and helps to explain the differences of model responses. However, other means of inverting for the $w(\tau)$ function are still worthy of investigation.

4.4 Illustration and Validation

In this subsection, we will illustrate our proposed calculation of drainage volume, instantaneous recovery ratio, and drainage volume derivative, $w(\tau)$, with both single fracture model and multiple fracture models. The accuracy of these calculation is validated against the actual reservoir pore volume.

4.4.1 Single Fracture Model Illustration

We first apply it to a simple model whose flow pattern is well-known: a single infinite conductivity fracture model. In this example, we use a ‘tartan’ grid to model a shale oil reservoir with a single hydraulic fracture. The fracture fully penetrates the reservoir in the vertical direction. The mesh size is 301×213×10 with 0.641 million cells. The grid sizes in the *x* and *z* directions are uniform (*DX* = 8 *ft* and *DZ* = 10 *ft*). The grid size in the *y* direction is logarithmic near the fracture to provide better flow resolution and varies from a minimum width of 0.02 *ft* to a maximum of 30 *ft* (Figure 4.2a). Although it is not necessary to do so, we have set the minimum cell width to match the fracture width. If we had chosen to work with a slightly coarser grid, then both the permeability and porosity would be adjusted to preserve the fracture conductance and the fracture pore volume. The key parameters are summarized in Table 4.2. This single fracture reservoir is produced at a constant bottom-hole pressure of 1000 *psi*.

Table 4.2 Parameters used in the single fracture example

Reservoir size	2408×2400×100 ft^3	Oil FVF (p_{init})	1.37 *bbl*/STB
Initial pressure	5470 *psi*	Fracture porosity	0.30
Matrix porosity	0.046	Fracture permeability	1000 *md*
Matrix permeability	0.0005 *md*	Fracture width	0.24 *in.*
Rock compressibility(p_{init})	1.0×10^{-6} psi^{-1}	Fracture height	100 *ft*
Oil viscosity	0.2 *cp*	Fracture half-length	400 *ft*
Oil compressibility	2.0×10^{-5} psi^{-1}		

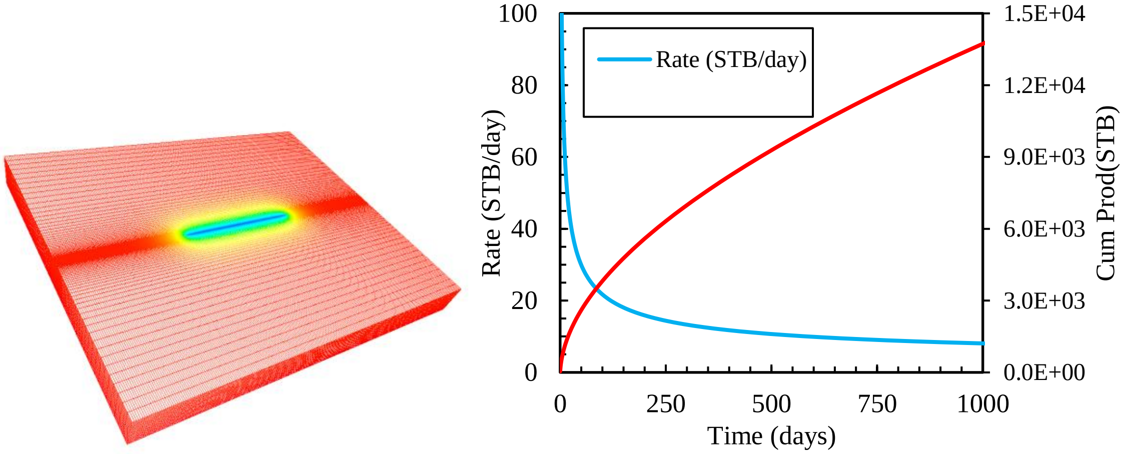

Figure 4.2 a) Single fracture on a tartan grid and its pressure distribution (1000 days); b) Production rate and cumulative production for the single fracture model (1000days)

This synthetic model is simulated with a commercial finite difference reservoir simulator. The rate and cumulative production information for the first 1000 days are given in Figure 4.2b. For the purpose of showing flow regimes including reservoir boundary dominated flow, the model is simulated for approximately 1.0×10^5 days. We do not expect to see the late time flow regimes in practical field applications.

Following the methodology described above, we can obtain the drainage volume, IRR, and $w(\tau)$ function (Figure 4.3). For this simple example, the reservoir pore volume is about $2.66\times10^7\ ft^3$, as the dashed line in Figure 4.3a, and the calculated drainage volume accurately converges to this value. We also intuitively know all the flow regimes, namely early linear flow, radial flow and boundary dominated pseudo-steady state flow. Our analysis in Figure 4.3d accurately captures the response for all the flow regimes. For linear flow, we expect the effective cross-section for flow to remain constant and the drainage volume to increase proportionally to the square root of time. For radial flow, we expect the effective cross-section for flow to increase linearly with τ and for the drainage volume to increase linearly with time. Both of these trends also appear. At late time the drainage volume reaches the pore volume of the reservoir and the effective cross-section for flow should reduce towards zero. The trend of the IRR is interesting. It is plotted on semi-log axes to emphasize the early time behavior. The early time recovery ratio reaches a maximum when the cross-over from linear flow to radial flow begins. In other words, the drainage volume now increases more rapidly than does the produced volume. For late time boundary dominated flow, the drainage volume no longer increases, and the IRR will then increase monotonically with production. The pressure contours are given in Figure 4.4.

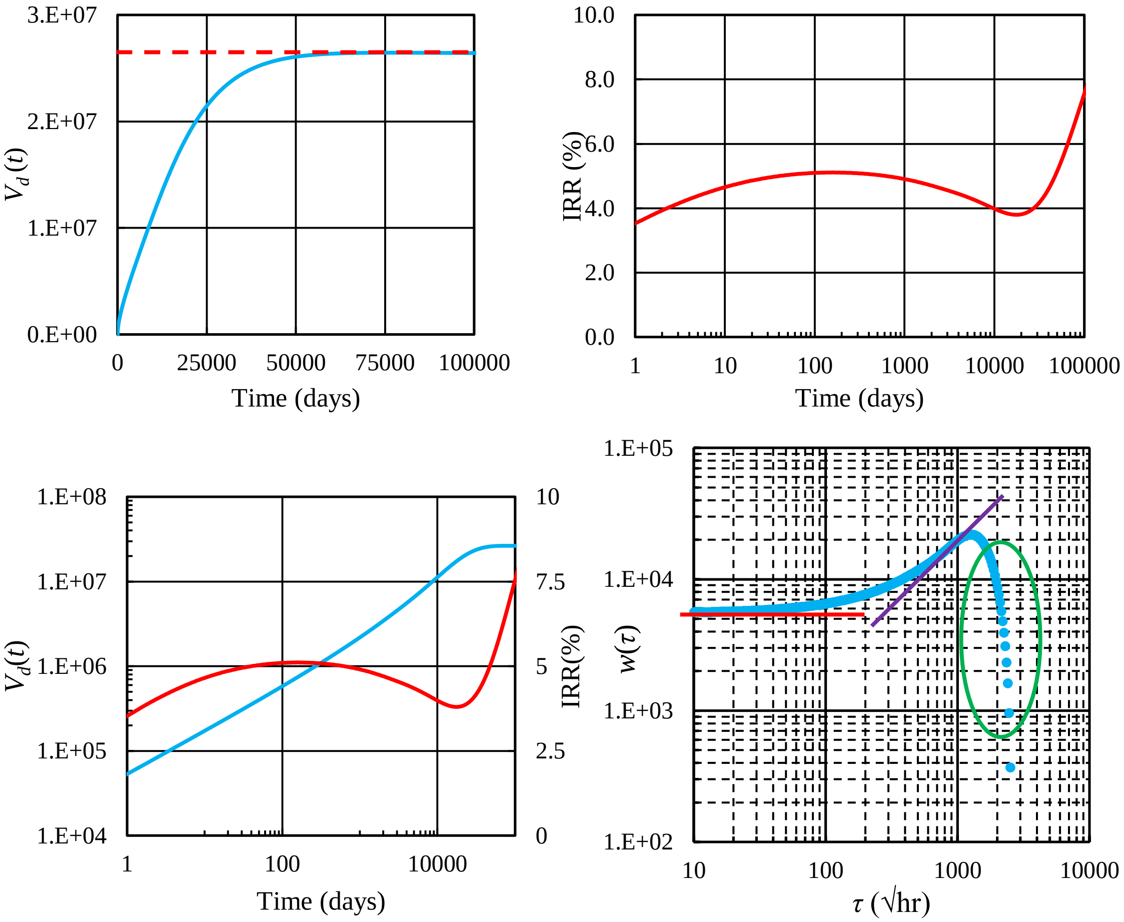

Figure 4.3 Analysis results for single fracture model: a) Drainage volume; b) IRR curve; c) Drainage volume and IRR in the same time scale; d) Drainage volume derivative function

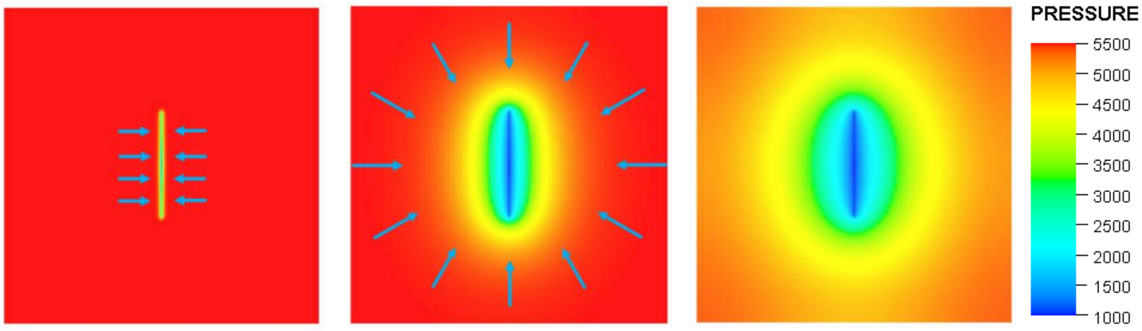

Figure 4.4 Pressure contours for single fracture model: a) Formation linear flow; b) Radial flow; c) Boundary dominated pseudo-steady state flow

4.4.2 Multiple Fracture Model Illustration

The proposed approach is further applied to synthetic multistage hydraulic fractured horizontal wells for sensitivity study. The matrix, fracture, and fluid properties are listed in Table 4.3. For this sensitivity study, four different scenarios are compared: 1) base case (60 clusters with cluster spacing 50 *ft*) produced at a constant bottom-hole pressure of 1000 *psi*; 2) constant rate production at 15 *STB/day*; 3) the same horizontal well length but with fewer clusters (40 clusters with cluster spacing 75 *ft*); 4) shorter horizontal well length (40 clusters with cluster spacing 50 *ft*).

Table 4.3 Parameters used for synthetic models for proposed production data analysis

Reservoir size	2408×6000×100 ft^3	Fracture porosity	0.30
Initial pressure	5470 *psi*	Fracture permeability	1000 *md*
Matrix porosity	0.046	Fracture width	0.24 *in.*
Matrix permeability	0.0001 *md*	Fracture height	100 *ft*
Rock compressibility(p_{init})	1.0×10^{-6} psi^{-1}	Fracture half-length	400 *ft*
Oil viscosity	0.2 *cp*	Number of clusters	40/60
Oil compressibility	2.0×10^{-5} psi^{-1}	Cluster spacing	50/75 *ft*
Oil FVF (p_{init})	1.37 *bbl*/STB		

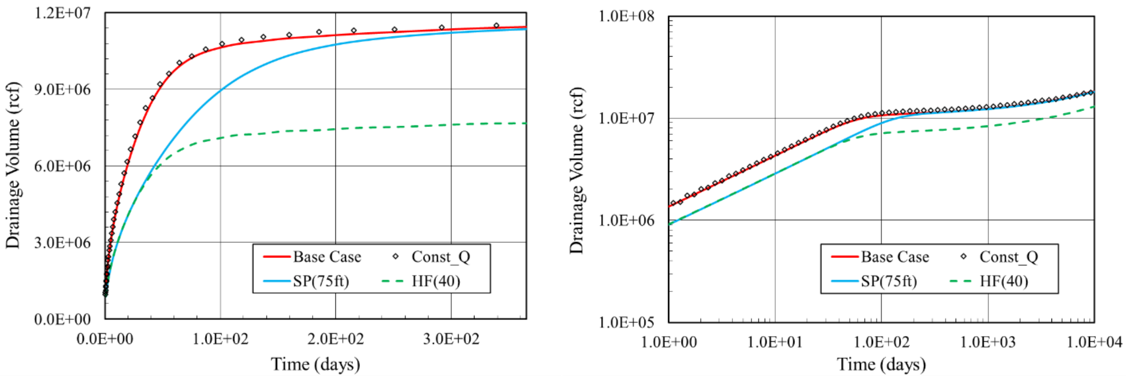

Figure 4.5 Drainage volume comparison: a) in Cartesian scale (first year); b) in log-log scale (1.0×10^4 days)

Figure 4.5 shows the drainage volume comparison for four different cases. The results are quite explanatory. For early time formation linear flow, the drainage volume shows a straight line with a unit slope in log-log plot with time. The good agreement between the base case and the constant rate constraint case validates that the proposed drainage volume is independent of operations. The drainage volume of case 3 agrees with that of case 4 at the early time because both cases share the same number of hydraulic fractures; while the drainage volume of case 3 gradually converges to that of the base case because the flow is into compound linear flow period and the horizontal well length is the controlling factors.

The IRR curves are presented in Figure 4.6. The IRR values start with a relatively high value for constant bottom-hole pressure constant cases because the fractures have an effective infinite conductivity which boosts quite a fast production when drainage volume hasn't increased too much. The bending up sections indicate the fracture interference: the case 3 with larger cluster spacing (75 *ft*) consequently shows the bending up feature later than other cases, with cluster spacing 50 *ft*. The results also indicate that the produced volume increase proportionally with the drainage volume under constant bottom-hole pressure constraint during the linear flow period. This explains the nearly flat section at quite early and late parts. The IRR of the constant rate constant case is significantly different from these of the constant bottom-hole pressure constant cases because the IRR curve incorporates the cumulative fluid production, which depends on and reflects the operation history.

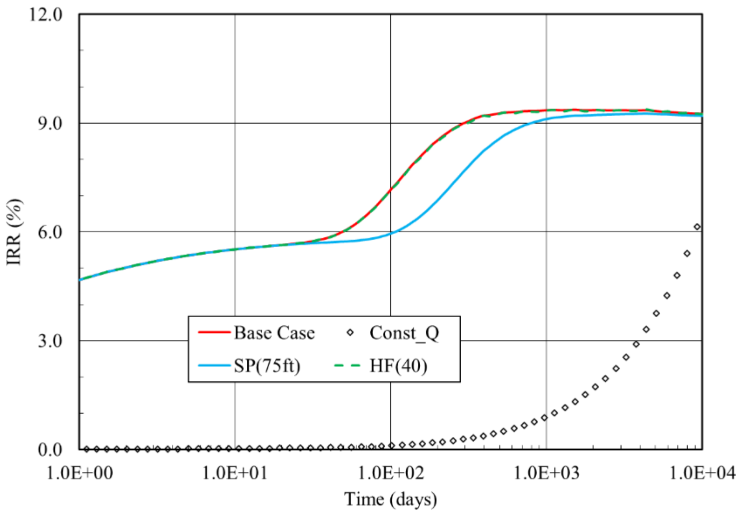

Figure 4.6 IRR curves comparison in semilogx scale (1.0×10^4 days)

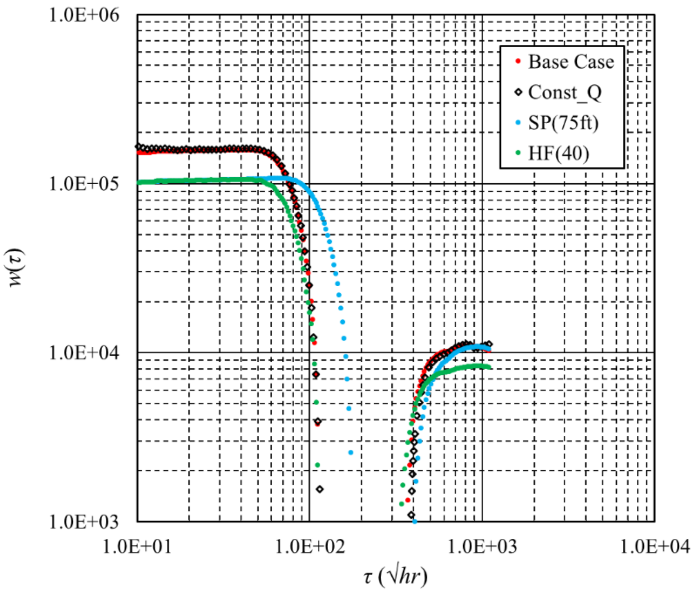

Figure 4.7 $w(\tau)$ function comparison

Figure 4.7 shows the $w(\tau)$ function for the above four synthetic simulations. The $w(\tau)$ function combines the influence of diffusivity and fracture geometry; at given diffusivity condition, all the differences on the $w(\tau)$ plot is attributed to fracture geometry. During the formation linear flow period for infinite conductivity scenario, the drainage volume increases at a rate which is proportional to the fracture surface area. Therefore, we see constant value on the $w(\tau)$ plot at the early time and the cases with 60 clusters show about 50% larger value for the cases with 40 clusters (note that the fracture half-lengths are the same). When the fractures inference with each other, the drainage volume increase slower and the $w(\tau)$ starts to decline. The case 3 with cluster spacing 75 *ft* shows about 50% larger τ value compared to cases with cluster spacing 50 *ft* at the same strength of fracture interference. The second section is due to that the pressure continues propagating in the reservoir as compound linear flow. The results are purely from synthetic simulations; for field cases, where one horizontal well is drilled near another, we don't expect the second section. What's more, due to finite conductivity effect (eg. proppant degradation) or partial penetration effect (eg. proppant sit lower part of the fracture), we don't expect strong flat feature at early part followed by sharp drop, instead the $w(\tau)$ might increases gradually before fracture interference and then drops slowly after fracture interference.

4.5 Procedure for Field Data Application

We now focus on the application of our methodology to field data and describe the specific steps of production data analysis. It is important to emphasize that our approach is model free, that is, we need not invoke any particular flow regimes for analysis of the field data. Thus, our analysis is data-driven rather than model-driven.

Field production data is always discontinuous, which limits our ability to take the derivatives required for the interpretation of drainage volume and instantaneous recovery ratio. These disturbances are either the results of planned or unplanned shutdowns in the production facility. Our primary method of simplifying the analysis is to ignore build-up pressure data taken during shut-ins, and the evaluation of derivatives with respect to cumulative production instead of time. However, further smoothing of the data is required to remove outliers and to capture the trend of the BHP. For shale reservoirs, the first 18 months of production are of particularly importance, and the use of cumulative production will emphasize the data trends for this particular period.

Below we provide a step by step analysis illustration of the procedure using production data from an Eagle Ford oil well. The figures cited appear below the description of these steps.

Step-1: Calculate cumulative production from the data. Well production data typically includes the production rate and the surface pressure. As mentioned previously, we use cumulative production instead of time by accumulating the produced volumes accounting for variable flow rates and variable production times. For shale oil reservoir, like Eagle Ford field, where three phases (oil, gas, and water) coexist, the phases are converted into reservoir condition and treated as combined single phase liquid.

Step-2: Bottom Hole Pressure calculation. The bottom-hole flowing pressure is generally not directly available. Surface production pressure needs to be converted to BHP (Figure 4.8a). This is done based on the pressure traverse calculation through the vertical well length, with production tubing pressure and production rate data. The quality of the

BHP calculation will directly affect the drainage volume calculation, thus more accurate BHP calculation is always preferred.

Step-3: Smoothing of data for adjusted BHP and adjusted rate. BHP is plotted against the cumulative production and data smoothed curve is fitted (Figure 4.8b). On the other hand, the production rate is plotted against time directly and stretched exponential decline curves is fitted (Figure 4.8c). A sufficient number of points are selected so as to obtain a clear trend for the data. The data points are resampled at every cumulative production interval for BHP data fitting and for rate fitting we just ignore all the obviously off-trend points.

Step-4: Computation of material balance time and rate normalized pressure. The smooth curve fit is used to represent the pressure and rate for data analysis. With the integration of fitted rate curve, the corresponding cumulative production is obtained with respect to time (Figure 4.8d). The idea of the analysis is to evaluate the reservoir response under circumstances of no planned or unplanned shut-ins. Therefore, the calculated cumulative is smooth, and it departs away from actual cumulative production during shut-in periods. The material balance time is calculated from fitted rate and cumulative production at the corresponding time and the rate normalized pressure is computed from the fitted BHP and fitted rate at corresponding cumulative production.

Step-5: Calculation of Drainage Volume, IRR and $w(\tau)$. Based on the material balance time and rate normalized pressure computed from the smoothed curves, the drainage volume is calculated from Eq.4.18 and IRR is calculated from Eq.4.20 (Figure 4.9a and Figure 4.9b). The drainage volume should look smooth because it measures the pressure propagation response under circumstances of no shut-ins. On the other hand, the IRR curve is not smooth as it includes the actual production history, which is a result of operation events. Once the drainage volume (Figure 4.9a) is calculated as a function of time, the $w(\tau)$ function can be calculated using Eq.4.21.

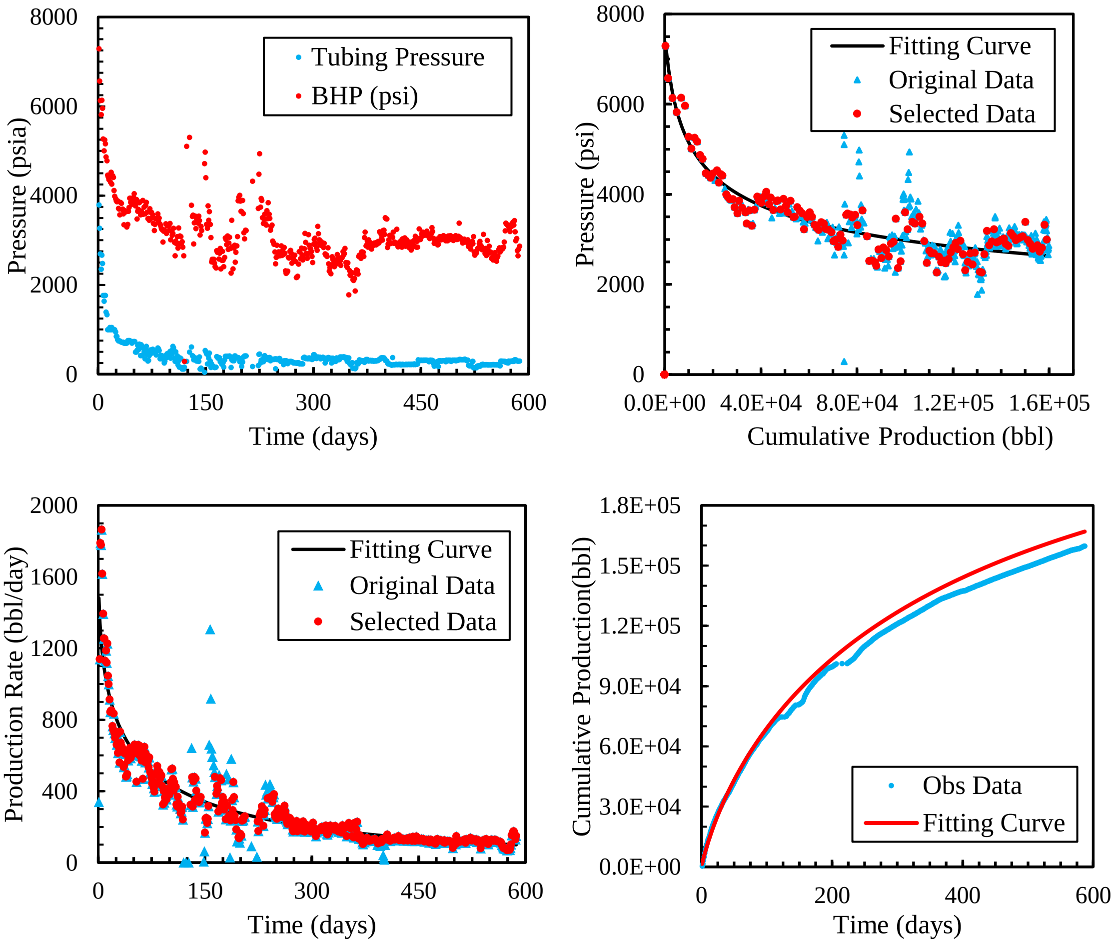

Figure 4.8 a) Pressure versus time; b) Pressure versus cumulative production; c) Production rate versus time; d) Cumulative production versus time

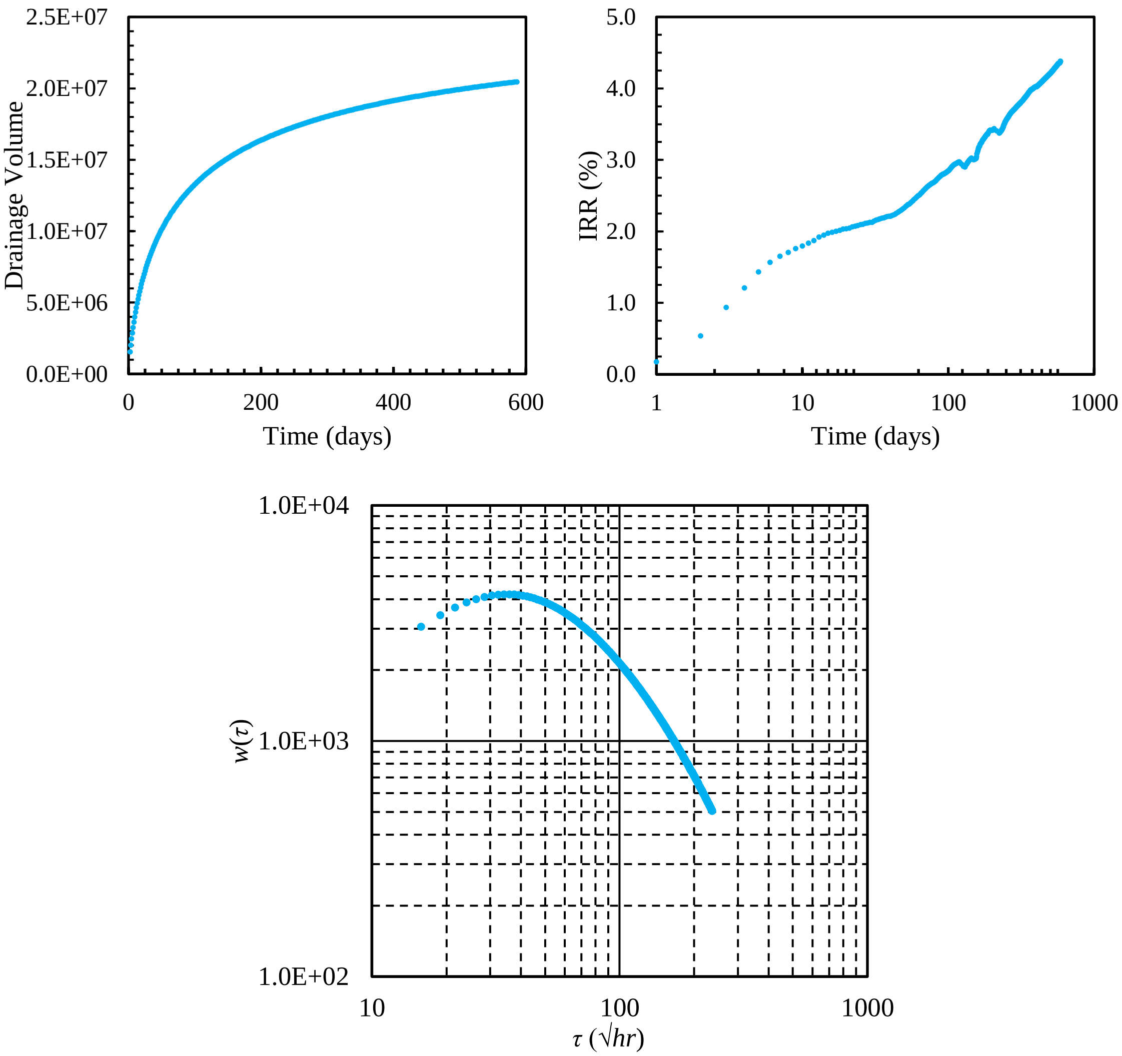

Figure 4.9 a) Drainage volume versus time; b) IRR versus time (semilogx scale); c) $w(\tau)$ function

4.6 Application to Refracturing Candidate Selection

Since the drainage volume evaluates the accessed reservoir volume by the well after hydraulic fracturing while the IRR captures the depletion efficiency, a combination of the two can provide a good understanding of the performance of multistage hydraulic fractured horizontal wells. The drainage volume and IRR of the wells at a particular time are cross-plotted in quadrants, and the wells are qualitatively compared. Large drainage volume values indicate that the wells have access to large reservoir volumes (i.e. large fracture surface area); Large IRR reflects the accessed reservoir volume have been efficiently depleted. Even though the $w(\tau)$ function will not play a direct role in the quadrants analysis, it helps understand the flow geometry and might help determine the appropriate time at which the data is selected for comparison.

4.6.1 Candidate Selection Criteria

In the quadrants (Figure 4.10), we defined four regions, among which wells in the region I have the highest potential for refracturing, followed by wells in region II. Region I wells have accessed large drainage volume but cannot be efficiently depleted, indicating wells have large fracture surface area but poor fracture conductivity, which is more likely to be the hydraulic fracturing using slickwater. High IRR value for region II wells means the drainage volume for this type of wells can be efficiently depleted but the drainage volume itself is limited. This might happen when the proppants are not transported effectively. Figure 4.11 shows the possible scenarios for region I and region II wells respectively. The wells in region III are good wells already; therefore they are not considered for refracturing. One the other hand, the wells in region IV show small drainage volume and low IRR, but they are not good candidates for refracturing because of possible high risk, for instance, due to poor reservoir quality, completion failure, and other well integrity issues.

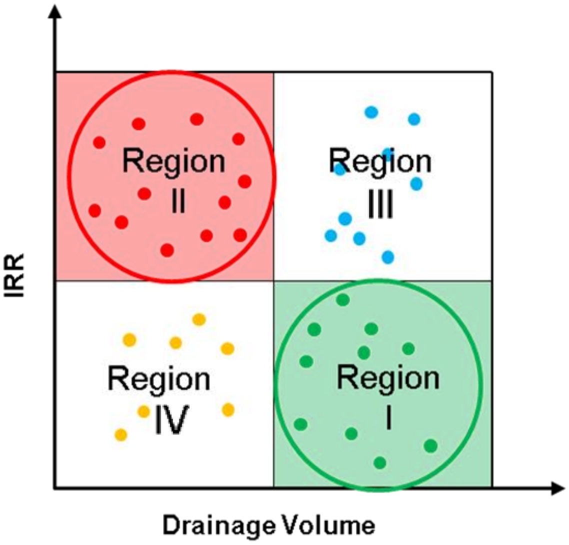

Figure 4.10 Refracturing candidate selection quadrants based on drainage volume and IRR

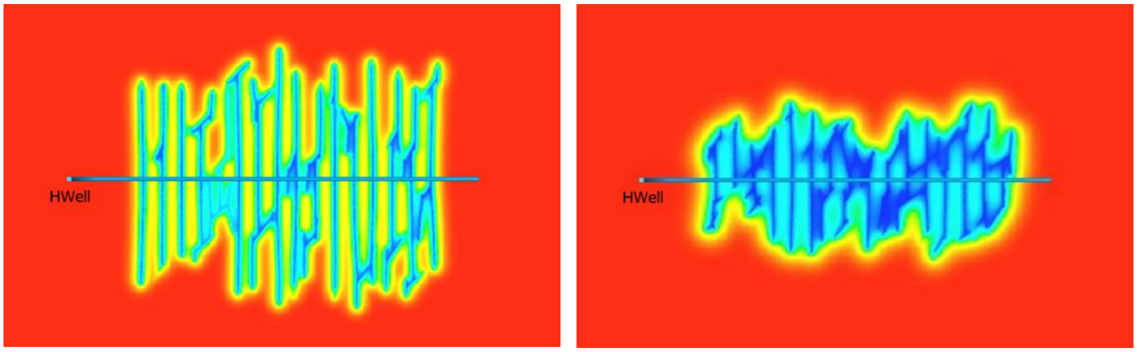

Figure 4.11 Illustration of possible configurations for wells in region I and region II

In the above quadrants, the drainage volume is the well drainage volume normalized by the horizontal well length, which essentially compares the depth into the formation by hydraulic fractures. For the particular time at which the data are compared, we recommend 18 months, which gives sufficient time for fracture interference. Engineers even compare the well performances based on the first six months, twelve months data, considering the sharp rate decline in unconventional shale reservoirs. Based on data availability, using the data at one year or two years will work as well. From our field analysis, it gives consistent results for both one year and 18 months data. One alternative way could be to select the time when the fractures have detectable interference, which could be determined based on the $w(\tau)$ function. In that case, the time for different wells will vary, and it needs more investigation and validation. One additional thing should be noticed that the wells are compared in the qualitative sense. The boundaries to divide these four regions are at the user's discretion, but the recommended value could be the arithmetic mean of all the data points, which is used in our analysis.

Our proposed approach qualitatively compares the wells for the potential of refracturing. It can help narrow down the group of wells for consideration but will not guarantee the feasibility for refracturing because this quadrant analysis is from the perspective of reservoir simulation and it doesn't directly account for drilling and completion factors. From the literature, almost all the refracturing candidate selection methods show a broad range of uncertainty, even for these methods directly derived from historical refractured wells. Therefore, after obtaining a narrowed group of candidate wells, it will be a good practice to further screen them from drilling and completion perspective.

4.6.2 Validation with Synthetic Example

We first demonstrate our approach with numerical simulations on synthetic cases. Our primary goal in this section is to create representative cases which fit in these four quadrants and evaluate their performance after refracturing. The key characteristics for refracturing simulation are the accurate quantification of the depletion-induced stress and pressure field change. Thus, the finite element method is used to solve the coupled reservoir flow and geomechanics model while a cohesive zone model is adopted to simulate the fracture propagation. A fully coupled poroelastic model is used here to simulate both hydraulic fracture propagation and well performance, which can capture not only the complex fracture propagation process in multistage sequential hydraulic fracturing but also production simulation along with proppant degradation. We adopt cohesive zone model to simulate the planar fracture propagation by assuming that the out-of-plane deflection is negligible. Bunger et al. (2012) provide a detailed algorithm to predict when it is valid to neglect the fracture path deflection and use the planar model. The entire simulation is performed based on the commercial finite element package ABAQUS platform, which provides a powerful interface for user-defined material and element properties, as well as complex initial and boundary condition variation through customized subroutines in FORTRAN.

To better understand the fracture growth in space, a fully three-dimensional model coupled with the two-dimensional fluid flow within fracture is required. However, such a 3D model generally requires substantial amounts of input data and can be extremely computationally intensive, which are limited mostly to academic research that provides us insights into the fracture and fluid interaction process in 3D space. Since the designed simulation here considers the effects of depletion on refracturing well performance at the reservoir scale, a 2D plane strain model is adopted to reduce the computational cost while capturing the most critical physics during the hydraulic fracturing process. The main input parameters for the simulation are listed in Table 4.4. To create the synthetic cases fit in these four quadrants, we deliberately select different fracture fluid type, injection amount, and reservoir quality to differentiate these four cases in the initial fracturing. For the region I case, we inject 35 minutes using slickwater. In order to get higher IRR case in region III, we inject 35 minutes using crosslinked gel. The case in region II is obtained with 20 minutes of gel injection. These three cases share the same reservoir quality; however, the case in region IV is assigned with porosity at 3.5%. And we inject 20 minutes of slickwater in the case for region IV.

Table 4.4 Input parameters for candidate selection validation simulation

Young's Modulus	2.58×10^{6} *psi*	Minimum Horizontal Stress	7900 *psi*
Poisson's Ratio	0.3	Maximum Horizontal Stress	8300 *psi*
Fracture Toughness	2000 $psi\cdot in^{1/2}$	Overburden Stress	11000 *psi*
Reservoir Permeability	25 *nd*	Reservoir Thickness	200 *ft*
Porosity	0.065	Injection Rate	60 *BPM*
Reservoir Oil Viscosity	0.36 *cp*	Injection Time	20, 35 *min*
Total Compressibility	3.2×10^{-5} psi^{-1}	Slickwater Viscosity	1.2 *cp*
Initial Reservoir Pressure	4850 *psi*	Gel Viscosity	100 *cp*
Producing BHP	2000 *psi*	Leakoff Coefficient	1.0×10^{-6} $ft/(psi\cdot s)$

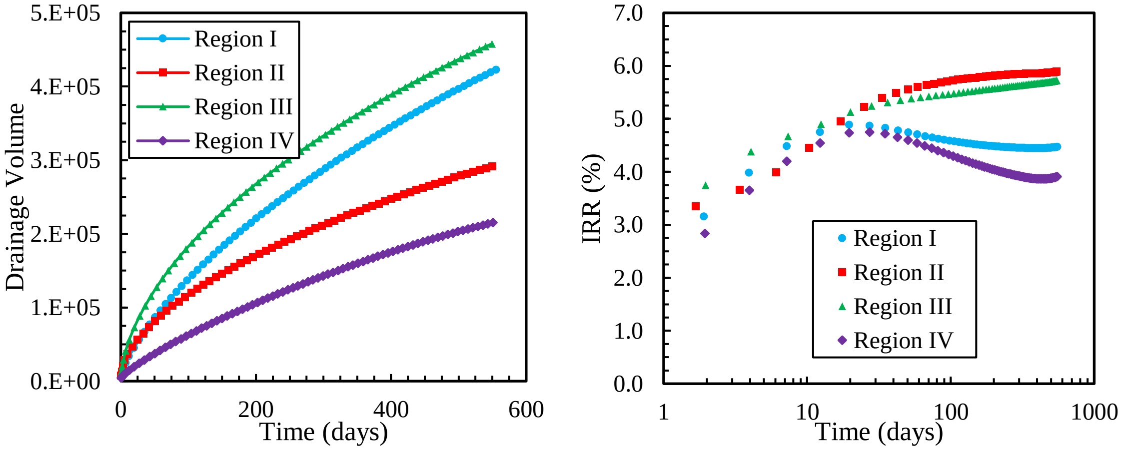

Figure 4.12 a) Drainage volume versus time; b) IRR versus time (semilog x scale)

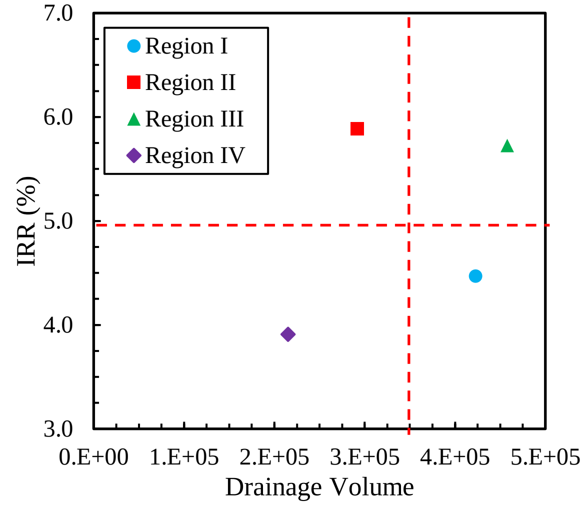

Figure 4.13 Quadrants analysis for synthetic cases

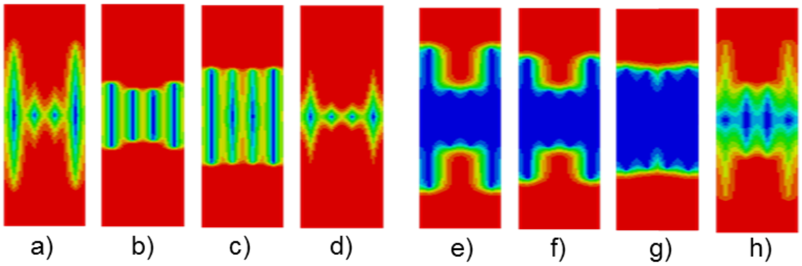

Figure 4.14 Pressure distribution at 18 months (a-d) and 3 years after refracturing (e-h)

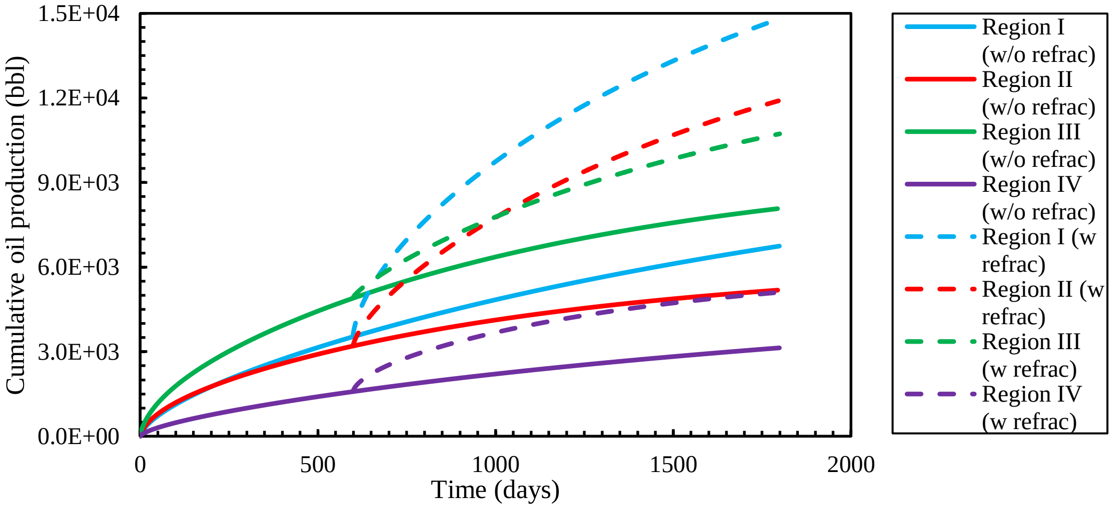

Figure 4.15 Cumulative liquid production for synthetic case with and without refracturing

Table 4.5 Cumulative oil production comparison

Simulation Case	Cum w/o refrac (bbl)	Cum w refrac (bbl)	Incremental Prod (bbl)	Incremental (%)
Region I	6744	14819	**8075**	120
Region II	5182	11897	**6714**	130
Region III	8072	10726	2654	33
Region IV	3135	5108	1973	63

The four synthetic cases are simulated for 18 months. The drainage volume and IRR behavior are calculated with the simulated production data based on our proposed calculation methods (Figure 4.12). The IRR curves for cases in the region I and IV show slight declines, which is due to bilinear flow effects resulting from low fracture conductivity (Figure 4.14a and Figure 4.14d). In this situation, the produced volume increases slower than the drainage volume increases, which can also be seen in radial flow regime. Figure 4.13 shows how these four cases fit in our four quadrants analysis. As mentioned earlier, the boundaries for the quadrants are the arithmetic mean. All the four simulation models are refractured at 600 days with the same refracturing schedule, which is 20 minutes injection of gel in our case, and then simulated for an additional three years. Figure 4.14 displays the pressure distribution at 18 months and additional three years after refracturing. The pressure distribution reflects the fracture properties and reservoir properties. Region I case initially accesses a larger drainage volume with slickwater but cannot be efficiently depleted (Figure 4.14a); after refracturing, it produces quite well (Figure 4.14e). Region II case initially depletes quite well but with a smaller drainage volume (Figure 4.14b); it also increases drainage volume after refracturing but not as much as the region I case (Figure 4.14f). Due to the depletion-induced stress and pressure field change, the fractures of region III case don't show a significant increase (Figure 4.14c and Figure 4.14g). Region IV case doesn't show much depletion either before or after refracturing because of poor reservoir quality (Figure 4.14d and Figure 4.14h). Figure 4.15 shows the cumulative oil production comparisons with and without refracturing, and the actual numbers at the end of the simulation are listed in Table 4.5. From the comparison, we see the region I case gives the best refracturing improvement, followed by the region II case, in terms of increased cumulative production.

4.6.3 Field Case Application

Here we discuss the analysis of shale oil production data from the Eagle Ford field. These wells are at a depth of 11,000 *ft*, with an initial reservoir pressure of about 8125 *psi*. Reservoir temperature is 270 ^{o}F, average porosity of 8.2% and permeability in the range of 100-20000 *nd*. Wells have multiphase fluid flow with oil as the main fluid component. All phases are converted to reservoir conditions and combined to obtain the produced volume in reservoir barrels. Eight wells are studied here, where well 1-4H have about 950 days of production data, and well 9-12H have 585 days.

Following the procedures described above, the drainage volume and IRR are computed for these eight Eagle Ford wells (Figure 4.16). They show quite similar trends: the drainage volume quickly increases and then gradually become stable; the IRR monotonically increase with some fluctuations, which is the combination results of approximately constant pressure constraint and artificial shut-ins. Then the drainage volume and IRR information are put into quadrants analysis. To investigate the sensitivity of selection drainage volume and IRR information at different times, we show both results at 12 months and 18 months (Figure 4.17).

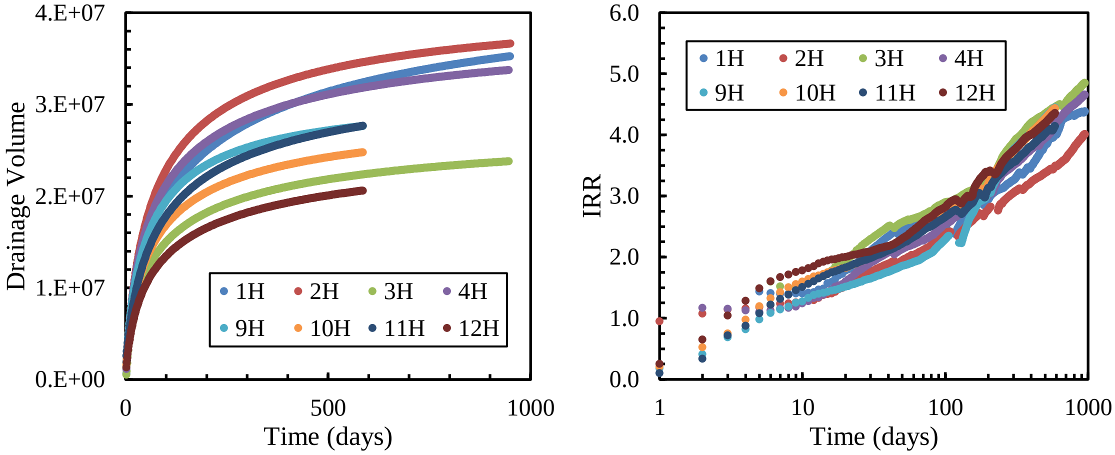

Figure 4.16 a) Drainage volume versus time; b) IRR versus time (semilogx scale) for eight Eagle Ford wells

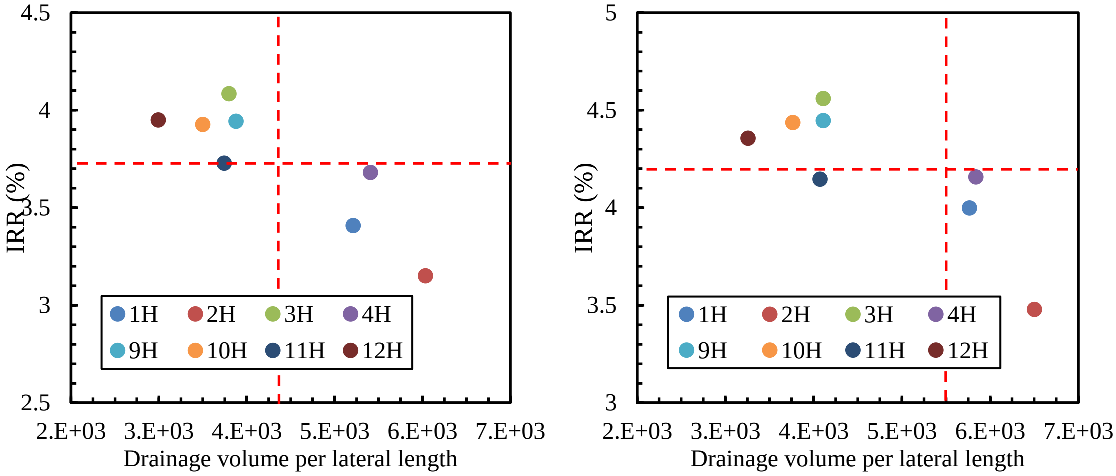

Figure 4.17 Refracturing candidate selection quadrants a) at 12 months; b) at 18 months

Based on our analysis and what synthetic simulations demonstrate, well 2H shows the highest potential for refracturing and the effort should be increasing the fracture conductivity. Well 1H then might be the second consideration. Since none of these wells have been refractured, we cannot validate the result from the performance after refracturing. We further analyze our results by comparing current cumulative production (Figure 4.18). The recommended well 2H won't necessarily be the least produced well, considering the risk of refracturing success.

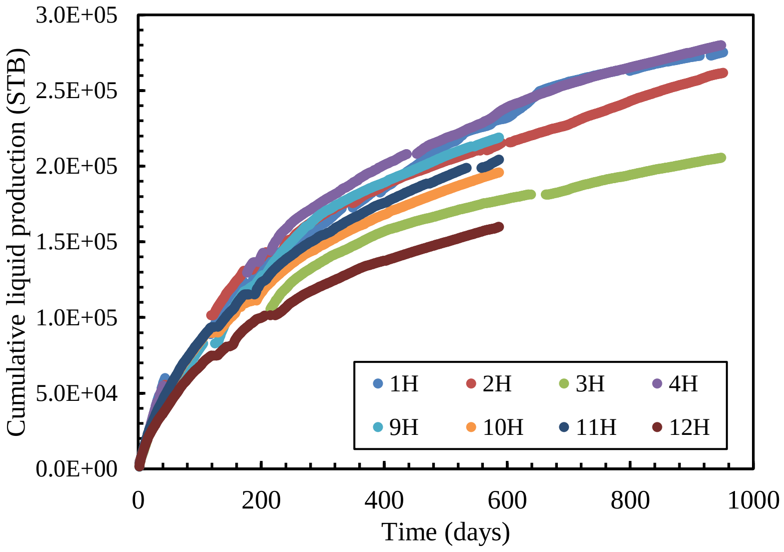

Figure 4.18 Cumulative liquid production for eight Eagle Ford wells

4.7 Conclusions

This chapter introduces a novel method of production analysis which attempts to answer what is the drainage volume of a well, where is this drainage volume and how effective is the depletion of the drainage volume. The method of analysis is based upon the use of the DToF as a spatial coordinate, and the solution of an equivalent 1D diffusivity equation. The pressure and rate response are then a consequence of the pressure wave propagation in the reservoir, with an effective cross-section for flow proportional to a function $w(\tau)$ which effectively characterizes the geometry of the drainage volume of the reservoir. We worked directly with production and pressure data to infer the drainage volume, the instantaneous recovery ratio, and the drainage volume geometry. This information is used to differentiate the performance of a group of wells and applied to select the candidate wells for refracturing.

The main conclusions from this study can be summarized as follows:

(1) The drainage volume measures how much reservoir volume is accessed by the hydraulic fractured well; the IRR provides information about how effectively the accessed drainage volume has been produced. The drainage volume derivative, $w(\tau)$, provides diagnostics to thefracture geometry and reservoir properties.

(2) This approach differs from our previous studies as the analysis is not model-based but is instead driven directly by the field production data itself. Our approach differs from current approaches in pressure (and rate) transient analysis through an extension of the definition of the drainage volume and the IRR ratio based upon our asymptotic solutions to the diffusivity equation.

(3) The four quadrants analysis to identify the refracturing candidates is based on the competition between the produced volume and drainage volume. The drainage volume measure how much reservoir pore volume is accessed while the IRR measures how efficiently the accessed volume is depleted.

(4) Based on our observation, the wells which already show better access to reservoir volumes but poor depletion rates provide a higher potential for refracturing by increasing the fracture conductivity.

CHAPTER V

SUMMARY

5.1 Summary and Conclusions

In this dissertation, we investigated rapid simulation approach and novel analysis techniques for unconventional reservoirs. All the simulation and analysis rely on the asymptotic solution to the diffusivity equation, leading to the diffusive time of flight (DToF) to capture reservoir heterogeneity and complex fracture geometry. We first adopted DToF-based simulation as a forward simulator and developed a systematic and efficient fracture design and optimization workflow. Then, we extended the DToF-based simulation to unstructured grid system to better capture the complex fracture geometry. Finally, we proposed a model-free production data analysis technique based on our cumulative understanding of the DToF and transient drainage volume.

We extended the DToF-based simulation to dual porosity system and applied it as the rapid forward simulator for the multistage hydraulic fracture design and optimization. DToF-based simulation is demonstrated to be an efficient approach to compute the well performance in unconventional reservoirs. It shows good agreement with commercial finite difference based simulators at a fraction of computation time, which is ideal for optimization process where hundreds or thousands of simulations are necessary. The optimization process is carried out through a derivative-free evolutionary algorithm, genetic algorithm. We demonstrated the proposed workflow with a synthetic multistage hydraulic fracture model and showed the capability to account for the geologic uncertainty. The optimum design with consideration of the uncertainty provides superior results on blind test models.

We extended this DToF-based simulation from Cartesian and corner point grid system to unstructured grids to better characterize the complex fracture geometry induced by hydraulic fracturing job in fractured reservoirs. The local Eikonal equation solvers based on Fermat's principle and Eulerian discretization for unstructured grids are investigated and compared. The construction based on Fermat's principle is more transparent to physical meaning; while the construction based on Eulerian discretization is more straightforwardly implemented and easily extended to anisotropic media. Based on the numerical examples, the Fermat's principle and Eulerian discretization yield equivalent result even though they follow distinctive constructions. Numerical examples are presented to illustrate the power and validity of this extended DToF-based simulation.

We proposed a model-free production data analysis method to analyze the performance of unconventional reservoirs. The transient drainage volume is derived directly based on the pressure and production rate. We further defined the drainage volume derivative and instantaneous recovery ratio, which can measure how effectively the reservoir has been stimulated by the hydraulic fractures. This technique is then applied to select the candidate wells for refracturing. We proposed four quadrants analysis to identify the refracturing candidates, based on the competition between the produced volume and drainage volume. Based on our observation, the wells which already show better access to reservoir volumes but poor depletion rates provide a higher potential for refracturing by increasing the fracture conductivity.

5.2 Recommendations

Based on the experiences gained from this study, several recommendations can be drawn for future further investigation:

(1) For the application of the DToF-based simulation to the unstructured grids system, efforts are necessary to more efficiently characterize the complex fracture system and construct the unstructured grids. An alternative approach is to take advantage of unstructured grids generated from commercial software, Mangrove; however, this grid information is currently not accessible for general users.

(2) For the implementation of the local Eikonal solver for unstructured grids, calculation of all the degraded scenarios because of causality violation and the computation of causality check might reduce the computational efficiency of FMM. Therefore, the optimized local Eikonal solver is worth investigation, especially for anisotropic media.

(3) The inversion of the drainage volume geometry, $w(\tau)$ from calculated drainage volume is implemented using a simple formula, with piecewise constant assumption. More robust and accurate solution of this Fredholm integral equation of the first kind can allow quantitative analysis of the characteristic of $w(\tau)$ function, as being briefly summarized in Appendix C.

(4) For the model-free production data analysis, current derivations are directly applicable for single phase slightly compressible liquid. It is worthwhile to be extended into highly compressible fluids, such as gas, and multi-phase fluids.

It will be substantially significant if more quantitative results can be inferred from this model-free production data analysis to characterize the reservoir and fracture properties.

(5) For field application of the model-free production data analysis, the current data smoothing technique assumed specific functional form. It is necessary to investigate non-parametric regression/smoothing technique, such as B-spline. Besides, our refracturing candidate selection is mainly from the reservoir engineering perspective, integrating the drilling and completion information might lead to more reliable selection results.

NOMENCLATURE

BHP = Bottom-hole Pressure

DFM = Discrete Fracture Model

DFN = Discrete Fracture Network

DToF = Diffusive Time of Flight

EDFM = Embedded Discrete Fracture Model

FMM = Fast Marching Method

GA = Genetic Algorithm

IRR = Instantaneous Recovery Ratio

NPV = Net Present Value

PSS = Pseudo-Steady State

RNP = Rate Normalized Pressure

c_t = total compressibility (psi^{-1})

k = permeability, (*md*)

$\overset{=}{\mathbf{k}}$ = permeability tensor, (*md*)

p = pressure, *psi*

∇p = gradient of pressure, *psi/ft*

p_{wf} = bottom-hole pressure, *psi*

q = flux (*STB/day*, *Mscf/day*)

r = distance, *ft*

t = time (*hr*)

t_e = material balance time (*hr*)

$\vec{u}$ = Darcy velocity (*ft/hr*)

$w(\tau)$ = drainage volume derivative ($ft^3/hr^{-1/2}$)

$\vec{x}$ = spatial coordinate vector

B = formation volume factor (*bbl/STB, rcf/Mscf*)

Q = cumulative production (*STB, Mscf*)

$V_p(\tau), V_p(t)$ = drainage pore volume (ft^3)

α = diffusivity (ft^2/hr)

ϕ = porosity

μ = viscosity (*cp*)

θ = angle parameter (^{o})

ρ = fluid density (lb/ft^3)

σ = shape factor (ft^{-2})

τ = diffusive time of flight (DToF) ($hr^{1/2}$)

$\nabla\tau$ = gradient of DToF

REFERENCES

Agarwal, R.G. 2010. Direct Method of Estimating Average Reservoir Pressure for Flowing Oil and Gas Wells. Society of Petroleum Engineers. DOI: 10.2118/135804-MS.

Al-Kobaisi, M., Ozkan, E., Kazemi, H. et al. 2006. Pressure-Transient-Analysis of Horizontal Wells with Transverse, Finite-Conductivity Fractures. Petroleum Society of Canada. DOI: 10.2118/2006-162.

Araque-Martinez, A., Rai, R., Boulis, A. et al. 2013. A Systematic Study for Refracturing Modeling under Different Scenarios in Shale Reservoirs. Society of Petroleum Engineers. DOI: 10.2118/165677-MS.

Arps, J.J. 1945. Analysis of Decline Curves. *Transactions of the AIME* **160** (1). DOI: 10.2118/945228-G

Barker, J.A. 1988. A Generalized Radial Flow Model for Hydraulic Tests in Fractured Rock. *Water Resources Research* **24** (10): 1796-1804. DOI: 10.1029/WR024i010p01796

Branets, L.V., Ghai, S.S., Lyon, S.L. et al. 2009. Challenges and Technologies in Reservoir Modeling. *Communications in Computational Physics* **6** (1): 1-23.

Bunger, A.P., Zhang, X., and Jeffrey, R.G. 2012. Parameters Affecting the Interaction among Closely Spaced Hydraulic Fractures. *SPE Journal* **17** (1). DOI: 10.2118/140426-PA

Callard, J.G. and Schenewerk, P.A. 1995. Reservoir Performance History Matching Using Rate/Cumulative Type-Curves. Society of Petroleum Engineers. DOI: 10.2118/30793-MS.

Cheng, H., Dehghani, K., and Billiter, T.C. 2008. A Structured Approach for Probabilistic-Assisted History Matching Using Evolutionary Algorithms: Tengiz Field Applications. Society of Petroleum Engineers. DOI: 10.2118/116212-MS.

Cipolla, C.L., Lolon, E.P., Erdle, J.C. et al. 2010. Reservoir Modeling in Shale-Gas Reservoirs. *SPE Reservoir Evaluation & Engineering* **13** (4). DOI: 10.2118/125530-PA

Cipolla, C.L., Maxwell, S.C., and Mack, M.G. 2012. Engineering Guide to the Application of Microseismic Interpretations. Society of Petroleum Engineers. DOI: 10.2118/152165-MS.

Cipolla, C.L., Weng, X., Mack, M.G. et al. 2011. Integrating Microseismic Mapping and Complex Fracture Modeling to Characterize Hydraulic Fracture Complexity. Society of Petroleum Engineers. DOI: 10.2118/140185-MS.

Clarkson, C.R., Nobakht, M., Kaviani, D. et al. 2012. Production Analysis of Tight-Gas and Shale-Gas Reservoirs Using the Dynamic-Slippage Concept. *SPE Journal* **17** (1). DOI: 10.2118/144317-PA

Craig, M.S., Wendte, S.S., and Buchwalter, J.L. 2012. Barnett Shale Horizontal Restimulations: A Case Study of 13 Wells. Society of Petroleum Engineers. DOI: 10.2118/154669-MS.

Cui, J., Yang, C., Zhu, D. et al. 2016. Fracture Diagnosis in Multiple-Stage-Stimulated Horizontal Well by Temperature Measurements with Fast Marching Method. *SPE Journal* **21** (06). DOI: 10.2118/174880-PA

Dahl, J., Dhuldhoya, K., Vaidya, R. et al. 2016. An Evaluation of Completion Effectiveness in Hydraulically Fractured Wells and the Assessment of Refracturing Scenarios. Society of Petroleum Engineers. DOI: 10.2118/179136-MS.

Datta-Gupta, A. and King, M.J. 2007. *Streamline Simulation: Theory and Practice*. Textbook Series. Richardson, Texas: SPE. Original edition. ISBN. 978-1555631116

Datta-Gupta, A., Xie, J., Gupta, N. et al. 2011. Radius of Investigation and Its Generalization to Unconventional Reservoirs. *Journal of Petroleum Technology* **63** (7). DOI: 10.2118/0711-0052-JPT

Dershowitz, B., LaPointe, P., Eiben, T. et al. 2000. Integration of Discrete Feature Network Methods with Conventional Simulator Approaches. *SPE Reservoir Evaluation & Engineering* **3** (2). DOI: 10.2118/62498-PA

Diakhate, M., Gazawi, A., Barree, R.D. et al. 2015. Refracturing on Horizontal Wells in the Eagle Ford Shale in South Texas - One Operator's Perspective. Society of Petroleum Engineers. DOI: 10.2118/173333-MS.

Edelsbrunner, H. 2001. *Geometry and Topology for Mesh Generation*: Cambridge University Press. Original edition. ISBN 978-0521682077.

Fan, L., Thompson, J.W., and Robinson, J.R. 2010. Understanding Gas Production Mechanism and Effectiveness of Well Stimulation in the Haynesville Shale through Reservoir Simulation. Society of Petroleum Engineers. DOI: 10.2118/136696-MS.

Fetkovich, M.J. 1980. Decline Curve Analysis Using Type Curves. *Journal of Petroleum Technology* **32** (6). DOI: 10.2118/4629-PA

Field, D.A. 1988. Laplacian Smoothing and Delaunay Triangulations. *Communications in Applied Numerical Methods* **4** (6): 709-712. DOI: 10.1002/cnm.1630040603

Fisher, M.K., Wright, C.A., Davidson, B.M. et al. 2005. Integrating Fracture Mapping Technologies to Improve Stimulations in the Barnett Shale. *SPE Production & Facilities* **20** (2). DOI: 10.2118/77441-PA

Fomel, S. and Sethian, J.A. 2002. Fast-Phase Space Computation of Multiple Arrivals. *Proceedings of the National Academy of Sciences* **99** (11): 7329-7334.

Freeman, C., Moridis, G.J., Ilk, D. et al. 2010. A Numerical Study of Transport and Storage Effects for Tight Gas and Shale Gas Reservoir Systems. Society of Petroleum Engineers. DOI: 10.2118/131583-MS.

Freeman, C.M., Moridis, G.J., Ilk, D. et al. 2009. A Numerical Study of Performance for Tight Gas and Shale Gas Reservoir Systems. Society of Petroleum Engineers. DOI: 10.2118/124961-MS.

Freitag, L.A. and Ollivier-Gooch, C. 1997. Tetrahedral Mesh Improvement Using Swapping and Smoothing. *International Journal for Numerical Methods in Engineering* **40** (21): 3979-4002.

French, S., Rodgerson, J., and Feik, C. 2014. Re-Fracturing Horizontal Shale Wells: Case History of a Woodford Shale Pilot Project. Society of Petroleum Engineers. DOI: 10.2118/168607-MS.

Fujita, Y., Datta-Gupta, A., and King, M.J. 2016. A Comprehensive Reservoir Simulator for Unconventional Reservoirs That Is Based on the Fast Marching Method and Diffusive Time of Flight. *SPE Journal* **21** (6). DOI: 10.2118/173269-PA

Grieser, B., Calvin, J., and Dulin, J. 2016. Lessons Learned: Refracs from 1980 to Present. Society of Petroleum Engineers. DOI: 10.2118/179152-MS.

Hansen, P.C. 1992. Numerical Tools for Analysis and Solution of Fredholm Integral Equations of the First Kind. *Inverse Problems* **8** (6): 849-872.

Hassouna, M.S. and Farag, A.A. 2007. Multistencils Fast Marching Methods: A Highly Accurate Solution to the Eikonal Equation on Cartesian Domains. *IEEE Transactions on Pattern Analysis and Machine Intelligence* **29** (9): 1563-1574. DOI: 10.1109/TPAMI.2007.1154

Heinemann, Z.E., Brand, C.W., Munka, M. et al. 1991. Modeling Reservoir Geometry with Irregular Grids. *SPE Reservoir Engineering* **6** (2). DOI: 10.2118/18412-PA

Holditch, S.A. 2010. Shale Gas Holds Global Opportunities. *The American Oil & Gas Reporter, August 2010 Editor's Choice.*

Holland, J.H. 1992. Genetic Algorithms. *Scientific American* **267** (1): 66-72.

Huang, J., Yang, C., Xue, X. et al. 2016. Simulation of Coupled Fracture Propagation and Well Performance under Different Refracturing Designs in Shale Reservoirs. Society of Petroleum Engineers. DOI: 10.2118/180238-MS.

Ilk, D., Currie, S.M., and Blasingame, T.A. 2010. Production Analysis and Well Performance Forecasting of Tight Gas and Shale Gas Wells. Society of Petroleum Engineers. DOI: 10.2118/139118-MS.

Ilk, D., Okouma Mangha, V., and Blasingame, T.A. 2011. Characterization of Well Performance in Unconventional Reservoirs Using Production Data Diagnostics. Society of Petroleum Engineers. DOI: 10.2118/147604-MS.

Jacobs, T. 2015. Changing the Equation: Refracturing Shale Oil Wells. *Journal of Petroleum Technology* **67** (4). DOI: 10.2118/0415-0044-JPT

Kappa. 2013. Kappa Unconventional Resources, October 2013, Http://Www.Kappaeng.Com/Documents/Flip/Ur-Brochure/ (Accessed Nov.14, 2016). In *Kappa Reading Room Brochure.*

Karimi-Fard, M., Durlofsky, L.J., and Aziz, K. 2004. An Efficient Discrete-Fracture Model Applicable for General-Purpose Reservoir Simulators. *SPE Journal* **9** (2). DOI: 10.2118/88812-PA

Kazemi, H., Merrill, L.S., Jr., Porterfield, K.L. et al. 1976. Numerical Simulation of Water-Oil Flow in Naturally Fractured Reservoirs. *Society of Petroleum Engineers Journal* **16** (6). DOI: 10.2118/5719-PA

Kim, T.H. and Schechter, D.S. 2009. Estimation of Fracture Porosity of Naturally Fractured Reservoirs with No Matrix Porosity Using Fractal Discrete Fracture Networks. *SPE Reservoir Evaluation & Engineering* **12** (2). DOI: 10.2118/110720-PA

King, M.J., Wang, Z., and Datta-Gupta, A. 2016. Asymptotic Solutions of the Diffusivity Equation and Their Applications. Society of Petroleum Engineers. DOI: 10.2118/180149-MS.

Konukoglu, E., Sermesant, M., Clatz, O. et al. 2007. A Recursive Anisotropic Fast Marching Approach to Reaction Diffusion Equation: Application to Tumor Growth Modeling. In *Information Processing in Medical Imaging: 20th International Conference, Ipmi 2007, Kerkrade, the Netherlands, July 2-6, 2007. Proceedings*, ed. Karssemeijer, N. and Lelieveldt, B., Berlin, Heidelberg: Springer Berlin Heidelberg.

Kuchuk, F. and Biryukov, D. 2014. Pressure-Transient Behavior of Continuously and Discretely Fractured Reservoirs. *SPE Reservoir Evaluation & Engineering* **17** (1). DOI: 10.2118/158096-PA

Kuchuk, F.J. 2009. Radius of Investigation for Reserve Estimation from Pressure Transient Well Tests. Society of Petroleum Engineers. DOI: 10.2118/120515-MS.

Kulkarni, K.N., Datta-Gupta, A., and Vasco, D.W. 2000. A Streamline Approach for Integrating Transient Pressure Data into High Resolution Reservoir Models. Society of Petroleum Engineers. DOI: 10.2118/65120-MS.

Lee, S.H., Lough, M.F., and Jensen, C.L. 2001. Hierarchical Modeling of Flow in Naturally Fractured Formations with Multiple Length Scales. *Water Resources Research* **37** (3): 443-455. DOI: 10.1029/2000WR900340

Lee, W.J. 1982. *Well Testing*. Spe Textbook Series. Richardson, TX: Society of Petroleum Engineers. Original edition. ISBN 978-089520-317-5.

Lelièvre, P.G., Farquharson, C.G., and Hurich, C.A. 2011. Computing First-Arrival Seismic Traveltimes on Unstructured 3-D Tetrahedral Grids Using the Fast Marching Method. *Geophysical Journal International* **184** (2): 885-896. DOI: 10.1111/j.1365-246X.2010.04880.x

Li, L. and Lee, S.H. 2008. Efficient Field-Scale Simulation of Black Oil in a Naturally Fractured Reservoir through Discrete Fracture Networks and Homogenized Media. *SPE Reservoir Evaluation & Engineering* **11** (4). DOI: 10.2118/103901-PA

Lindsay, G.J., White, D.J., Miller, G.A. et al. 2016. Understanding the Applicability and Economic Viability of Refracturing Horizontal Wells in Unconventional Plays. Society of Petroleum Engineers. DOI: 10.2118/179113-MS.

Ma, X., Plaksina, T., and Gildin, E. 2013. Optimization of Placement of Hydraulic Fracture Stages in Horizontal Wells Drilled in Shale Gas Reservoirs. Unconventional Resources Technology Conference.

Maleknejad, K. and Sohrabi, S. 2007. Numerical Solution of Fredholm Integral Equations of the First Kind by Using Legendre Wavelets. *Applied Mathematics and Computation* **186** (1): 836-843. DOI: https://doi.org/10.1016/j.amc.2006.08.023

Mallison, B.T., Hui, M.H., and Narr, W. 2010. Practical Gridding Algorithms for Discrete Fracture Modeling Workflows. Paper presented at the 12th ECMOR, Oxford, UK.

Malpani, R., Sinha, S., Charry, L. et al. 2015. Improving Hydrocarbon Recovery of Horizontal Shale Wells through Refracturing. Society of Petroleum Engineers. DOI: 10.2118/175920-MS.

Matthews, C.S., Brons, F., and Hazebroek, P. 1954. A Method for Determination of Average Pressure in a Bounded Reservoir. *Petroleum Transactions, AIME* **201**: 182-191.

Maxwell, S.C., Urbancic, T.I., Steinsberger, N. et al. 2002. Microseismic Imaging of Hydraulic Fracture Complexity in the Barnett Shale. Society of Petroleum Engineers. DOI: 10.2118/77440-MS.

Miller, C.K., Waters, G.A., and Rylander, E.I. 2011. Evaluation of Production Log Data from Horizontal Wells Drilled in Organic Shales. Society of Petroleum Engineers. DOI: 10.2118/144326-MS.

Mirzaei, M. and Cipolla, C.L. 2012. A Workflow for Modeling and Simulation of Hydraulic Fractures in Unconventional Gas Reservoirs. Society of Petroleum Engineers. DOI: 10.2118/153022-MS.

Mitchell, M. 1999. *An Introduction to Genetic Algorithms*. Cambridge, Massachusetts: The MIT Press. Original edition. ISBN 978-0262631853.

Mroczka, J. and Szczuczyński, D. 2009. Inverse Problems Formulated in Terms of First-Kind Fredholm Integral Equations in Indirect Measurements. *Metrology and Measurement Systems* **16** (3): 333-357.

Nordbotten, J.M., Celia, M.A., and Bachu, S. 2004. Analytical Solutions for Leakage Rates through Abandoned Wells. *Water Resources Research* **40** (4): n/a-n/a. DOI: 10.1029/2003WR002997

Oda, M. 1984. Permeability Tensor for Discontinuous Rock Masses. *Geotechnique* **35** (4): 483-495.

Olorode, O., Freeman, C.M., Moridis, G. et al. 2013. High-Resolution Numerical Modeling of Complex and Irregular Fracture Patterns in Shale-Gas Reservoirs and Tight Gas Reservoirs. *SPE Reservoir Evaluation & Engineering*. DOI: 10.2118/152482-PA

Oruganti, Y., Mittal, R., McBurney, C.J. et al. 2015. Re-Fracturing in Eagle Ford and Bakken to Increase Reserves and Generate Incremental Npv: Field Study. Society of Petroleum Engineers. DOI: 10.2118/173340-MS.

Persson, P.O. and Strang, G. 2004. A Simple Mesh Generator in Matlab. *SIAM Review* **46** (2): 329-345.

Pratikno, H., Rushing, J.A., and Blasingame, T.A. 2003. Decline Curve Analysis Using Type Curves - Fractured Wells. Society of Petroleum Engineers. DOI: 10.2118/84287-MS.

Qian, J., Zhang, Y.-T., and Zhao, H.-K. 2007. A Fast Sweeping Method for Static Convex Hamilton–Jacobi Equations. *Journal of Scientific Computing* **31** (1): 237-271. DOI: 10.1007/s10915-006-9124-6

Riahi, A. and Damjanac, B. 2013. Numerical Study of Interaction between Hydraulic Fracture and Discrete Fracture Network. In *Effective and Sustainable Hydraulic Fracturing*, ed. Bunger, A.P., McLennan, J., and Jeffrey, R., Rijeka: InTech.

Riele, H.J.J. 1985. A Program for Solving First Kind Fredholm Integral Equations by Means of Regularization. *Computer Physics Communications* **36** (4): 423-432. DOI: http://dx.doi.org/10.1016/0010-4655(85)90032-3

Roussel, N.P. and Sharma, M.M. 2012. Role of Stress Reorientation in the Success of Refracture Treatments in Tight Gas Sands. *SPE Production & Operations*. DOI: 10.2118/134491-PA

Roussel, N.P. and Sharma, M.M. 2013. Selecting Candidate Wells for Refracturing Using Production Data. *SPE Production & Operations*. DOI: 10.2118/146103-PA

Saldungaray, P.M., Palisch, T., and Shelley, R. 2013. Hydraulic Fracturing Critical Design Parameters in Unconventional Reservoirs. Society of Petroleum Engineers. DOI: 10.2118/164043-MS.

Savitski, A.A., Lin, M., Riahi, A. et al. 2013. Explicit Modeling of Hydraulic Fracture Propagation in Fractured Shales. International Petroleum Technology Conference. DOI: 10.2523/IPTC-17073-MS.

Sehbi, B.S., Kang, S., Datta-Gupta, A. et al. 2011. Optimizing Fracture Stages and Completions in Horizontal Wells in Tight Gas Reservoirs Using Drainage Volume Calculations. Society of Petroleum Engineers. DOI: 10.2118/144365-MS.

Sethian, J.A. 1996. A Fast Marching Level Set Method for Monotonically Advancing Fronts. *Proceedings of the National Academy of Sciences* **93** (4): 1591-1595.

Sethian, J.A. 1999. Fast Marching Methods. *SIAM Review* **41** (2): 199-235.

Sethian, J.A. and Vladimirsky, A. 2000. Fast Methods for the Eikonal and Related Hamilton– Jacobi Equations on Unstructured Meshes. *Proceedings of the National Academy of Sciences* **97** (11): 5699-5703.

Sierra, L., Mayerhofer, M., and Jin, C.J. 2013. Production Forecasting of Hydraulically Fractured Conventional Low-Permeability and Unconventional Reservoirs Linking the More Detailed Fracture and Reservoir Parameters. Society of Petroleum Engineers. DOI: 10.2118/163833-MS.

Sinha, S. and Ramakrishnan, H. 2011. A Novel Screening Method for Selection of Horizontal Refracturing Candidates in Shale Gas Reservoirs. Society of Petroleum Engineers. DOI: 10.2118/144032-MS.

Song, B. and Ehlig-Economides, C.A. 2011. Rate-Normalized Pressure Analysis for Determination of Shale Gas Well Performance. Society of Petroleum Engineers. DOI: 10.2118/144031-MS.

Sun, J. and Schechter, D. 2015. Optimization-Based Unstructured Meshing Algorithms for Simulation of Hydraulically and Naturally Fractured Reservoirs with Variable Distribution of Fracture Aperture, Spacing, Length, and Strike. *SPE Reservoir Evaluation & Engineering* **18** (4). DOI: 10.2118/170703-PA

Sun, Y. and Fomel, S. 1998. Fast-Marching Eikonal Solver in the Tetragonal Coordinates. Paper presented at the 1998 SEG Annual Meeting, New Orleans, Louisiana. Society of Exploration Geophysicists.

Valko, P.P. and Lee, W.J. 2010. A Better Way to Forecast Production from Unconventional Gas Wells. Society of Petroleum Engineers. DOI: 10.2118/134231-MS.

Vasco, D.W., Keers, H., and Karasaki, K. 2000. Estimation of Reservoir Properties Using Transient Pressure Data: An Asymptotic Approach. *Water Resources Research* **36** (12): 3447-3465. DOI: 10.1029/2000WR900179

Vidale, J. 1988. Finite-Difference Calculation of Travel Times. *Bulletin of the Seismological Society of America* **78** (6): 2062.

Vincent, M. 2011. Restimulation of Unconventional Reservoirs: When Are Refracs Beneficial? *Journal of Canadian Petroleum Technology*. DOI: 10.2118/136757-PA

Wang, S.Y., Luo, X.L., and Hurt, R.S. 2013. What We Learned from a Study of Re-Fracturing in Barnett Shale: An Investigation of Completion/Fracturing, and

Production of Re-Fractured Wells. International Petroleum Technology Conference. DOI: 10.2523/IPTC-17081-Abstract.

Warren, J.E. and Root, P.J. 1963. The Behavior of Naturally Fractured Reservoirs. *Society of Petroleum Engineers Journal* **3** (3). DOI: 10.2118/426-PA

Weese, J. 1992. A Reliable and Fast Method for the Solution of Fredholm Integral Equations of the First Kind Based on Tikhonov Regularization. *Computer Physics Communications* **69** (1): 99-111.

Winestock, A.G. and Colpitts, G.P. 1965. Advances in Estimating Gas Well Deliverability. *Journal of Canadian Petroleum Technology*. DOI: 10.2118/65-03-01

Wu, R., Kresse, O., Weng, X. et al. 2012. Modeling of Interaction of Hydraulic Fractures in Complex Fracture Networks. Society of Petroleum Engineers. DOI: 10.2118/152052-MS.

Xie, J., Yang, C., Gupta, N. et al. 2015a. Depth of Investigation and Depletion in Unconventional Reservoirs with Fast-Marching Methods. *SPE Journal* **20** (4). DOI: 10.2118/154532-PA

Xie, J., Yang, C., Gupta, N. et al. 2015b. Integration of Shale-Gas-Production Data and Microseismic for Fracture and Reservoir Properties with the Fast Marching Method. *SPE Journal*. DOI: 10.2118/161357-PA

Xue, X., Yang, C., Sharma, V.K. et al. 2016. Reservoir and Fracture Flow Characterization Using a Novel W(T) Formulation. Unconventional Resources Technology Conference. DOI: 10.15530/URTEC-2016-2440083.

Yan, B., Alfi, M., Wang, Y. et al. 2013. A New Approach for the Simulation of Fluid Flow in Unconventional Reservoirs through Multiple Permeability Modeling. Society of Petroleum Engineers. DOI: 10.2118/166173-MS.

Yang, C., King, M.J., and Datta-Gupta, A. 2017. Rapid Simulation of Naturally Fractured Unconventional Reservoirs with Unstructured Grids Using the Fast Marching Method. Society of Petroleum Engineers. DOI: 10.2118/182612-MS.

Yang, C., Sharma, V.K., Datta-Gupta, A. et al. 2015. A Novel Approach for Production Transient Analysis of Shale Gas/Oil Reservoirs. Unconventional Resources Technology Conference. DOI: 10.15530/URTEC-2015-2176280.

Yang, C., Vyas, A., Datta-Gupta, A. et al. 2017. Rapid Multistage Hydraulic Fracture Design and Optimization in Unconventional Reservoirs Using a Novel Fast

Marching Method. *Journal of Petroleum Science and Engineering* **156**: 91-101. DOI: https://doi.org/10.1016/j.petrol.2017.05.004

Yang, C., Xue, X., Huang, J. et al. 2016. Rapid Refracturing Candidate Selection in Shale Reservoirs Using Drainage Volume and Instantaneous Recovery Ratio. Unconventional Resources Technology Conference. DOI: 10.15530/URTEC-2016-2459368.

Ye, P. and Ayala, L. 2013. Straightline Analysis of Flow Rate Vs. Cumulative-Production Data for the Explicit Determination of Gas Reserves. *Journal of Canadian Petroleum Technology*. DOI: 10.2118/165583-PA

Yin, J., Park, H., Datta-Gupta, A. et al. 2010. A Hierarchical Streamline-Assisted History Matching Approach with Global and Local Parameter Updates. Society of Petroleum Engineers. DOI: 10.2118/132642-MS.

Yin, J., Xie, J., Datta-Gupta, A. et al. 2011. Improved Characterization and Performance Assessment of Shale Gas Wells by Integrating Stimulated Reservoir Volume and Production Data. Society of Petroleum Engineers. DOI: 10.2118/148969-MS.

Zhang, Y., Bansal, N., Fujita, Y. et al. 2016. From Streamlines to Fast Marching: Rapid Simulation and Performance Assessment of Shale-Gas Reservoirs by Use of Diffusive Time of Flight as a Spatial Coordinate. *SPE Journal*. DOI: 10.2118/168997-PA

Zhang, Y., Yang, C., King, M.J. et al. 2013. Fast-Marching Methods for Complex Grids and Anisotropic Permeabilities: Application to Unconventional Reservoirs. Society of Petroleum Engineers. DOI: 10.2118/163637-MS.

Zoveidavianpoor, M., Samsuri, A., and Shadizadeh, S.R. 2012. Development of a Fuzzy System Model for Candidate-Well Selection for Hydraulic Fracturing in a Carbonate Reservoir. Society of Petroleum Engineers. DOI: 10.2118/153200-MS.

APPENDIX A

DTOF-BASED 1D FLUID FLOW EQUATION

Following Zhang et al. (2016) and Fujita et al. (2016), the 1D DToF-based coordinate transformation of the fluid flow equation can be derived using the divergence theorem. To start, a single-phase mass balance equation is given by Eq.A-1:

$$\frac{\partial(\rho\phi)}{\partial t} = -\nabla \cdot (\rho\vec{u}) \tag{A-1}$$

Here $\vec{u}$ is the Darcy velocity, expressed by Eq.A-2:

$$\vec{u} = -\frac{k(\vec{x})}{\mu}\nabla p \tag{A-2}$$

As shown by Vasco et al. (2000), Kulkarni et al. (2000) and Xie et al. (2015a, 2015b), the transient pressure propagation process can be captured through the following Eikonal equation (Eq.A-3), which is derived from the asymptotic solution of the diffusivity equation.

$$\nabla\tau \cdot \alpha(\vec{x}) \cdot \nabla\tau = \nabla\tau \cdot \frac{k(\vec{x})}{\varphi(\vec{x})\mu c_t} \cdot \nabla\tau = 1 \tag{A-3}$$

To reduce the fluid flow equation (Eq.A-1 and A-2) to only one spatial dimension, we assume that the pressure only depends on τ in space, which is equivalent to assuming that the pressure gradient direction aligns with the τ gradient direction (Eq.A-4).

$$\nabla p \approx \frac{\partial p}{\partial\tau}\nabla\tau \tag{A-4}$$

According to the pressure propagation equation (Eq.A-3), the permeability is related to τ gradient:

$$k = \frac{(\phi \mu c_t)_{init}}{\nabla \tau \cdot \nabla \tau} \tag{A-5}$$

Substituting Eq.A-4 and A-5 into Darcy's law (Eq.A-2), we obtain the τ -based velocity equation (Eq.A-6), where $\hat{n}_\tau$ is the unit normal vector to the contour of τ .

$$\vec{u} = -\frac{(\phi \mu c_t)_{init}}{\mu} \frac{1}{|\nabla \tau|} \frac{\partial p}{\partial \tau} \hat{n}_\tau \, , \; \hat{n}_\tau = \frac{\nabla \tau}{|\nabla \tau|} \tag{A-6}$$

We take the volumetric integral of the above mass balance equation (Eq.A-1) over the domain, Ω:

$$\int_\Omega \frac{\partial (\phi \rho)}{\partial t} dV = -\int_\Omega \nabla \cdot (\rho \vec{u}) dV \tag{A-7}$$

Based on the divergence theorem, the flux term is transformed to the following surface integral (Eq.A-8), accounting for the τ -based velocity equation (Eq.A-6):

$$\int_\Omega \nabla \cdot (\rho \vec{u}) dV = \oint_{\partial \Omega} (\rho \vec{u}) \cdot \hat{n}_\tau dA = -\oint_{\partial \Omega} \rho \frac{(\phi \mu c_t)_{init}}{\mu} \frac{1}{|\nabla \tau|} \frac{\partial p}{\partial \tau} dA \tag{A-8}$$

The integral of the fluid flow equation, in the τ coordinate system, then takes the following form:

$$\int_\Omega \frac{\partial (\phi \rho)}{\partial t} dV = \oint_{\partial \Omega} \rho \frac{(\phi \mu c_t)_{init}}{\mu} \frac{1}{|\nabla \tau|} \frac{\partial p}{\partial \tau} dA \tag{A-9}$$

From the calculation of the drainage pore volume, we can define the $w(\tau)$ function as Eq.A-11.

$$dV_p = \int_\Omega \phi_{init} dV = \oint_{\partial \Omega} \phi_{init} \nabla \tau \cdot \hat{n}_\tau dA = \Delta \tau \oint_{\partial \Omega} \phi_{init} \frac{1}{|\nabla \tau|} dA \tag{A-10}$$

$$\oint_{\partial \Omega} \phi_{init} \frac{1}{|\nabla \tau|} dA = \frac{dV_p}{d\tau} = w(\tau) \tag{A-11}$$

Note that the $w(\tau)$ function is the derivative of the drainage pore volume with respect to τ, which indicates how fast the drainage pore volume increases.

Eq.A-11 induces $\phi_{init}\Delta V = w(\tau)\Delta\tau$, and then the accumulation term can be expressed as Eq.A-12:

$$\int_{\Omega} \frac{\partial(\phi\rho)}{\partial t} dV = \frac{\partial(\phi\rho)}{\partial t} \frac{w(\tau)}{\varphi_{init}} \Delta\tau \tag{A-12}$$

Substituting Eq.A-11 and A-12 into Eq. A-9, and let $\Delta\tau \to 0$, we obtain:

$$\frac{w(\tau)}{\phi_{init}} \frac{\partial(\phi\rho)}{\partial t} = \frac{\partial}{\partial\tau}\left(w(\tau)\rho \frac{(\mu c_t)_{init}}{\mu} \frac{\partial p}{\partial\tau} \right) \tag{A-13}$$

Rearranging the above equation (Eq.A-13) and taking any sink/source terms into consideration, we obtain the following 1D fluid flow equation along τ -coordinate.

$$\frac{\partial(\phi\rho)}{\partial t} = \frac{\phi_{init}}{w(\tau)} \frac{\partial}{\partial\tau}\left(w(\tau)\rho \frac{(\mu c_t)_{init}}{\mu} \frac{\partial p}{\partial\tau} \right) + \rho q \tag{A-14}$$

APPENDIX B

ANISOTROPIC PERMEABILITY ANALYSIS

B.1 Principal Component in 2D

With symmetric positive definite permeability tensor in 2D (shown by Eq.B-1), the permeability tensor after applying the rotation matrix could be expressed as Eq.B-2 or further expressed as Eq.B-3.

$$\overline{\overline{\mathbf{k}}} = \begin{bmatrix} k_{11} & k_{12} \\ k_{21} & k_{22} \end{bmatrix} \tag{B-1}$$

$$\begin{bmatrix} k_{11}^{'} & k_{12}^{'} \\ k_{21}^{'} & k_{22}^{'} \end{bmatrix} = \begin{bmatrix} \cos\theta & \sin\theta \\ -\sin\theta & \cos\theta \end{bmatrix} \begin{bmatrix} k_{11} & k_{12} \\ k_{21} & k_{22} \end{bmatrix} \begin{bmatrix} \cos\theta & -\sin\theta \\ \sin\theta & \cos\theta \end{bmatrix} \tag{B-2}$$

$$\begin{cases} k_{11}^{'} = k_{11}\cos^2\theta + k_{22}\sin^2\theta + k_{12}\sin 2\theta \\ k_{22}^{'} = k_{11}\sin^2\theta + k_{22}\cos^2\theta - k_{12}\sin 2\theta \\ k_{12}^{'} = (k_{22} - k_{11})\sin\theta\cos\theta + k_{12}\cos 2\theta \end{cases} \tag{B-3}$$

The requirement for the rotated permeability tensor to serve as the principal direction is $k_{12}^{'} = 0$. Thus the principal component and the rotation angle can be calculated using Eq.B-4.

$$\begin{cases} k_{11}^{'}, k_{22}^{'} = \dfrac{k_{11} + k_{22}}{2} \pm \sqrt{k_{12}^2 + \left(\dfrac{k_{11} - k_{22}}{2}\right)^2} \\ \theta = \dfrac{1}{2}\arctan\left(\dfrac{2k_{12}}{k_{11} - k_{22}}\right) \end{cases} \tag{B-4}$$

when θ belongs to $\left[-\dfrac{\pi}{4}, \dfrac{\pi}{4}\right]$, $k_{11}^{'}$ corresponds to the maximum principal component if $k_{11} > k_{22}$.

B.2 Principal Component in 3D

Let's first take a look at the rotation matrix in a standard right-handed Cartesian coordinate system. Any vector can be decomposed into a two-step rotations, as illustrated by Figure B-1: first rotate θ with *z* axis as rotate vector and then rotate φ with $\mathbf{u}$ as rotate vector. The vector $\mathbf{u}$ in Figure B-1 is within the *x*-*y* plane and perpendicular to the solid green and red vector. The rotation matrix for the first and second step are given by $\mathbf{R}_Z(\theta)$ (Eq.B-5) and $\mathbf{R}_\mathbf{u}(\varphi)$ (Eq.B-6), respectively. The combined rotation matrix can be expressed as $\mathbf{R} = \mathbf{R}_Z(\theta)\mathbf{R}_\mathbf{u}(\varphi)$ (Eq.B-7).

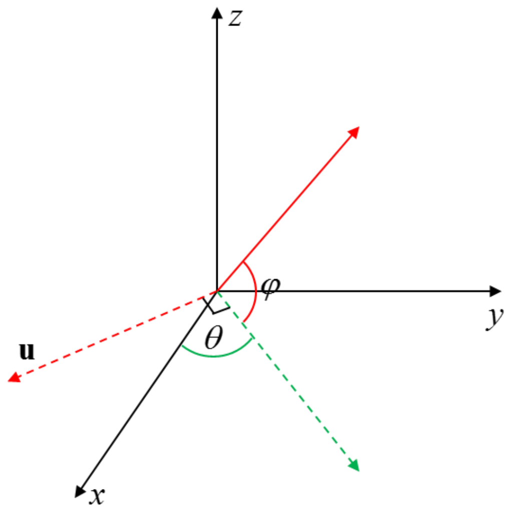

Figure B-1 Illustration of rotating coordinates to an arbitrary direction in 3D

$$\mathbf{R}_Z(\theta) = \begin{bmatrix} \cos\theta & -\sin\theta & 0 \\ \sin\theta & \cos\theta & 0 \\ 0 & 0 & 1 \end{bmatrix} \tag{B-5}$$

$$\mathbf{R}_\mathbf{u}(\varphi) = \begin{bmatrix} \cos\varphi + \sin^2\theta(1-\cos\varphi) & -\sin\theta\cos\theta(1-\cos\varphi) & -\sin\varphi\cos\theta \\ -\sin\theta\cos\theta(1-\cos\varphi) & \cos\varphi + \cos^2\theta(1-\cos\varphi) & -\sin\varphi\sin\theta \\ \sin\varphi\cos\theta & \sin\varphi\sin\theta & \cos\varphi \end{bmatrix} \tag{B-6}$$

$$\mathbf{R} = \mathbf{R}_Z(\theta)\mathbf{R}_{\mathbf{u}}(\varphi) = \begin{bmatrix} \begin{matrix}\sin 2\theta \sin\theta + \\ \cos 2\theta \cos\theta \cos\varphi\end{matrix} & \begin{matrix}-\sin 2\theta \cos\theta + \\ \cos 2\theta \sin\theta \cos\varphi\end{matrix} & -\sin\varphi \cos 2\theta \\ \begin{matrix}-\sin\theta \cos 2\theta + \\ \sin 2\theta \cos\theta \cos\varphi\end{matrix} & \begin{matrix}\cos 2\theta \cos\theta + \\ \sin 2\theta \sin\theta \cos\varphi\end{matrix} & -\sin\varphi \sin 2\theta \\ \sin\varphi \cos\theta & \sin\varphi \sin\theta & \cos\varphi \end{bmatrix} \tag{B-7}$$

Suppose the symmetric positive definite permeability tensor in 3D is expressed as Eq.B-8. By applying the rotation matrix, the permeability tensor could be expressed as Eq.B-9. Or the permeability tensor in original coordinates can be expressed in terms of the permeability tensor in new coordinates with Eq.B-10.

$$\bar{\bar{\mathbf{k}}} = \begin{bmatrix} k_{11} & k_{12} & k_{13} \\ k_{21} & k_{22} & k_{23} \\ k_{31} & k_{32} & k_{33} \end{bmatrix},\ k_{12} = k_{21}, k_{13} = k_{31}, k_{23} = k_{32} \tag{B-8}$$

$$\bar{\bar{\mathbf{k}}}' = \mathbf{R}^T \cdot \bar{\bar{\mathbf{k}}} \cdot \mathbf{R} \tag{B-9}$$

$$\bar{\bar{\mathbf{k}}} = \mathbf{R} \cdot \bar{\bar{\mathbf{k}}}' \cdot \mathbf{R}^T \tag{B-10}$$

If $\bar{\bar{\mathbf{k}}}'$ serves as the principal direction, Eq.B-10 is equivalent to perform the Eigen-decomposition of $\bar{\bar{\mathbf{k}}}$. The eigenvalue provide the principal component and the eigenvectors give the rotation matrix.

B.3 Permeability Magnitude at Arbitrary Direction

Let’s first look at 2D case. Suppose the principal direction has a rotation angle θ, and we are computing the permeability in $\mathbf{n} = (\cos\varphi, \sin\varphi)^T$ direction (shown by Figure B-2). In the rotated coordinate system, the permeability satisfys Eq.B-11,

$$\frac{x'^2}{k_1}+\frac{y'^2}{k_2}=1 \tag{B-11}$$

The coordinate of the intersection between vector $\mathbf{n}$ and the ellipse can be expressed as $\left(\sqrt{k}\cos(\varphi-\theta),\sqrt{k}\sin(\varphi-\theta)\right)$ Substitute it into Eq.B-11, the permeability can be calculated as Eq.B-12,

$$k=\frac{k_1k_2}{k_1\sin^2(\varphi-\theta)+k_2\cos^2(\varphi-\theta)} \tag{B-12}$$

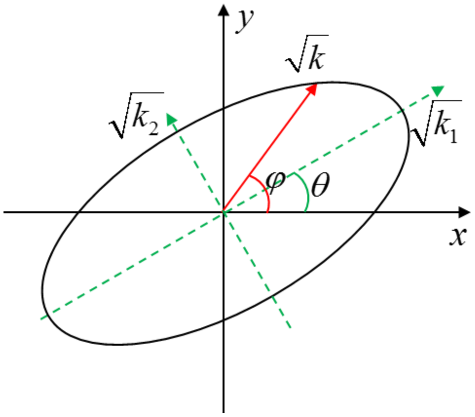

Figure B-2 Illustration of calculating the magnitude of permeability in anisotropic scenario

If the principal direction of permeability tensor is aligned with coordinate axis in 3D, which means the permeability tensor can be expressed as Eq.B-13

$$\frac{x^2}{k_1}+\frac{y^2}{k_2}+\frac{z^2}{k_3}=1 \tag{B-13}$$

For the any unit direction vector $\mathbf{n}=(n_1,n_2,n_3)^T$, the endpoint of vector $(\sqrt{k}n_1,\sqrt{k}n_2,\sqrt{k}n_3)$ should satisfy equation Eq.B-13, which provides us the permeability in $\mathbf{n}$ direction as,

$$k = \frac{k_1 k_2 k_3}{k_2 k_3 n_1^2 + k_1 k_3 n_2^2 + k_1 k_2 n_3^2} \tag{B-14}$$

In the case the principal direction of permeability tensor is not aligned with coordinate axis in 3D, an additional rotation is applied. As illustrated by Eq.B-10, a Eigen-decomposition procedure is first applied to the permeability tensor to obtain the rotation matrix $\mathbf{R}$ and the principal component $(k_{11}^{'}, k_{22}^{'}, k_{22}^{'})^T$. The unit direction vector $\mathbf{n} = (n_1, n_2, n_3)^T$ is rotated to the principal direction based coordinate system, and be expressed as $\mathbf{R} \cdot \mathbf{n} = (n_1^{'}, n_2^{'}, n_3^{'})^T$. Finally, the permeability can be calculated as Eq.B-15,

$$k = \frac{k_{11}^{'} k_{22}^{'} k_{33}^{'}}{k_{22}^{'} k_{33}^{'} n_1^{'2} + k_{11}^{'} k_{33}^{'} n_2^{'2} + k_{11}^{'} k_{22}^{'} n_3^{'2}} \tag{B-15}$$

APPENDIX C

FREDHOLM INTEGRAL EQUATION OF THE FIRST KIND

Eq.4.13 turns out to be Fredholm integral equations of this first kind, which exists in a broad class of continuous linear invasive problem in science and engineering, such as computerized tomography, image restoration, and digital signal processing (Mroczka and Szczuczyński 2009).

$$\int_a^b k(x,t)\,f(t)\,dt = g(x)\,,\ a \le x \le b \tag{C-1}$$

where $g(x)$ and $k(x,t)$ are known functions and $f(t)$ is the unknown function to be determined. The discretized inverse problem formulated in terms of Fredholm inverse integral equation of the first kind is generally ill-posed and ill-conditioned. Several numerical inverse techniques were proposed by researchers for solving this type of problem, where the regularization method (Hansen 1992; Riele 1985; Weese 1992) and projection methods (Maleknejad and Sohrabi 2007), such as Galerkin and collocation methods, are widely utilized.

In regularization method, the problem is set to minimize the following quadratic function Eq.C-2,

$$\Phi(f) = \left\| \int_a^b k(x,t)\,f(t)\,dt - g(x) \right\|^2 + \lambda \left\| Lf \right\|^2 \tag{C-2}$$

where λ is a the so-called regularization parameter, L is an operator, for which the identity ($Lf = f$) or the second derivative ($Lf = f^{''}$) is frequently used. In the discretization, the integral in Eq.C-2 at particular x value is approximated by

$$\begin{aligned}\left\|\int_a^b k(x_i,t)\,f(t)dt-g(x_i)\right\|^2 &= \left\|\sum_{j=1}^{N}\int_{t_{j-1}}^{t_j} k(x_i,t)\,f(t)dt-g(x_i)\right\|^2 \\ = \left\|\sum_{j=1}^{N} f(t_j)\int_{t_{j-1}}^{t_j} k(x_i,t)dt-g(x_i)\right\|^2 &= \left\|\sum_{j=1}^{N}K_{ij}f_j-g(x_i)\right\|^2\end{aligned} \tag{C-3}$$

Substituting Eq.C-3 into Eq.C-2, and with a selected operator L, the minimization problem shown by Eq.C-2 can be solved by imposing $\partial\Phi(f)/\partial f_j = 0$.

In Galerkin method, a sequence of orthonormal basis function is used to approximate the solutions

$$f_n(t)=\sum_{j=1}^{d_n} c_j\varphi_j(t) \tag{C-4}$$

By substituting Eq.C-4 into C-1, we have the approximated residual term

$$r_n(x)=\int_a^b k(x,t)y_n(t)dt-g(x)=\sum_{j=1}^{d_n}c_j\int_a^b k(x,t)\varphi_j(t)dt-g(x) \tag{C-5}$$

To determine the unknown coefficients, the following requirements are imposed,

$$(r_n(x),\varphi_i)=\int_a^b r_n(x)\varphi_i(x)dx=0 \text{ for } i=1,2,...,d_n \tag{C-6}$$

which leads to the system

$$\sum_{j=1}^{d_n}c_j\int_a^b\int_a^b k(x,t)\varphi_j(t)\varphi_i(x)dtdx=\int_a^b g(x)\varphi_i(x)dx\,,\ i=1,2,...,d_n \tag{C-7}$$

For our problem in Eq.4.13, the challenges are that the Fredholm integral of the first kind is defined on interval $(0,\infty)$, and how to select the appropriate operator L in regulation method or the basis function in Galerkin method to obtain an accurate and robust estimation of the unknown function.